

# Multifunctional Transition Metal-Based Phosphides in Energy-Related Electrocatalysis

Yang Li, Zihao Dong, and Lifang Jiao\*

Dedicated to 100th Anniversary of Nankai university

The exploitation of cheap and efficient electrocatalysts is the key to make energy-related electrocatalytic techniques commercially viable. In recent years, transition metal phosphides (TMPs) electrocatalysts have gained a great deal of attention owing to their multifunctional active sites, tunable structure, and composition, as well as unique physicochemical properties. This review summarizes the up-to-date progress on TMPs in energy-related electrocatalysis from diversified synthetic methods, ingenious-modulated strategies, and novel applications. In order to set forth theory–structure–performance relationships upon TMPs, the corresponding reaction mechanisms, electrocatalysts' structure/composition designs and desired electrochemical performance are jointly discussed, along with demonstrating their practical electrocatalytic applications in overall water splitting, metal–air batteries, lithium–sulfur batteries, etc. In the end, some underpinning issues and research orientations of TMPs toward efficient energy-related electrocatalysis are briefly proposed.

## 1. Introduction

The aggravated global energy and environmental issues bring tremendous challenges to the normal functioning of modern society.<sup>[1]</sup> To achieve sustainable energy cycles, one way is efficiently storing the intermittent renewable energy in reliable energy carriers for human utilization.<sup>[2]</sup> In this regard, a representative example is the solar-to-hydrogen fuel conversion via water splitting, and the yielded hydrogen can be further used in fuel cells.<sup>[3]</sup> Another method is turning the waste into value by properly converting the emitted exhausts into clean fuels and chemical feedstocks, such as the electrochemical CO<sub>2</sub> reduction reaction (CO<sub>2</sub>RR) process.<sup>[4]</sup> These two ways portray a bright blueprint for the future sustainable society. However, these processes are of sluggish kinetics and require robust electrocatalysts to boost the reaction rates.<sup>[5]</sup> Generally speaking,

noble metals are the state-of-the-art electrocatalysts toward these electrochemical reactions, while practical applications are surely constrained by their high cost and limited availability.<sup>[6]</sup> Therefore, it is of great significance to find cheap and efficient electrocatalysts with the aim of making these promising energy-related technologies commercially viable.

At the early stage, the search for electrocatalysts was relied on “trials and errors.”<sup>[7]</sup> While with the finding of descriptors within catalytic reactions, theoretical calculations rationally guide the screening of catalysts by decoupling the reaction process and comparing corresponding adsorption free energy of reaction intermediates.<sup>[8]</sup> This generates a new way for the finding of catalysts in terms of combining theory with experiment.<sup>[3b,9]</sup> For example, an early study

indicated that MoS<sub>2</sub> was nonreactive toward hydrogen evolution reaction (HER), whereas this tide was reversed by the theoretical and experimental identification of the edge active site on nano-sized MoS<sub>2</sub> in electrochemical HER.<sup>[5b,10]</sup> Besides, concerning more complex oxygen evolution reaction (OER), oxygen reduction reaction (ORR), and CO<sub>2</sub>RR,<sup>[11]</sup> combining theory with experiment makes it possible to find suitable catalysts with boosted reaction kinetics and (or) enhanced reaction directionality.<sup>[7a,12]</sup> Following this way, in recent years, some well-recognized electrocatalysts toward specific reaction have successively emerged, such as MoS<sub>2</sub> for HER,<sup>[13]</sup> Co<sub>3</sub>O<sub>4</sub> for OER/ORR,<sup>[14]</sup> and Cu for CO<sub>2</sub>RR.<sup>[15]</sup> Unfortunately, their intrinsically unfavorable physicochemical features, such as the insufficient active sites of MoS<sub>2</sub>,<sup>[16]</sup> the poor electron conductivity of Co<sub>3</sub>O<sub>4</sub>,<sup>[17]</sup> surely enable these electrocatalysis processes not somewhat efficiency, not to mention further extending them to practical utilization.

In contrast, transition metal phosphides (TMPs) may break through these limits to be suitable electrocatalysts due to their distinct physicochemical properties, such as desirable electronic and magnetic properties, polytropic composition and structure.<sup>[18]</sup> In the periodic table, nearly all of the transition metal elements can react with phosphorus to form TMPs (Figure 1a).<sup>[19]</sup> Phosphides chemistry is very complex because different constituent elements and stoichiometric ratios can give rise to various structures.<sup>[20]</sup> Taken the nickel phosphides as an example, there are more than nine kinds of nickel phosphides with different nickel/phosphorus stoichiometric ratios.<sup>[21]</sup> Figure 1b displays some typical crystal structures of binary nickel phosphides. Among them,

Y. Li, Z. Dong, Prof. L. Jiao  
Key Laboratory of Advanced Energy Materials Chemistry  
(Ministry of Education)  
Renewable Energy Conversion and Storage Center (ReCast)  
College of Chemistry  
Nankai University  
Tianjin 300071, China  
E-mail: jiaolf@nankai.edu.cn

 The ORCID identification number(s) for the author(s) of this article can be found under <https://doi.org/10.1002/aenm.201902104>.

DOI: 10.1002/aenm.201902104

the metal-rich  $\text{Ni}_{12}\text{P}_5$  adopts a tetragonal structure with a point group of  $I4/m$ , and each Ni atom is bonded to four phosphorus atoms accompanied by substantial Ni–Ni bonds among the local coordination environment.<sup>[22]</sup> While in phosphorus-rich  $\text{NiP}_3$ , it presents a  $\text{Im}\bar{3}$  cubic structure and possesses abundant P–P bonds, forming the so-called polyphosphides.<sup>[23]</sup> It can be seen that the minor variation in metal/phosphorus stoichiometric ratios leads to significant changes in their structure, thus presenting different physicochemical properties.<sup>[24]</sup> For instance, in metal-rich and monophosphides, abundant metal–metal bonds and metal–phosphorus bonds can endow TMPs with better electron conductivity, thermal, and chemical stability than that of the phosphorus-rich TMPs with plenty of phosphorus–phosphorus bonds.<sup>[21]</sup> Therefore, the desired physicochemical properties of TMPs can be routinely accessed by altering their corresponding composition and structure.

The first catalytic applications of TMPs can be dated back to the 1980s when some TMPs presented the remarkable catalytic performance in hydrodesulfurization (HDS), even better than the commercial  $\text{MoS}_2$ .<sup>[25]</sup> Considering both HDS and HER proceeded with the similar reversible hydrogen and/desorption



**Lifang Jiao** is a professor at Nankai University, China. She received her Ph.D. degree from Nankai University (China) in 2005. Her current research is focused on energy conversion and storage (including lithium, sodium, and magnesium secondary batteries, and super capacitors), hydrogen storage materials, and electrocatalytic hydrogen evolution.

process, TMPs might be active towards electrocatalytic HER.<sup>[26]</sup> This point has been successfully confirmed by the subsequent theoretical and experimental works.<sup>[27]</sup> With flourishing synthetic techniques, a series of nanostructured TMPs with controllable morphology and composition appeared, and demonstrated their abilities in electrocatalytic HER. Successively, recent studies

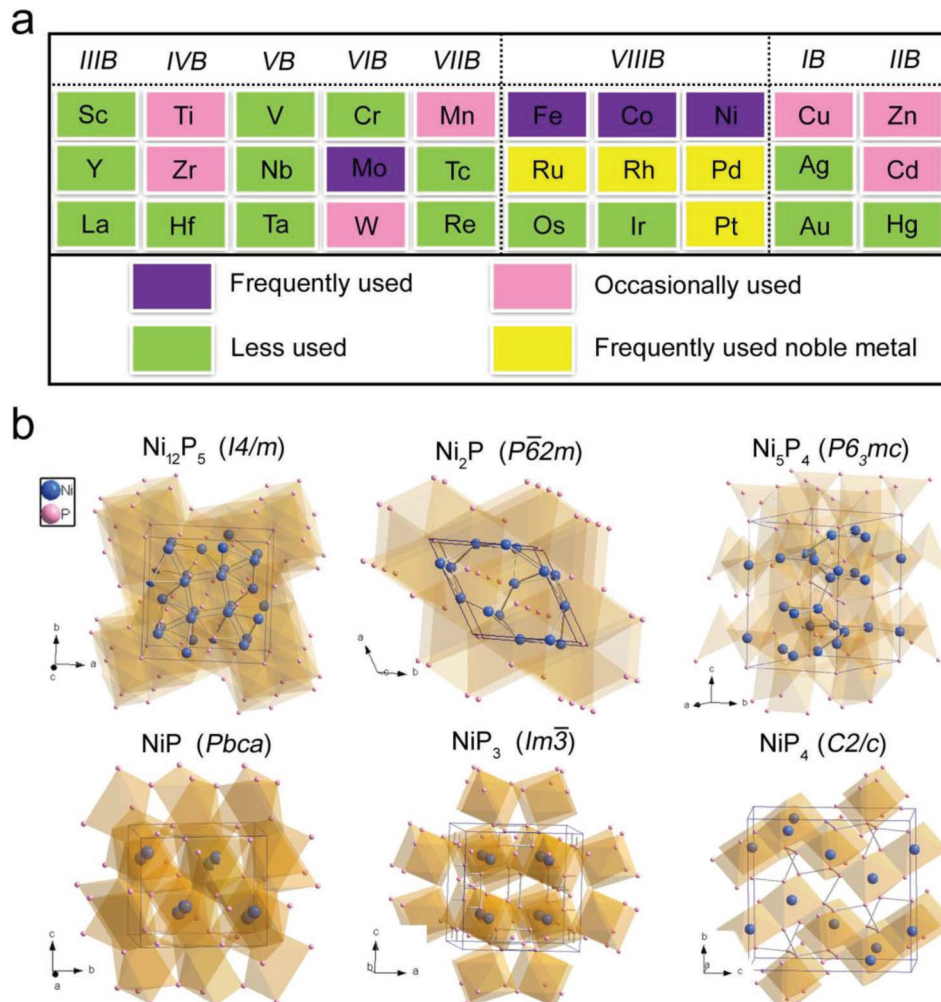


**Figure 1.** a) Elements that are used to form TMPs for electrocatalysis. b) Selected polyhedral representation of the nickel phosphides lattice based on the Ni polyhedra.

proved that TMPs can also serve as highly efficient catalysts or precatalysts in oxygen evolution/reduction,<sup>[28]</sup> which extends their applications to water electrolyzer,<sup>[29]</sup> metal–air batteries,<sup>[30]</sup> and fuel cells.<sup>[31]</sup> Besides, the burgeoning electrocatalytic applications of TMPs in CO<sub>2</sub> electrochemical reduction,<sup>[32]</sup> and organic molecules electrocatalysis,<sup>[33]</sup> along with regulation of the polysulfide redox conversion in lithium–sulfur (Li–S) batteries,<sup>[34]</sup> raise TMPs again to be a research hotspot.

In the past few years, earth-abundant transition metal dichalcogenides (TMDs),<sup>[16b]</sup> metal oxides (TMOs),<sup>[14a]</sup> metal carbides (TMCs),<sup>[35]</sup> metal nitrides (TMNs),<sup>[36]</sup> and pure metals (TMs) have also emerged as catalysts toward these energy-related electrocatalytic reactions,<sup>[37]</sup> whereas TMPs possess some intrinsic advantages over these compounds. Typically, layered TMDs were widely recognized as efficient HER catalysts in acidic conditions. Admittedly, in most cases, the preparation of TMDs undergoes a much milder condition as compared with TMPs' synthesis. It is worth noting that the most stable and only naturally occurring polymorph of TMDs is the 2H phase.<sup>[38]</sup> While its semiconductor nature and edge distributed active sites undoubtedly bring detrimental effects on electrocatalysis. Hence, in order to improve the electrical conductivity and increase exposed active edges, the commonly synthesized TMDs are usually required to be exfoliated into few layers.<sup>[5b]</sup> This additional experimental process seems complex and uneconomical. Although the 1T phase TMDs are found to be metallic and active sites in the basal plane are activated, the synthesis of high-purity 1T phase TMDs is still a challenging work, not to mention its thermally metastable nature. These limitations may make TMDs electrocatalysts not suitable for large-scale applications. Similar to TMDs, TMOs electrocatalysts usually suffer from relatively low electrical conductivity and with regard to designing TMOs catalysts, how to facilitate the electron transfer is always the first concern. In comparison, the emergence of TMPs electrocatalysts may circumvent these obstacles. First, most of metal-rich metal phosphides are metallic, even some TMPs known as the superconductors, showing a better electrical conductivity for electrocatalysis.<sup>[21]</sup> Second, without forming the layered structure, the geometric structure of TMPs endows more crystalline surfaces being exposed, naturally offering more active sites for electrocatalysis.<sup>[39]</sup> Third, in consideration of the unsatisfied performance of TMDs in neutral and alkaline solution as well as stability issues of TMOs in acidic medium,<sup>[40]</sup> TMPs usually present wider applicability for electrocatalysis. Regarding the intermetallic compounds, TMCs and TMNs are also used as electrocatalysts in the field of HER, OER, and ORR. While their synthesis is always involved with high-temperature treatment or post-ammonia reduction annealing, making the synthesis costly, complicated, or even environmental unfriendly.<sup>[41]</sup> Although pure TMs are easy to access and are good conductors of electricity, their catalytic performance is usually unsatisfied because the single metal surface could not provide separate optimization toward the binding affinities of individual intermediates.<sup>[42]</sup> Therefore, in view of the advantageous physicochemical properties and multiple synthesis methods, cheap but efficient TMPs electrocatalysts may be the best candidate to replace noble metals toward these energy-related electrocatalysis reactions.

It is well known that the electrocatalytic performance is highly sensitive to the composition, structure, morphology, and

surface/interface properties of electrocatalysts. Therefore, to achieve significantly exposed active sites, desired structure and composition, as well as optimized surface/interface properties, the insightful principles and effective strategies are quite imperative. In this review, we first summarize the recent progress in the synthesis of TMPs. Then, various modulated strategies for TMPs in electrocatalytic HER, OER, and ORR are successively discussed, including elemental doping, interfacial regulation, phase modification, structural engineering, and nanocarbon incorporation. Upon each item, we aim to provide an in-depth understanding of the theory–structure–function relationship and offer the unequivocal reasons behind the improved electrocatalytic performance. Furthermore, triggered by facilely tailored physicochemical properties of TMPs, their multifunctional applications in electrocatalytic water splitting, metal–air batteries, Li–S batteries, as well as just emerged utilizations in electrocatalytic CO<sub>2</sub> reduction and electrocatalysis of organic molecules are successively demonstrated (**Figure 2**). Eventually, the remaining challenges and outlooks are clarified to offer a fresh impetus for designing robust TMPs electrocatalysts.

## 2. Synthesis of Nanostructured Transition Metal Phosphides

At the early stage, the preparation of metal phosphides required harsh conditions with the use of flammable phosphorus and high toxic phosphine as the phosphating reagent, which undoubtedly impeded the scale-up synthesis and applications.<sup>[43]</sup> With the booming of synthetic-chemistry and nanoscience, some novel synthetic methods are springing up. In the following section, we will briefly summarize the recent progress in the synthesis of TMPs according to the solution-phase reaction, vapor–solid reaction, and emerging methods.

### 2.1. Solution-Phase Reaction

One versatile way for the solution-phase synthesis of TMPs is using organophosphorus as phosphorus sources, including the trioctylphosphine (TOP), triphenyl phosphine (TPP), and their analogues.<sup>[19]</sup> This chemical colloidal route can routinely yield many 3d, 4d, 5d transition metal phosphides with well-defined nanostructures and good crystallinity.<sup>[21]</sup> For example, using TOP as the phosphorus source and metal acetylacetones as the metal precursor, this reaction is proceeding in high boiling point solvent, such as 1-octadecene, and oleylamine. With the elevated reaction temperature ( $\approx 300$  °C), the carbon–phosphorus bonds in TOP molecular are cleaved, so the phosphorus atoms can further coordinate with metal atoms to generate metal phosphides. The reaction process can be expressed as the following chemical formula: (C<sub>8</sub>H<sub>17</sub>)<sub>3</sub>P + M(acac)<sub>2</sub> → MP<sub>x</sub>.<sup>[25b]</sup> The corresponding phase structure, size, and morphology of products are controllable by manipulating the reaction temperature, solvent types, or the molar ratio of metal to phosphorus. Notably, the limitation of this method is required rigorously inert atmosphere conditions to prevent the release of highly flammable phosphorus.<sup>[43]</sup> In contrast, the electrochemical deposition is much milder because the electrodeposition process

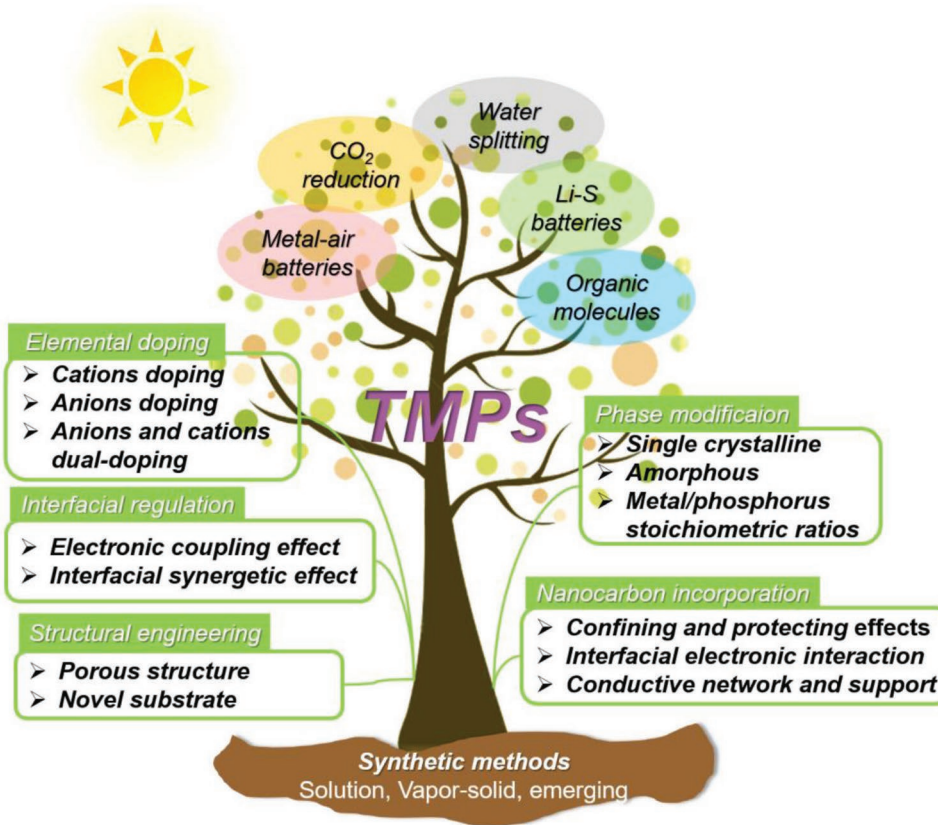


**Figure 2.** Synthetic methods, modulated strategies, and energy-related electrocatalytic applications of TMPs.

is mainly carried out in room temperature and will not release the high-toxic substance. The metal phosphides can be facilely deposited onto the conductive substrate surfaces by the reduction reaction of metal ions and  $\text{H}_2\text{PO}_2^-$ . In general, this method is only applicable to the synthesis of specific metal phosphides, such as Co-P, Ni-P, and the yielded metal phosphides mainly present amorphous features and complex composition.<sup>[44]</sup>

## 2.2. Vapor–Solid Reaction

The common characteristic of the vapor–solid phosphidation reaction is mostly conducted at tube furnace filled with protective gas or in a vacuum environment. Specifically, one approach is employing the bulk or nanosized metal as the precursors and high activity phosphorus steam as the phosphorus source. For this method, the common reaction temperature is above 600 °C, of which this process can be expressed as the chemical formula:  $\text{M}+\text{P}\rightarrow\text{MP}_x$ . We note that using this approach, some P-rich metal phosphides ( $\text{CoP}_3$ ), even some unstable metal phosphides can be prepared.<sup>[21]</sup> Unfortunately, since this high-temperature reaction can produce high activity white phosphorus and phosphine, the tightness of reaction device and following isolation of product should be rigorously controlled. Another method is employing the metal oxides (metal or metal hydroxides) as the precursor and hypophosphite ( $\text{NaH}_2\text{PO}_2$ ,  $\text{NH}_4\text{H}_2\text{PO}_2$ ) as the phosphorus source.<sup>[26a]</sup> Commonly, the  $\text{NaH}_2\text{PO}_2$  and metal oxides precursor are placed in two separate porcelain boats with

the former at the upstream and the latter at the downstream. When the temperature is exceeding 250 °C,  $\text{NaH}_2\text{PO}_2$  is quickly decomposed with simultaneously releasing  $\text{PH}_3$ , which can further react with the metal oxides precursor to produce metal phosphides. The reaction equation can be expressed as follows:  $2\text{NaH}_2\text{PO}_2\rightarrow\text{Na}_2\text{HPO}_4+\text{PH}_3\uparrow$ , then  $\text{PH}_3 + \text{M}_y\text{O}_z\rightarrow\text{M P}_x$ .<sup>[43]</sup> Owing to proceeded at low temperature (300 °C) and short time (2 h), this method can maximize the retention of the morphology of precursors, which paves a new way for the fabrication of nanostructured metal phosphides. Different from the above two vapor–solid strategies, another scalable approach for phosphides, synthesis is the so-called temperature-programmed reduction (TPR) method via the reduction of metal–phosphates by  $\text{H}_2$ .<sup>[45]</sup> Briefly, a mixture of quantitative molar ratio metal salt/diammonium phosphate is calcined in air to produce metal–phosphate precursor, followed by a thermal reduction treatment. Under the high-temperature in  $\text{H}_2$  atmosphere (400–1000 °C), the phosphorus–oxygen bonds are broken and further lead to the formation of metal phosphides. This approach is energy consuming and prone to yielding large grain size metal phosphides.

## 2.3. Emerging Methods

Aside from the aforementioned methods, some novel strategies are flourished in pursuit of making synthetic processes much safer and quicker. For example, compared with unsafe elemental phosphorus sources, the ecofriendly, nontoxic biomass phosphorus

source is much more appealing.<sup>[46]</sup> For instance, phytic acid was reported as the phosphating reagent for the synthesis of TMPs.<sup>[46a]</sup> It can readily form the phytic acid–metal cross-linked structure by virtue of strong coordination effects between its six phosphate groups and metal cations. The following pyrolysis of biomass–metal precursors can produce metal phosphides. The advantage of this method is applicable to the large-scale synthesis of metal phosphides. Likewise, the synthesis of nanostructured TMPs/carbon composites via metal-organic frameworks (MOFs)-derived route recently attracts intensive attention because the synthesized nanostructure has some unique merits, such as the high specific surface area, abundant pore structure, ultrafine size, and excellent electrical conductivity.<sup>[47]</sup> Notably, with the ingenious selection of metal ions and phosphorus-containing organic ligands, nanostructured TMPs embedded in porous carbon can be obtained by a simple one-step pyrolysis.<sup>[48]</sup> Also, the ionic liquid was also reported as the phosphorus source to fabricate the TMPs. With using the ionic liquid [BMIM]·PF<sub>6</sub> and metal salts as precursors, the one-step thermal reduction would induce the decomposition of [BMIM]·PF<sub>6</sub> and further yield TMPs/heteroatom-doped carbon architecture.<sup>[49]</sup> Meanwhile, the current bottleneck also lies in the common phosphating process required high reaction temperature and long time. Considering these issues, an ultrafast microwave-assisted strategy was recently developed to fabricate the nanostructured TMPs. With using carbon cloth as microwave susceptors and Prussian blue analogues/graphene oxides/NaH<sub>2</sub>PO<sub>2</sub> composite as the precursor, TMPs can be obtained within 20 s under microwave irradiation.<sup>[50]</sup> Moreover, a novel PH<sub>3</sub> plasma-assisted phosphating method was developed. This process was featured with a low temperature (250 °C) and short time (15 min), which can be extended to the synthesis of various TMPs.<sup>[51]</sup> Unfortunately, this process is utilizing high toxic PH<sub>3</sub> as the phosphorus source, and thus for large-scale application how to effectively prevent the leakage of PH<sub>3</sub> becomes an intractable work.

### 3. Fundamentals of Energy-Related Electrocatalytic Reactions on TMPs

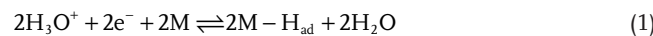
It is well known that theoretical calculation enables a robust way to screen a new catalyst. In general, the Gibbs adsorption free energy is regarded as a sole descriptor to theoretically evaluate catalysts' activity. In a prototypical computational simulation procedure, one electrocatalytic reaction is decoupled into several steps according to the corresponding reaction mechanism. In terms of correlating the adsorption free energies of each step with catalysts' electronic structure, the Gibbs adsorption energy change plot regarding the intrinsic activity of electrocatalysts is obtained. Therefore, understanding electrocatalytic reaction mechanisms is the prerequisite for combining theory with experiment. In this respect, we present fundamental insights into some energy-related electrocatalytic reactions, especially tending to elucidate the role of metal phosphides in these reactions. Meanwhile, by means of the advanced post-catalysis characterization techniques, the underlying surface reconstruction of TMPs during the electrocatalytic process is uncovered, reinforcing our understanding toward identifying the real active species. The main aim of this section is to correlate the reaction

mechanism, surface properties with the electrocatalytic activities and based on these, provides the modulated strategies for achieving better electrocatalytic performance.

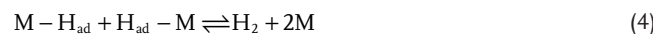
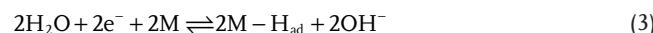
#### 3.1. Hydrogen Evolution Reaction

The electrocatalytic hydrogen evolution reaction is a well-studied electrochemical reaction. In principle, the general accepted HER process in acid or alkaline electrolyte undergoes two different reaction mechanisms.<sup>[9a]</sup> One of the possible reaction mechanism is the so-called Volmer-Tafel mechanism, in which the H<sub>3</sub>O<sup>+</sup> or H<sub>2</sub>O molecules are discharged on the surface to yield absorbed hydrogen atoms (H<sub>ad</sub>) (Reactions (1) and (3)). Then, due to relatively high coverage of H<sub>ad</sub> in the catalysts' surface, two adjacent H<sub>ad</sub> intermediates tend to bond together to produce molecular H<sub>2</sub>, as illustrated in Reactions (2) and (4). The other possible reaction mechanism is Volmer-Heyrovsky mechanism. The initial step is still the formation of absorbed hydrogen atom (H<sub>ad</sub>) by reduction of the H<sub>3</sub>O<sup>+</sup> or H<sub>2</sub>O molecule with the help of an electron (Reactions (5) and (7)). While in the following step the H<sub>ad</sub> coverage is low, the adsorbed hydrogen atom would couple with a new electron and another proton to generate molecular H<sub>2</sub> (Reactions (6) and (8)).<sup>[6c,26a]</sup>

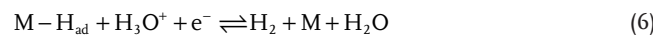
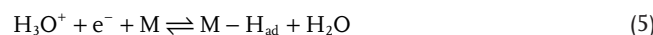
I: Volmer-Tafel reaction mechanism in acid electrolyte:



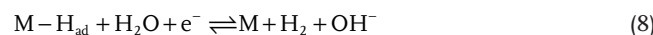
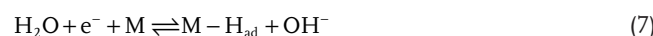
Or in alkaline electrolyte:



II: Volmer-Heyrovsky reaction mechanism in acid electrolyte:



Or in alkaline electrolyte:



In general, the rate-limiting step in HER process is associated with the affinity between reaction intermediates and the catalyst's surface. If a catalyst has a weak bonding strength with adsorbed H intermediate, the adsorption process (Volmer step) will dominate the HER process, while a catalyst binds the adsorbed H intermediate too strong, the desorption step (either the Heyrovsky step or the Tafel step) will be the rate-limiting step.<sup>[39]</sup> Thereby, an ideal HER catalyst should have moderate bonding with H<sub>ad</sub> intermediate, which can both facilitate the formation of intermediates and facilely desorb the formed molecular H<sub>2</sub>. By calculating the free energy change for H<sup>\*</sup>

adsorption on a catalyst surface, the obtained  $\Delta G_{H^*}$  can theoretically evaluate catalysts' HER activities. Accordingly, an ideal HER catalyst should have a moderate  $\Delta G_{H^*}$  of zero.<sup>[5b]</sup>

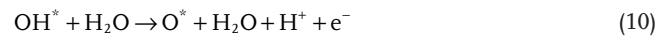
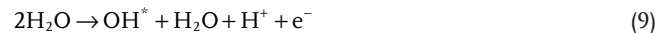
Recently, TMPs have attracted intensive attention to be good HER catalysts over a wide pH range. The first theoretical investigation of TMPs for catalyzing HER was reported by Rodriguez's group.<sup>[27a]</sup> In this study, the density functional theory (DFT) calculation was used to study energy changes for the HER on the [NiFe] hydrogenase, Ni<sub>2</sub>P (001), Pt (111), Ni (111), and other complexes. Because the Ni sites could bond hydrogen too strongly to allow the facile removal of H<sub>2</sub>, the slow kinetics of the HER was achieved on the Ni (111) surfaces. While once the Ni hollow sites of Ni<sub>2</sub>P (001) were poisoned by 1/3 of a monolayer H, the poisoned surface presented a high HER activity similar to that of the [NiFe] hydrogenase, potentially rendering Ni<sub>2</sub>P to be excellent HER catalyst. Guided by this, in 2013, Schaak's group prepared the Ni<sub>2</sub>P nanoparticles with highly exposed (001) facets and experimentally confirmed their outstanding HER activity.<sup>[27b]</sup> Since then, different kinds of nanostructured TMPs have sprung up, such as CoP,<sup>[52]</sup> MoP,<sup>[53]</sup> FeP,<sup>[54]</sup> etc. In general, a widely accepted viewpoint of HER catalytic mechanism on TMPs is that due to the stronger electronegativity of P atoms, the electrons can partially transfer from metal atoms to adjacent P atoms, generating partial negative charged ( $\delta^-$ ) phosphorus sites as the proton-acceptor and partial positive charged ( $\delta^+$ ) metal sites as the hydride-acceptor.<sup>[55]</sup> The metal and phosphorus in TMPs are not separated but synergistically facilitate the HER process. However, unlike the MoS<sub>2</sub> whose S–Mo–S edges were experimentally identified as the HER active site,<sup>[10b]</sup> direct evidence of identifying a real catalytic site on TMPs is still lacking.

Aside from ascertaining the catalytic active sites of TMPs, another urgent work is to comprehend the structural changes of the superficial active species during the electrocatalytic process. In the early stage, most TMPs are announced to be stable in both acidic and alkaline electrolyte during the electrochemical HER tests without changes in structure and composition. While with more focuses have been moved toward the post-HER characterizations, the possible changes on the catalysts' surface during the HER process gradually come to light.<sup>[56]</sup> Taken the cobalt-based phosphides as an example, generally, CoP prepared by high-temperature phosphidation methods are naturally oxidized on the surface. During HER, the surface oxidation layer is dissolved in the acidic electrolyte with exposing a fresh CoP surface, while in alkaline electrolyte a Co-rich phosphide surface is formed because of the preferential dissolution of phosphorus over cobalt.<sup>[57]</sup> Besides, different TMPs fabricated by different methods may involve varied structure reconstruction behavior in the electrochemical HER.<sup>[58]</sup>

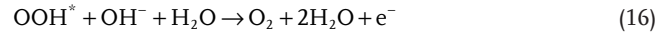
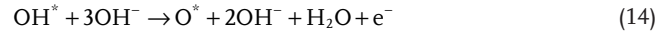
### 3.2. Oxygen Evolution Reaction

Oxygen evolution reaction (OER) is a pivotal step in many energy conversion and storage techniques, such as water electrolyzer and rechargeable metal–air batteries. Different from the HER only involved with a reaction intermediate, the OER undergoes the sequential formation of OH\*, O\*, OOH\* intermediates, thus rendering much more sluggish kinetics. As a generally accepted model claimed, the OER mechanism is displayed in Reactions (9)–(12) or (13)–(16).<sup>[59]</sup>

#### I. In acidic electrolyte:



#### II. In alkaline electrolyte:



In general, all of these steps are the thermodynamically uphill reaction and require robust catalysts to speed up reaction kinetics. Based on the theoretical calculation, the relationship between the catalysts' electronic structure and their activities have been established using the adsorption energies of corresponding intermediates as descriptors. To date, the state-of-the-art OER catalysts are iridium and ruthenium-based compounds.<sup>[5c]</sup> Nevertheless, their high costs surely limit large-scale applications. Thus, to substitute for noble OER catalysts, earth-abundant metal (oxy)hydroxides,<sup>[60]</sup> oxides,<sup>[61]</sup> phosphate compounds have successively emerged with comparable activity and sustainable stability.<sup>[62]</sup>

Although the first application of TMPs in electrocatalytic OER can date back to 1989,<sup>[63]</sup> the renaissance of TMPs in OER is accompanied by the thriving of TMPs catalysts in electrocatalytic HER. Interestingly, TMPs demonstrate excellent OER activities and stability in alkaline electrolyte, even surpassing that of corresponding metal oxides and (oxy)hydroxides. In fact, TMPs are thermodynamically less stable under oxidizing potentials and the containing phosphorus composition can dissolve into the electrolyte.<sup>[64]</sup> Ample post-catalysis analyses expound that real OER active species in TMPs are ascribed to the gradual formed amorphous or metastable metal oxide/hydroxide phases in the surface and the inner TMPs core may serve as the conductive scaffolds for the superficial active metal oxide/hydroxide species.<sup>[28a,65]</sup>

### 3.3. Oxygen Reduction Reaction

The sluggish reaction kinetics of oxygen reduction reaction render it to be a bottleneck in fuel cells and rechargeable metal–air batteries. Although the ORR and OER are reverse processes and share the same reaction intermediates (e.g., O\*, OH\*, OOH\*, etc.), the required catalysts differ from each other. For instance, Pt-based compounds are the most active ORR catalysts, while they present poor OER performance because of the formation of Pt oxides on the surface during OER.<sup>[66]</sup> Similarly,

the best OER catalysts are also not very effective for ORR. In general, the ORR contains a direct 4e pathway by reducing O<sub>2</sub> to H<sub>2</sub>O (in alkaline OH<sup>-</sup>), or an indirect 2-by-2e pathway by first yielding H<sub>2</sub>O<sub>2</sub> (in alkaline HO<sub>2</sub><sup>-</sup>), followed by a further reduction to H<sub>2</sub>O (in alkaline OH<sup>-</sup>).<sup>[67]</sup> To adopt which pathways dominate the ORR process is related to the oxygen adsorption mode on catalysts' surface. In fact, a direct four-electron pathway is highly desired to achieve high-efficiency electrocatalysis. Till now, metal–nitrogen doped carbon materials are widely investigated as promising alternatives to Pt for ORR electrocatalysis.<sup>[2b,c]</sup> It was thought to be that the formed metal–N<sub>4</sub> chelate bonds in the conjugated p-electron system are regarded as ORR-active sites.<sup>[26b]</sup> Given the fact that phosphorus and nitrogen belong to the same group and have similar chemical properties, the formed metal–phosphorus bonds in TMPs may be served as active sites for ORR. This hypothesis was first proved by Yu's group.<sup>[68]</sup> They experimentally uncovered excellent ORR catalytic activities on Fe–P–C materials and attributed their performance mainly to the formed Fe–P species. Following this trend, nanostructured TMPs were successively tried as the ORR catalysts with displaying comparable activity and durability.<sup>[69]</sup> But the corresponding reaction mechanism of TMPs in ORR and related structural changes need further investigations owing to the just emerging study of TMPs in this realm.

### 3.4. CO<sub>2</sub> Reduction Reactions (CO<sub>2</sub>RR)

With using intermittent renewable electricity, the electrochemical reduction of CO<sub>2</sub> offers a promising way to produce clean fuels and commodity chemicals. In general, the CO<sub>2</sub>RR is involved with complex reaction pathways with transferring various electrons and thus yielding different products including carbon monoxide (CO), formic acid (HCOOH), methane (CH<sub>4</sub>), methanol (CH<sub>3</sub>OH), etc.<sup>[11c]</sup> In general, the reaction products are mostly a mixture of carbon compounds, and the employed electrocatalyst and experimental parameters dominate which product will be a major part. Although CO<sub>2</sub>RR undergoes different reaction pathways under different conditions, a widely accepted reaction process includes: 1) chemical adsorption of CO<sub>2</sub> on electrocatalyst surface; 2) proton-coupled multiple-electron-transfer process to break C–O bonds and/or form C–H bonds and/or couple C–C bonds; 3) rearrangement of products' configuration and desorb products from the electrocatalyst surface to the electrolyte.<sup>[70]</sup> In consideration of the complexity of CO<sub>2</sub>RR, current bottlenecks regarding the electrocatalysts are lying in their unsatisfied catalytic activity, poor selectivity, and stability.

According to the thermodynamics theory, the equilibrium potentials for CO<sub>2</sub>RR are comparable to that of HER so that in aqueous solution most of TMPs are not considered as suitable CO<sub>2</sub>RR electrocatalysts because their favorable HER kinetics would largely suppress the CO<sub>2</sub>RR.<sup>[71]</sup> Therefore, in most cases, the potential roles of TMPs in electrocatalytic CO<sub>2</sub>RR are ignored. In 2018, Han and co-workers first investigated the CO<sub>2</sub>RR activity on metal phosphide under a nonaqueous solution.<sup>[32]</sup> With using the ionic liquid as supporting electrolyte, MoP/In-doped porous carbon composites can effectively facilitate the electroreduction of CO<sub>2</sub> into formic acid with a record-breaking faradaic efficiency and current density. Although the underlying catalytic

mechanism is not clear, this pioneering work surely enlarges the applications of TMPs in energy-related electrocatalysis.

### 3.5. Electrocatalysis in Li–S Batteries

Li–S batteries are endowed with intriguingly high energy density but practical application is handicapped by some intractable issues.<sup>[72]</sup> One of the major concerns come from the sluggish sulfur redox kinetics involving multielectron redox reactions and successive phase transformations.<sup>[73]</sup> In the case of the sulfur redox reaction kinetics not fast enough, lithium polysulfides intermediates (LPS) could be dissolved in electrolyte and diffused in the battery, thus rendering the loss of active materials and diminished electrochemical performance.<sup>[74]</sup> Till now, nanostructured carbonaceous materials are widely investigated as sulfur host materials for constructing sulfur composite cathodes.<sup>[75]</sup> However, limited by the weak physical interaction and incompatible surface affinity, nonpolar carbon cannot efficiently immobilize the charged sulfur species as well as facilitate its conversion.<sup>[76]</sup> In contrast, some polarized materials have been recognized as suitable sulfur hosts because they could not only confine LPS via chemical interactions but also presented excellent electrocatalytic activity by accelerating the sulfur redox kinetics.<sup>[77]</sup>

Among them, the first use of TMPs as the sulfur host was reported by Wang and co-workers.<sup>[34]</sup> In this study, MoP/CNTs and CoP/CNT were experimentally proved to be effective host material to trap polysulfide intermediates and boost their redox kinetics. Successively, in another study, they unveiled that the surface oxidation layers of CoP played a key role in their enhanced electrochemical performance.<sup>[78]</sup> Since then, studies of TMP-based sulfur host materials are prosperous.

## 4. Modulated Strategies for TMPs in Electrocatalytic HER, OER, and ORR

Although pure TMPs exhibit advantageous physicochemical properties for electrocatalysis, their practical performance is always unsatisfied. In real condition, the intrinsic ability of active sites and surrounded local environments simultaneously dominate the practical electrocatalytic activities.<sup>[79]</sup> More specifically, the active sites are responsible for the adsorption of reactants, bond breaking and forming, interfacial charge transfer, and desorption of products, while the local environment influences the accessibility of active sites, mass diffusion, together with the concentration gradient.<sup>[80]</sup> Therefore, from the perspective of catalysts' design, how to boost the catalytic activity in each active site and expose sufficient active sites, along with creating a favorable local environment should be taken into considerations. In view of considerable achievements in these aspects, herein, we summarize recent progress of modulated strategies for TMPs, including elemental doping, interfacial regulation, phase modification, structural engineering, and nanocarbon incorporation. We aim to demonstrate the effects of these modulated strategies and expound the elaborate reasons behind the enhanced electrocatalytic performance. Concurrently, some facing challenges and possible opportunities are briefly proposed.

#### 4.1. Elemental Doping

Elemental doping is a versatile strategy to boost the intrinsic activity of catalysts. In general, the incorporated foreign elements can modulate the catalysts' electronic structure, thus giving rise to significant changes in their physicochemical properties.<sup>[39,81]</sup> Besides, one typical feature of this strategy is that the optimal doping level of foreign elements can be predicted in advance by theoretical calculation, thus enabling a precise regulation of catalytic activity at the atomic scale.<sup>[82]</sup> In recent years, elemental doping engineered TMPs are reported everywhere, including cations doped TMPs, anions doped TMPs, along with anions and cations dual-doped TMPs. In regard to their contributions to electrocatalysis, the following part will be discussed case by case.

##### 4.1.1. Cations Doping

Although single TMPs have demonstrated their catalytic ability in many energy-related electrocatalysts fields, the further improvement of their catalytic performance is hindered by the limitations of intrinsic properties, such as relatively poor electrical conductivity, the unsuitable adsorption energy of intermediates, etc.<sup>[26a]</sup> To overcome these obstacles, incorporating foreign metal atoms into the single TMPs is proved to be useful. For example, Sun and co-workers reported that the introduction of nonelectroactive Zn into CoP could significantly boost HER performance.<sup>[83]</sup> As displayed in the free energy diagram (Figure 3a), the  $\Delta G_{H^*}$  on pristine CoP (101) was calculated as -0.36 eV, revealing that CoP surface bound the hydrogen intermediates too strong to facilely allow the desorption of H<sub>2</sub>. Interestingly, when trace Zn replaced Co atoms, the  $\Delta G_{H^*}$  on CoP was optimized and CoP with 8.3% Zn doping had the most moderate  $\Delta G_{H^*}$  of 0.08 eV. Since Zn had lower electron negativity, it could donate some electrons to adjacent P atoms and yield some electron-deficient cations. In order to compensate the electron deficiency, the surrounding Co would lose more electrons, thus weakening the bonding strength between Co atoms and adsorbed H. This thought can be verified by the density of state (DOS) calculation with a decrease of d-band center from -2.15 eV in CoP to -2.3 eV in 8.3% Zn-doped CoP (Figure 3b). As expected, 8.3% Zn doped CoP showed promoted HER activity with merely requiring 39 mV overpotential to drive a current density of 10 mA cm<sup>-2</sup>, which was better than that of pristine CoP (82 mV), Zn<sub>0.04</sub>Co<sub>0.96</sub>P (46 mV) and Zn<sub>0.13</sub>Co<sub>0.87</sub>P (66 mV) (Figure 3c). Beyond Zn, elements of Mn,<sup>[84]</sup> V,<sup>[85]</sup> Ce,<sup>[86]</sup> Cu,<sup>[87]</sup> Cr were successively recognized as good dopants.<sup>[88]</sup> The enhanced performance was ascribed to the enhanced electron interaction and optimized  $\Delta G_{H^*}$ . Besides, cations doping can also affect the local coordinated environment, thus influencing the electrocatalytic performance. For example, Dai and co-workers prepared the Ni@Ni<sub>2</sub>P–Ru nanorods via the wet chemical method.<sup>[89]</sup> The extended X-ray absorption fine structure (EXAFS) spectrum was utilized to uncover its surrounding environment (Figure 3d). Upon Ru doping, Ni–Ni peak at a position of 2.2 Å became stronger, indicating much retention of Ni (0) for fast electron transfer. Additionally, since the Ru–Ni coordination number was 1.8, this strong electron interaction between Ni and Ru could prevent the total phosphidation of Ni.

The Ni core together with the surface decorated Ru would optimize the  $\Delta G_{H^*}$  and facilitate electron transfer, accounting for the phenomenon that Ni@Ni<sub>2</sub>P–Ru displayed superior HER performance comparable to commercial Pt/C (Figure 3e).

Recently, TMPs have also shown excellent performance in electrocatalytic OER. Ample results indicated that their real catalytic active sites result from the surface formed oxyhydroxide while inner TMPs may serve as the conductive scaffolds. Therefore, for TMPs in OER, the cations regulation strategies actually regulate the electronic structure of derived oxyhydroxide. For example, Wang's group prepared hollow Mo-doped CoP nanoarrays and demonstrated their application in electrocatalytic OER.<sup>[90]</sup> Mo-doped CoP required 305 mV overpotential to reach a current density of 10 mA cm<sup>-2</sup> and had a low Tafel slope of 56 mV dec<sup>-1</sup>. The effect of Mo doping on the adsorption free energy of intermediates was further investigated via DFT calculations. For the potential kinetic limiting step (HO<sup>\*</sup>→O<sup>\*</sup>), the calculated free energy on Mo-doped  $\beta$ -CoOOH was as low as 0.59 eV, which was smaller than that of pure  $\beta$ -CoOOH (0.72 eV), expounding the reason behind the enhanced performance (Figure 3f). Similarly, Yi's group utilized scrap copper wires (SCW) as the substrate for the electrodeposition of amorphous TMPs.<sup>[91]</sup> Among them, bimetallic NiCoP/SCW displayed better electrocatalytic performance than that of monometallic NiP/SCW and CoP/SCW, only needing overpotentials of 178 mV (HER) and 220 mV (OER) to achieve the current density of 10 mA cm<sup>-2</sup>. Notably, this NiCoP/SCW exhibited good durability in electrocatalytic OER during the chronoamperometric test and cyclic voltammetry (CV) cycle test. Meanwhile, a post-OER characterization indicated that the morphology of this NiCoP electrode was finely maintained (Figure 3g inset). Besides bimetallic TMPs, trimetallic TMPs can display better electrocatalytic performance by multiple synergistic effects between metal cations. For instance, Liu's group prepared a series of TMPs containing different metal components (M = Fe, Co, Ni).<sup>[92]</sup> The OER activities of these catalysts followed the order of FeCoNiP >CoNiP>FeNiP>FeCoP>NiP>CoP>FeP (Figure 3h), manifesting that multiple cations doping was a feasible way to significantly improve the OER performance. Additionally, X-ray photoelectron spectroscopy (XPS) analysis further revealed that the introduction of tertiary metal into the bimetallic TMPs could induce more partial electron transfer from TM cations to P, thus benefiting the formation of high-valence-state TM species. This work surely pointed out the future orientation for the fabrication of TMPs catalysts by virtue of cations doping.

##### 4.1.2. Anions Doping

Anions doping is recognized to be effective in modulating the electrocatalytic activity, which can be divided into two categories. One is directly introducing anions, such as O, S, or Se into TMPs, thus leading to obvious changes in the electronic structure. While in another case, P is served as a dopant to substitute partial anions in other compounds. Since this process undergoes the formation of metal–phosphorus bonds, this item can be also included in this part. At the early stage, TMPs were widely investigated as the HDS electrocatalysts. In HDS, the most active sites are thought to be the surface phosphosulfide

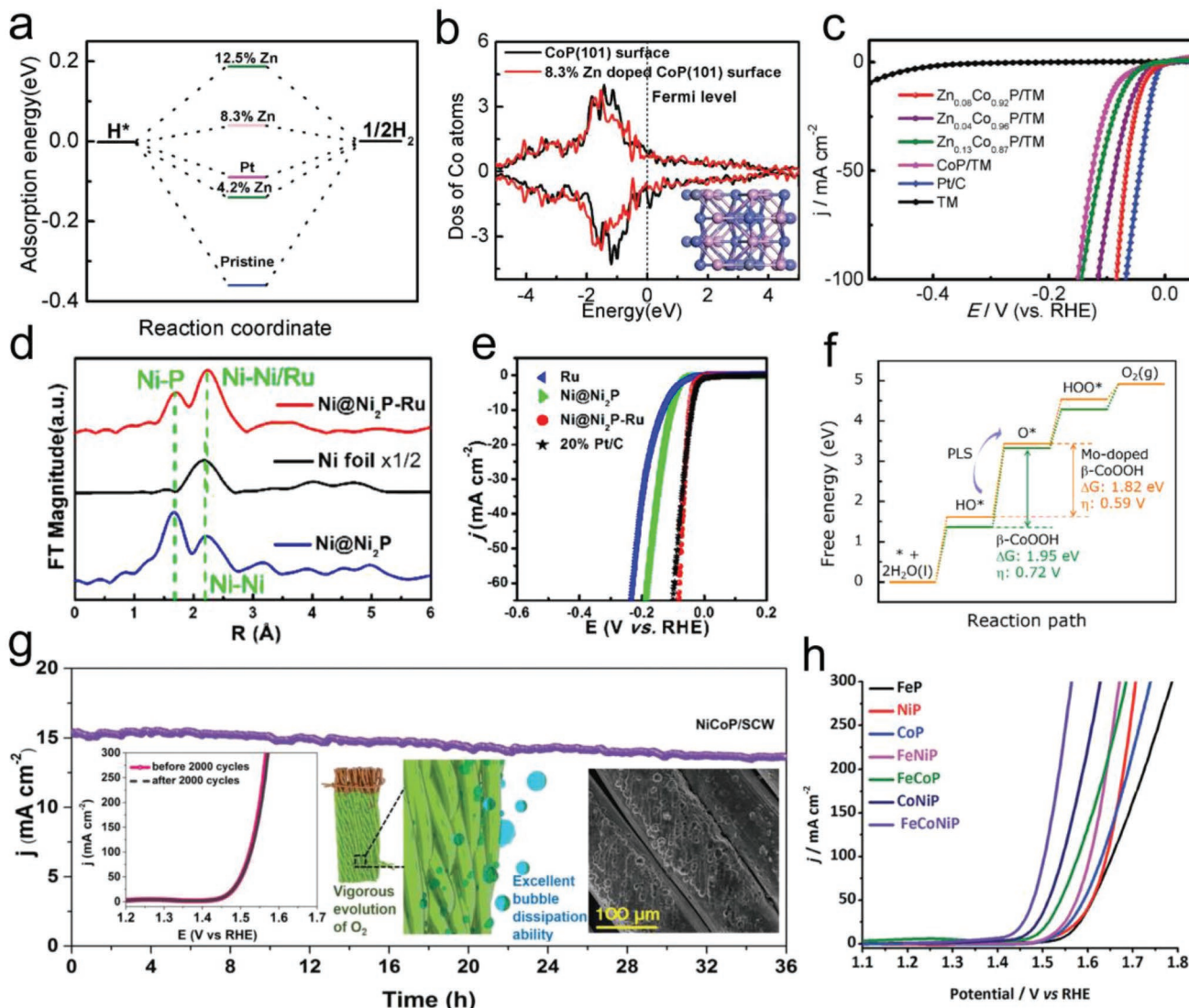


**Figure 3.** a) Diagram of free energies for  $\text{H}^*$  adsorption on (101) facet of pristine CoP and CoP (101) with different Zn doping contents. b) DOS results of Co atoms on the (101) facet of CoP and CoP with 8.3% Zn. (inserted picture: the crystal structure of CoP with 8.3% Zn doping). c) Polarization curves of  $\text{Zn}_x\text{Co}_{1-x}\text{P}/\text{titanium mesh}$  (TM) and contrastive samples obtained with a scanning rate of  $5 \text{ mV s}^{-1}$ . Reproduced with permission.<sup>[83]</sup> Copyright 2017, John Wiley and Sons. d) EXAFS spectra of Ni K-edge after Fourier transformation in Ni foil,  $\text{Ni@Ni}_2\text{P}$ , and  $\text{Ni@Ni}_2\text{P}-\text{Ru}$  samples. e) Polarization curves of  $\text{Ni@Ni}_2\text{P}-\text{Ru}$  and contrastive electrocatalysts. Reproduced with permission.<sup>[89]</sup> Copyright 2018, American Chemical Society. f) Diagram of standard free energies for OER pathways on (001) surfaces of  $\beta$ -CoOOH and Mo-doped  $\beta$ -CoOOH. Reproduced with permission.<sup>[90]</sup> Copyright 2018, Elsevier. g) The OER stability test of NiCoP electrode (inserted plots are polarization curves of NiCoP before and after 2000 CV cycles and corresponding morphology). Reproduced with permission.<sup>[91]</sup> Copyright 2018, John Wiley and Sons. h) Comparison of OER performance between pure TMPs and multiple-cations doped TMPs. Reproduced with permission.<sup>[92]</sup> Copyright 2018, Royal Society of Chemistry.

formed during reactions. Since both HDS and HER share a similar mechanism, the surficial phosphosulfide may be beneficial for the HER. Guided by this, a pioneering work of introducing S on the surface of MoP has been reported by Jaramillo's group.<sup>[93]</sup> This MoPS exhibited better activity and stability in electrocatalytic HER compared with pure MoP. Further analysis indicated that sulfur and phosphorus could mutually regulate electronic properties, and the existence of S lowered the degree of surface oxidation in TMPs, thus achieving a longer lifespan. This work proved that doping anion into TMPs could remarkably optimize electrocatalysts' activities. Different from the above strategy (anion doping in TMPs), Jin's group fabricated

the ternary cobalt phosphosulfide (CoPS) by doping P into pyrite-type  $\text{CoS}_2$ .<sup>[94]</sup> This work was originated from the thought about similar active metal centers existing in hydrogenase and the pyrite surface, and doping weak electronegativity P could modify the electron-donating character of the chalcogen ligands. According to the schematic illustration of crystal structures (Figure 4a inset), CoPS presented an analogous pyrite structure similar to  $\text{CoS}_2$ , but CoPS had the  $\text{Co}^{3+}$  octahedra and dumbbells with a uniform distribution of  $\text{P}^{2-}$  and  $\text{S}^-$  atoms. This minor difference in structure resulted in the more thermoneutral hydrogen adsorption at the CoPS's active sites (Figure 4a). Thus, nanostructured CoPS displayed excellent performance for

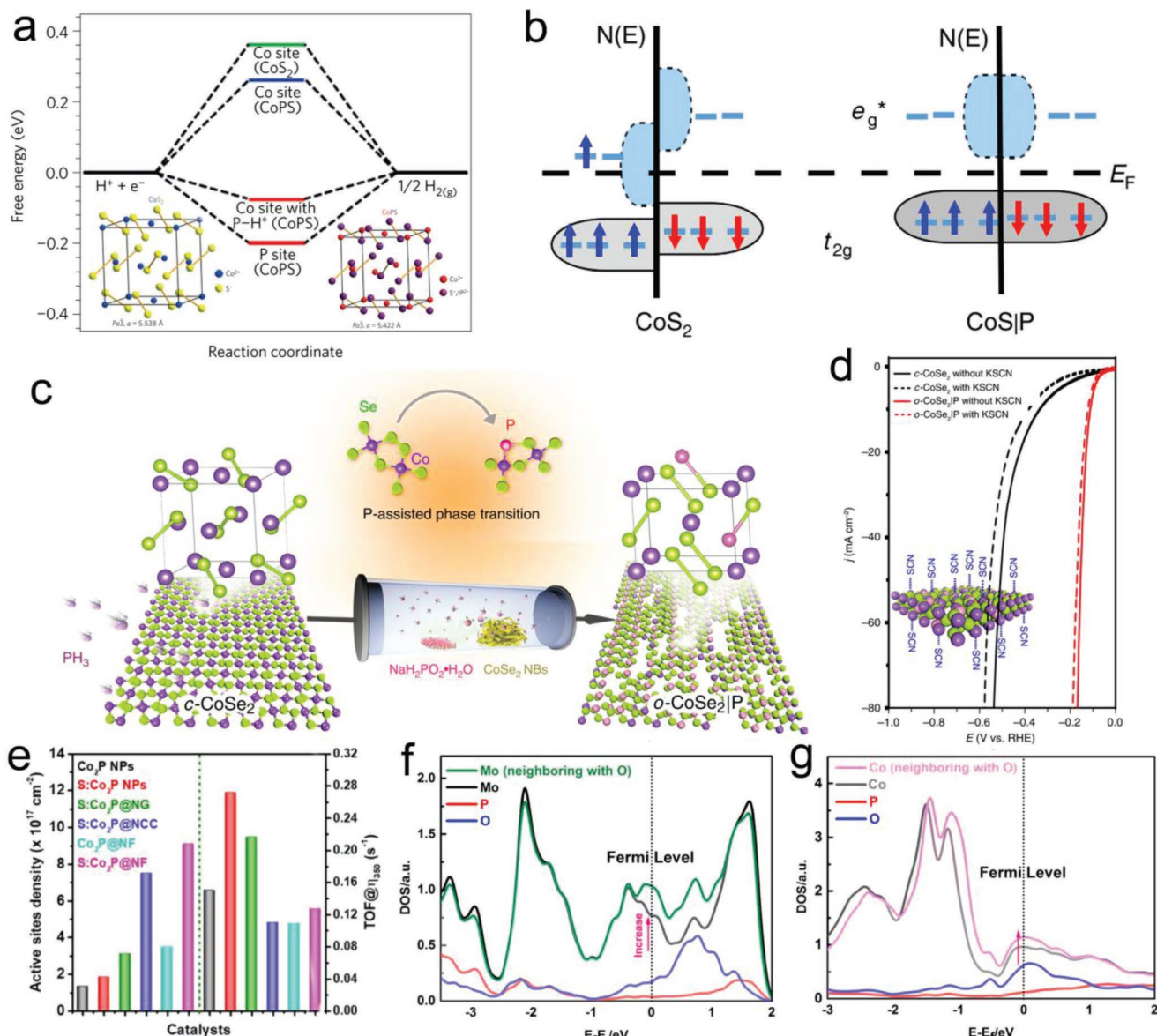


**Figure 4.** a) Differences of free energies for  $\text{H}^*$  adsorption on Co sites and P sites in CoPS and  $\text{CoS}_2$  (inserted picture: corresponding crystal structures). Reproduced with permission.<sup>[94]</sup> Copyright 2015, Nature Publishing Group. b) Diagram of the frontier molecular orbitals for electron occupation in  $\text{CoS}_2$  and  $\text{CoS|P}$ . Reproduced with permission.<sup>[95]</sup> Copyright 2016, Nature Publishing Group. c) The schematic illustration of the P-doping-assisted structural phase transition. d) Poisonous effects of  $\text{SCN}^-$  ions on HER performance for  $\text{c-CoSe}_2$  and  $\text{o-CoSe}_2|\text{P}$ . Reproduced with permission.<sup>[96]</sup> Copyright 2018, Nature Publishing Group. e) The calculated number of active sites (left) and TOF (right) in  $\text{S:Co}_2\text{P}$ . Reproduced with permission.<sup>[97]</sup> Copyright 2018, American Chemical Society. DOS of f) O-doped MoP and g) O-doped CoP. Reproduced with permission.<sup>[46a]</sup> Copyright 2016, American Chemical Society.

electrocatalytic HER, needing 48 mV overpotential to achieve the current density of  $10 \text{ mA cm}^{-2}$  in  $0.5 \text{ M H}_2\text{SO}_4$ . Successively, Wang's group prepared the pyrite-structured  $\text{CoS|P}$  on carbon nanotubes (CNT) via a facile three-step method.<sup>[95]</sup> Besides its higher activity in electrocatalytic HER, this  $\text{CoS|P/CNT}$  also demonstrated better durability than that of pure  $\text{CoS}_2/\text{CNT}$ . They further performed the theoretical calculation to illustrate this phenomenon. From the energy-level diagrams of the frontier molecular orbitals, pure  $\text{CoS}_2$  was instability because its highest occupied states were of antibonding nature. While once replacing some S by P, the antibonding  $e_g^*$  orbitals were

depleted (Figure 4b), thus achieving endurable stability with stronger chemical bonds between Co atoms and surrounding ligands. The common feature in the above works is the substitution process neither alters the crystal structure nor lattice parameters because of the very similar atomic sizes between S and P. While an unusual result of phase transformation was discovered by Yu's group.<sup>[96]</sup> They observed that phosphorus doping could induce a structural transition from pyrite-type cubic  $\text{CoSe}_2$  ( $\text{c-CoSe}_2$ ) to marcasite-type orthorhombic  $\text{CoSe}_2|\text{P}$  ( $\text{o-CoSe}_2|\text{P}$ ). As depicted in Figure 4c, when cubic  $\text{CoSe}_2$  was annealed at  $400^\circ\text{C}$ , there were some vacancies generated by the

loss of partial Se, and these vacancies could be further occupied by in situ decomposed P. This substitution would lead to the formation of closer Co–P interactions and longer Se–Se(P) pairs, thus driving the rotation of Se–Se(P) pairs to yield orthorhombic  $\text{CoSe}_2|\text{P}$ . As compared with c-CoSe<sub>2</sub>, o-CoSe<sub>2</sub>||P demonstrated better electrocatalytic HER performance with an overpotential of 104 mV to deliver a current density of 10 mA cm<sup>-2</sup> and a small Tafel slope of 69 mV dec<sup>-1</sup> in the alkaline electrolyte. An important implication of this work was that they found the P sites in o-CoSe<sub>2</sub>||P directly contributed to its high HER activity. They utilized SCN<sup>-</sup> to poison the metal-centered catalytic sites (Figure 4d). It was evident that in c-CoSe<sub>2</sub> the poisoning effect led to significant degradation of HER performance, while this condition was totally different in o-CoSe<sub>2</sub>||P. Successively, Lee and co-workers fabricated the sulfur-doped dicobalt phosphide (S:Co<sub>2</sub>P) by a facile thiourea-phosphate-assisted strategy.<sup>[97]</sup> This S:Co<sub>2</sub>P demonstrated higher HER and OER performance in contrast with pure Co<sub>2</sub>P. Interestingly, in view of its high OER activity, they estimated the density of Co<sup>2+</sup> active sites and further calculated the turnover frequency (TOF). As displayed in Figure 4e, S-doped Co<sub>2</sub>P samples possessed more active sites and higher TOF compared with pure Co<sub>2</sub>P, revealing that the introduction of S could both proliferate the number of active sites and enhance the intrinsic catalytic activity. Besides S and Se, doping oxygen into TMPs can also regulate their electrocatalytic properties. For example, Li's group fabricated a series of O-doped MoP and CoP on reduced graphene oxides (RGO) via pyrolyzing the phytic acid cross-linked complexes.<sup>[46a]</sup> It was verified that doping oxygen atoms into TMPs could activate the active sites through the elongation of the M–P bonds. Meanwhile, upon O substitution, the metal atoms adjacent to the O atoms also presented an increased density of states (DOS) at the Fermi level as compared with the residual ones, manifesting their enhanced electrical conductivity (Figure 4f,g). Benefited from these merits, in 1 M KOH, the O-doped MoP@RGO could effectively catalyze HER with requiring 93 mV overpotential to produce a current density of 20 mA cm<sup>-2</sup>, while O-doped CoP@RGO facilitated the OER with only needing 280 mV overpotential to deliver a current density of 10 mA cm<sup>-2</sup>. Till now, most of the doped anions in TMPs are the chalcogens. It is anticipated that doping new anions, such as F, N, etc. may generate positive results. Additionally, binary anion doping can also contribute to a remarkable catalytic performance but it is rarely reported.

#### 4.1.3. Anions and Cations Dual Doping

In light of the remarkably promotional catalytic performance caused by elemental doping, cations and anions dual-doping strategy is also quite appealing. In common, the cations and anions dual-doping can engender dual synergistic effects on modulating adsorption energy, electrical conductivity, etc. In this regard, Zhang and co-workers used the hexagonal NiS (0001) as the pristine model and investigated the effect of dual doping Fe and P on their electronic structure via DFT calculations.<sup>[98]</sup> As demonstrated in Figure 5a, the replacement of one topmost surface Ni/S atom by Fe and P atoms could generate the NiFeS (Figure 5a-a3) and NiSP (Figure 5a-a4), and NiFeSP (Figure 5a-a5, a6), respectively. The results revealed that the

P atom preferred to be doped on the inner layer sites while the Fe doping would cause segregation of the inner P to the surface. Based on these optimized models, they further calculated the  $\Delta G_{\text{H}^*}$  to theoretically compare their catalytic HER performance (Figure 5b). The  $\Delta G_{\text{H}^*}$  on pristine NiS (0001) is -1.02 eV, and single doping either Fe or P did not lead to a moderate  $\Delta G_{\text{H}^*}$ . Interestingly, once Fe and P are codoped on NiS surface, a preferable  $\Delta G_{\text{H}^*}$  of -0.13 eV was obtained. We note here that although the starting model in this work is TMSs rather than TMPs, it still offers some reference for anion and cation dual doping. While Qiao's group experimentally demonstrated the feasibility of this dual doping strategy by reporting the controllable synthesis of Fe- and O-doped Co<sub>2</sub>P nanowires (CoFePO) via chemical bath deposition and post phosphidation strategy.<sup>[99]</sup> This CoFePO electrode could both markedly facilitate HER and OER. As displayed in Figure 5c, the higher TOF values for HER (16.87 s<sup>-1</sup>) and OER (6.8 s<sup>-1</sup>) were observed on CoFePO in contrast with other counterparts, further stating the vital roles of Fe and O incorporation in accelerating reaction kinetics. Successively, He's group fabricated the partially oxidized Ni<sub>0.75</sub>Fe<sub>0.25</sub>P<sub>2</sub> nanosheets by a scalable two-step method.<sup>[100]</sup> Regarding the electrocatalytic OER performance (Figure 5d), this O-Ni<sub>0.75</sub>Fe<sub>0.25</sub>P<sub>2</sub> only required the overpotential of 155 mV to reach a current density of 10 mA cm<sup>-2</sup>, which was lower than that of Ni<sub>2</sub>P (180 mV), Ni<sub>0.75</sub>Fe<sub>0.25</sub>(OH)<sub>y</sub> (280 mV) and Ni<sub>0.75</sub>Fe<sub>0.25</sub>O<sub>y</sub> (430 mV). It also presented the lowest Tafel slope of 55 mV dec<sup>-1</sup> among these contrastive catalysts. More importantly, the authors unambiguously elucidated the effects of Fe, O dopants on their enhanced OER performance via DFT calculation. The free energy diagram of OER ( $U = 1.23$  V) upon pure Ni<sub>2</sub>P, Fe-doped Ni<sub>2</sub>P (Ni<sub>0.75</sub>Fe<sub>0.25</sub>P<sub>2</sub>) and partially oxidized Ni<sub>0.75</sub>Fe<sub>0.25</sub>P<sub>2</sub> (O-Ni<sub>0.75</sub>Fe<sub>0.25</sub>P<sub>2</sub>) surfaces were displayed in Figure 5e. It was found on pure NiP<sub>2</sub> surface, both the third step (O<sup>\*</sup>→HOO<sup>\*</sup>) and the fourth step (HOO<sup>\*</sup>→O<sub>2</sub>) were uphill in free energy, suggesting that the OER was kinetically limited by these two steps. While for Ni<sub>0.75</sub>Fe<sub>0.25</sub>P<sub>2</sub>, the Fe incorporation was a “double-edged sword.” Upon Fe incorporation, the rate-limiting step was reduced because the third step (O<sup>\*</sup>→HOO<sup>\*</sup>) became downhill. But it should be also noted that there was an extremely high energy barrier in the fourth step and the formed HOO<sup>\*</sup> in the third step could easily decompose into O<sup>\*</sup> and HO<sup>\*</sup>, which also brought about detrimental effects on the OER. Furthermore, once introducing O into Ni<sub>0.75</sub>Fe<sub>0.25</sub>P<sub>2</sub>, the free energy for each step underwent a remarkable variation. The free energy of the fourth step turned to be downhill and the overall OER reaction kinetics was only limited by the third step, thus resulting in higher OER performance. This work expounds the function of dual elemental doping on phosphorus-rich TMPs and provides an insight into the OER mechanism. In contrast, Kim and co-workers anchored the quaternary (Co<sub>1-x</sub>Ni<sub>x</sub>)(S<sub>1-y</sub>P<sub>y</sub>)<sub>2</sub> hybrids on graphene through a wet chemical route, followed by gas sulfuration and subsequent phosphidation methods.<sup>[101]</sup> As shown in Figure 5f, this (Co<sub>1-x</sub>Ni<sub>x</sub>)(S<sub>1-y</sub>P<sub>y</sub>)<sub>2</sub>/G presented the doughnut-like morphology with a diameter of 3–4 μm. It could be seen the uniform distribution of Co, Ni, S, and P elements on this sample (Figure 5g). When utilized as catalysts, this (Co<sub>1-x</sub>Ni<sub>x</sub>)(S<sub>1-y</sub>P<sub>y</sub>)<sub>2</sub>/G composite displayed superior electrocatalytic performance, only needing overpotentials of 117 and 285 mV to drive the current density of 10 mA cm<sup>-2</sup>,

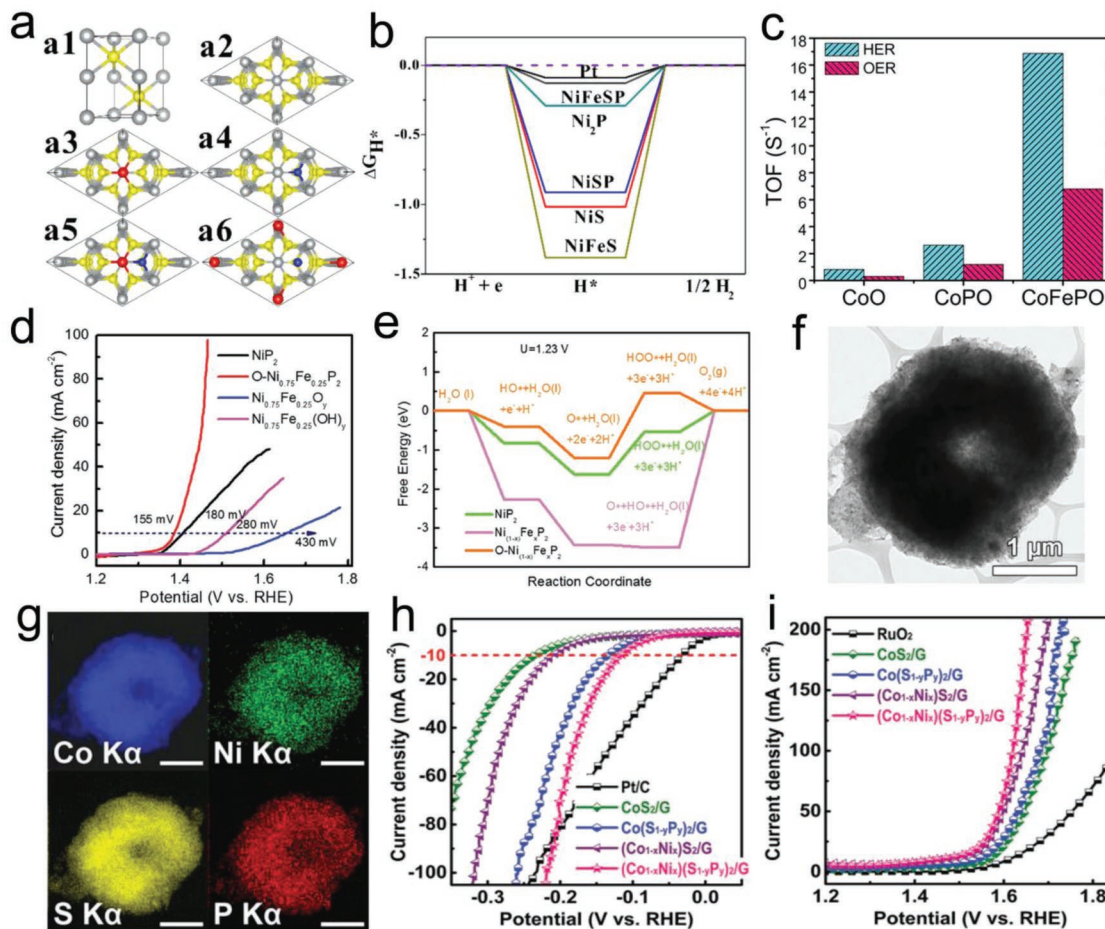


**Figure 5.** a) Crystal structures of a1,a2) NiS, a3) NiFeS, a4) NiSP, a5,a6) NiFeSP from different views. b) Comparison of free energies for HER on Pt, NiFeSP, NiFeS, NiSP, NiS, and Ni<sub>2</sub>P catalysts. Reproduced with permission.<sup>[98]</sup> Copyright 2017, American Chemical Society. c) Calculated values of the turnover frequency on CoO, CoPO, and CoFePO for HER and OER. Reproduced with permission.<sup>[99]</sup> Copyright 2016, American Chemical Society. d) Polarization curves of O-Ni<sub>0.75</sub>Fe<sub>0.25</sub>P<sub>2</sub> and contrastive samples for OER. e) Diagram of free energies on surfaces of NiP<sub>2</sub>, Ni<sub>0.75</sub>Fe<sub>0.25</sub>P<sub>2</sub>, and O-Ni<sub>(1-x)</sub>Fe<sub>x</sub>P<sub>2</sub> calculated at U=1.23 V. Reproduced with permission.<sup>[100]</sup> Copyright 2018, John Wiley and Sons. f) The TEM image of (Co<sub>1-x</sub>Ni<sub>x</sub>)(S<sub>1-y</sub>P<sub>y</sub>)<sub>2</sub>/G. g) Elemental distribution images of (Co<sub>1-x</sub>Ni<sub>x</sub>)(S<sub>1-y</sub>P<sub>y</sub>)<sub>2</sub>/G. h) Polarization curves of (Co<sub>1-x</sub>Ni<sub>x</sub>)(S<sub>1-y</sub>P<sub>y</sub>)<sub>2</sub>/G and contrastive samples in h) HER and i) OER. Reproduced with permission.<sup>[101]</sup> Copyright 2018, John Wiley and Sons.

along with Tafel slopes of 85 and 105 mV dec<sup>-1</sup> for HER and OER, respectively (Figure 5h,i). In brief, dual doping of anion and cation enables a robust way to engineer TMPs with a preferable electronic structure, and these dual doped electrocatalysts usually display better electrocatalytic performance in comparison with single doped samples. Despite significantly promotional effects caused by the dual doping strategy, there are still some critical challenges needed to be resolved. For instance, the preparation of dual doping TMPs is generally involved with multistep methods, which is not beneficial for their large-scale applications. In addition, the doping levels of corresponding anions and cations are also essential for achieving considerable electrochemical performance but it is rarely studied.

#### 4.2. Interfacial Engineering

It is widely recognized that the rational design of multicomponent heterogeneous structure enables a promising way to

access electrocatalysts with significantly boosted electrocatalytic activities.<sup>[102]</sup> Since each component/phase has direct physical contact, the corresponding physicochemical properties in the interface would be substantially different from the bulk phase.<sup>[103]</sup> More importantly, this kind of hybrid electrocatalysts usually displays strong interfacial interactions, leading to enhanced electron conductivity, optimized adsorption energy, and fast reaction kinetics. With the help of theoretical calculation and surface/interface characterization techniques, these interfacial interactions between each component are uncovered, including the electronic coupling effect and interfacial synergistic effect. In view of considerable achievements in this field, herein, we highlight some cases to demonstrate recent advances in interfacial engineered TMPs and attempt to establish a relationship between interfacial properties of catalysts and their enhanced electrocatalytic activities.

Regarding the electronic coupling effect, it could trigger the redistribution of electrons on the heterointerfaces. As a consequence, the interfacial electronic structure would be tuned,

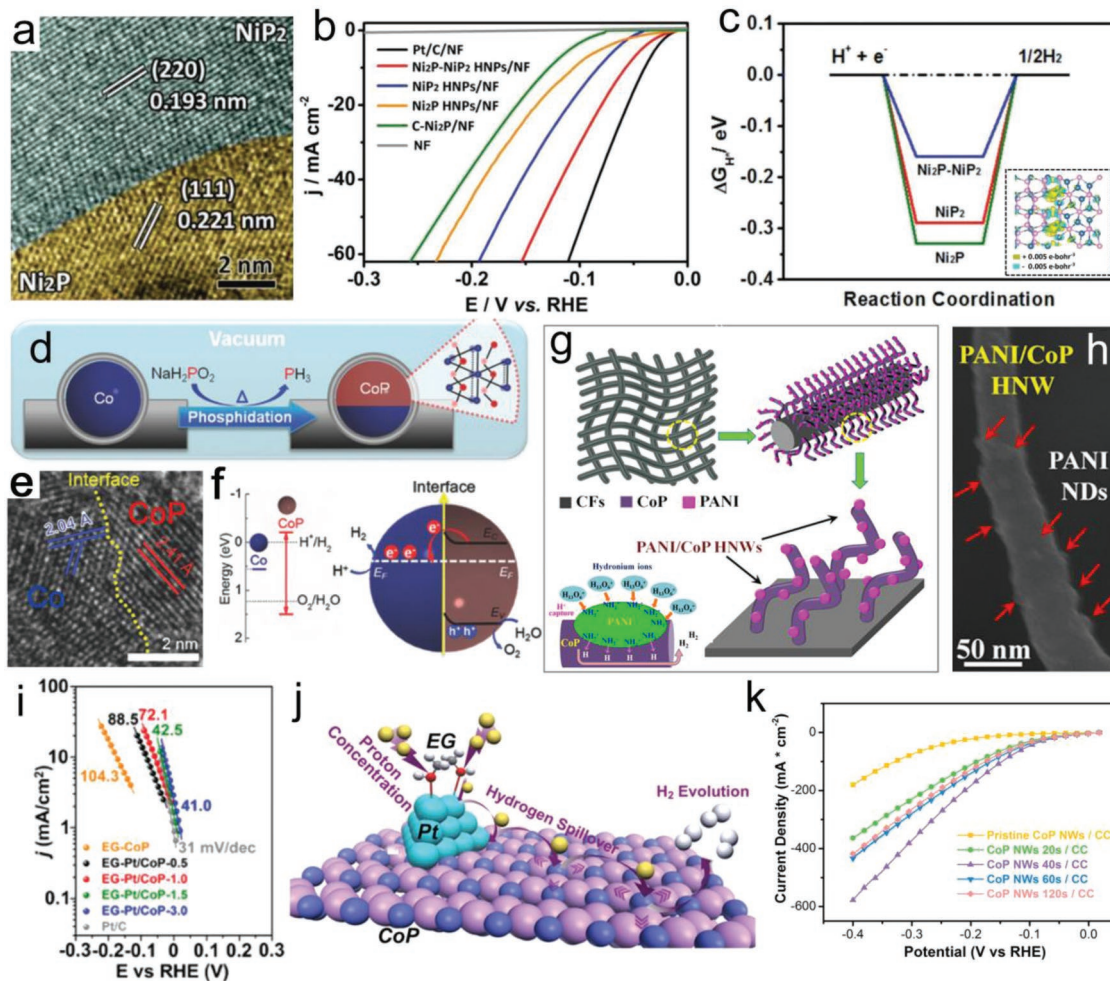


**Figure 6.** a) The TEM image of Ni<sub>2</sub>P–NiP<sub>2</sub> polymorphs with an obvious interface. b) HER performances of Ni<sub>2</sub>P–NiP<sub>2</sub> polymorphs and contrast samples. c) Diagram of  $\Delta G_{H^*}$  for pure Ni<sub>2</sub>P, Ni<sub>2</sub>P and Ni<sub>2</sub>P–NiP<sub>2</sub> (inset plot: distribution of electron charge density at the interface of Ni<sub>2</sub>P–NiP<sub>2</sub>). Reproduced with permission.<sup>[104]</sup> Copyright 2018, John Wiley and Sons. d) Synthetic routes for Janus Co/CoP nanoparticles. e) The TEM image of Co/CoP nanoparticles with a clear interface. f) Electronic structures of metallic Co, CoP, and the Co/CoP-based Mott–Schottky contact ( $E_F$ : work function;  $E_C$ : conduction band;  $E_V$ : valence band) Reproduced with permission.<sup>[108]</sup> Copyright 2017, John Wiley and Sons. g) The fabrication step of PANI/CoP hybrid nanowires (inset: schematic illustration of the improved HER by capturing H<sup>+</sup> through the surface-protonated NH<sub>2</sub><sup>+</sup>). h) The SEM image of PANI/CoP hybrid nanowires. Reproduced with permission.<sup>[110]</sup> Copyright 2018, American Chemical Society. i) Tafel slopes of EG-Pt/CoP and 20% Pt/C catalysts. j) Schematic catalytic mechanism of EG-Pt/CoP for HER. Reproduced with permission.<sup>[111]</sup> Copyright 2019, Royal Society of Chemistry. k) Polarization curves of CoP NWs/CC catalysts with different oxygen plasma engraving time of 0, 20, 40, 60, 120 s in alkaline media. Reproduced with permission.<sup>[114]</sup> Copyright 2018, John Wiley and Sons.

giving rise to the enhanced electron conductivity and optimized adsorption energy toward intermediates. In this regard, a representative work has been done by Guo and co-workers.<sup>[104]</sup> They constructed the hollow Ni<sub>2</sub>P–NiP<sub>2</sub> polymorphs heterointerface by the phosphidation of NiS<sub>2</sub> single-crystal precursor. From the TEM image (Figure 6a), it could be seen the interface between (111) plane of Ni<sub>2</sub>P and the (220) plane of NiP<sub>2</sub>, with the lattice fringe spacings of 0.221 and 0.193 nm, respectively. When utilized as the HER catalyst, this Ni<sub>2</sub>P–NiP<sub>2</sub> polymorphs electrode demonstrated excellent electrocatalytic performance with only needing 59.7 mV overpotential to afford a current density of 10 mA cm<sup>-2</sup> and a Tafel slope of 58.8 mV dec<sup>-1</sup> (Figure 6b). The HER performance achieved on Ni<sub>2</sub>P hollow nanoparticles (104.8 mV@10 mA cm<sup>-2</sup> and Tafel slope of 85.3 mV dec<sup>-1</sup>), NiP<sub>2</sub>

hollow nanoparticles (82.2 mV@10 mA cm<sup>-2</sup> and Tafel slope of 70.3 mV dec<sup>-1</sup>), and commercial solid Ni<sub>2</sub>P nanoparticles (130.8 mV@10 mA cm<sup>-2</sup> and Tafel slope of 87.7 mV dec<sup>-1</sup>). Successively, the theoretical calculations unveiled a significant role of interfacial effect in Ni<sub>2</sub>P–NiP<sub>2</sub> heterointerface (Figure 6c). Obviously, there was a more moderate H adsorption free energy (close to zero) on Ni<sub>2</sub>P–NiP<sub>2</sub> (-0.161 eV) as compared with that of Ni<sub>2</sub>P (-0.326 eV) and NiP<sub>2</sub> (-0.290 eV), manifesting a preferable H<sup>\*</sup> adsorption strength on Ni<sub>2</sub>P–NiP<sub>2</sub>. The difference in H adsorption free energy between Ni<sub>2</sub>P–NiP<sub>2</sub> and single components resulted from the strong charge redistribution occurred at the Ni<sub>2</sub>P–NiP<sub>2</sub> interface (Figure 6c inset). This charge redistribution endowed Ni<sub>2</sub>P–NiP<sub>2</sub> polymorphs with optimized valence electron state and enhanced electrical conductivity, thereby showing better electrocatalytic

activity. Meanwhile, this electronic coupling effect in the interface could be also found in  $\text{Ni}_2\text{P}/\text{Ni}_3\text{S}_2$  heteronanoflake arrays,<sup>[105]</sup>  $\text{Ni}_2\text{P}-\text{VP}_2$  heterogeneous nanocomposites,<sup>[106]</sup> and  $\text{Ni}_2\text{P}/\text{Fe}_2\text{P}$  heterostructure.<sup>[107]</sup> As a typical heterostructure, the Janus nanoparticles always present unique physicochemical properties because their building block contains asymmetric shapes or compositions. In general, the highly coupled interface between the two facets offers an ideal paradigm to study the interfacial effects on electrocatalysis. For example, Chen and co-workers fabricated the Janus Co/CoP via a controllable vacuum-diffusion method (Figure 6d).<sup>[108]</sup> As depicted in the high-resolution TEM image (Figure 6e), the Co facet (lattice fringe spacing: 2.04 Å) and CoP facet (lattice fringe spacing: 2.41 Å) presented a clear interface. It was worth noting that the Janus Co/CoP had a metal–semiconductor contact with forming a Mott–Schottky heterojunction. Since semiconductor CoP had a much lower work function than that of metallic Co, the electron could transfer from CoP to Co through the Co/CoP interface, rendering a higher electron-donating ability for proton reduction on Co facet. Meanwhile, the electron redistribution at interfaces also pulled down the valence band of CoP (Figure 6f), resulting in stronger oxidation ability of CoP facet for OER. Therefore, profited from the electronic coupling effect, this Janus-type Co/CoP demonstrated remarkable HER and OER activities over a wide pH range. Besides this, the interfacial electronic coupling effect can be also achieved on a core–shell structure. For instance, Wang's group prepared the iron–iron phosphide core–shell nanoparticles on carbon nanotubes ( $\text{Fe}@\text{FeP/CNT}$ ) and demonstrated its application in electrocatalytic HER.<sup>[109]</sup> To deliver a current density of 10 mA cm<sup>-2</sup>, the  $\text{Fe}@\text{FeP/CNT}$  only required 53 mV overpotential, suppressing the performance of Fe/CNT and FeP/CNT. Its excellent performance was attributed to more favorable hydrogen adsorption free energy caused by electron transfer from the Fe core to the FeP shell.

Moreover, interfacial engineering can also induce the synergistic effect between heterocomponents, dramatically facilitating the electrocatalytic reaction kinetics. In general, the added component can promote the evolution of reactant into reaction intermediates or alter reaction pathways, etc., thereby making the electrocatalytic process much easier. In fact, constructing these multicomponent catalysts with strong interfacial synergies is based on an in-depth understanding of the reaction mechanism so that it can accordingly modulate the rate-limiting step and speed up the overall reaction rate. For example, Li and co-workers fabricated the PANI/CoP hybrid nanowires (HNWs) via a feasible three-step method, in which conductive polymers polyaniline (PANI) nanodots were uniformly anchored on CoP nanowires (Figure 6g,h).<sup>[110]</sup> This PANI/CoP hybrid demonstrated a Pt-like electrocatalytic HER performance in acidic electrolyte with a low onset potential of 15 mV. Interestingly, the incorporation of PANI dramatically decreased the Tafel slope from 111.8 mV dec<sup>-1</sup> in CoP to 46.3 mV dec<sup>-1</sup> in PANI/CoP at high current density (10–40 mA cm<sup>-2</sup>), manifesting that the PANI nanodots affected the kinetic radical step. Hence, they performed further experiments to unveil a critical role of PANI. As depicted in Figure 6g inset, in PANI, the amine groups with lone electron pairs could efficiently capture proton ( $\text{H}^+$ ) from hydronium ions ( $\text{H}_3\text{O}_6^+$ ) to protonated amine groups. And the protonated amine groups were more

easily electroreduced into  $\text{H}_2$  on CoP as compared with hydronium ions. In other words, the existence of PANI nanodots was able to weaken the shackles of coordinated water molecules around protons to boost the HER. This work offers a representative case to demonstrate how the interfacial synergistic effect between heterointerface regulates the reaction kinetics. More recently, Qu and co-workers reported an impressive work by regulating the reaction pathway to expedite the acidic HER kinetics.<sup>[111]</sup> Their motivation was to design a hybrid catalyst with Pt and CoP as the favorable  $\text{H}^*$  adsorption and  $\text{H}_2$  desorption component, respectively. Interestingly, they found only under ethylene-glycol (EG) ligand environment the HER kinetics on this Pt/CoP hybrid could be dramatically facilitated. As shown in Figure 6i, with adding ethylene glycol ligand, the Tafel slope on Pt/CoP showed a decreasing trend from 104.3 to 41.0 mV dec<sup>-1</sup> with an increasing Pt content from 0 to 3.0 wt%, while this phenomenon was not observed in pure Pt/CoP. Following control experiments and DFT calculation expounded that EG could not only enrich the proton concentrations around Pt but also facilitate the hydrogen spillover from hydrogen-enriched Pt to hydrogen-deficient CoP, thus achieving promoted HER kinetics. Based on this result, a possible reaction mechanism on EG-Pt/CoP was illustrated in Figure 6j.

Additionally, compared with HER proceeding in acidic media, the alkaline HER is much more sluggish because protons are stemmed from the disassociation of water molecules rather than from hydronium ions in acidic electrolyte.<sup>[112]</sup> Although TMPs are capable of adsorbing and recombining the reactive  $\text{H}_{\text{ad}}$  intermediate, it is ineffective for the water dissociation steps in alkaline HER process resulted from the improper binding affinities with hydroxyl species.<sup>[113]</sup> To address this issue, Wu and co-workers made a decent work by using oxygen plasma to engrave the CoP nanowires (NWs), in which this process led to the formation of a thin layer  $\text{CoO}_x$  on CoP surface.<sup>[114]</sup> When tried as the electrocatalyst for HER, CoP nanowires with an etching time for 40 s displayed nearly fourfold improved activity than that of pristine CoP NWs, only requiring an overpotential of 146 mV to attain a current density of 100 mA cm<sup>-2</sup> in 1 M KOH (Figure 6k). From the X-ray absorption near-edge structure measurements and XPS test, it was found that the  $\text{CoO}_x$  sites were highly positive charged and had the unfilled d-orbital in  $\text{Co}^{n+}$  so that it could offer strong binding affinities with the –OH groups, while adjacent CoP sites were served as the  $\text{H}_{\text{ad}}$  sites. This kind of synergy between CoP and  $\text{CoO}_x$  would dramatically expedite the dissociation of water molecules, thus benefiting the overall HER kinetics. Successively, similar interfacial synergistic effects were also observed on  $\text{Ni}_5\text{P}_4@\text{NiCo}_2\text{O}_4$ ,<sup>[115]</sup>  $\text{Co}_2\text{P}-\text{Ni}_2\text{P}/\text{TiO}_2$ ,<sup>[116]</sup> and sc- $\text{Ni}_2\text{P}^{\delta-}/\text{NiHO}$ ,<sup>[117]</sup> in which metal oxide/hydronium oxide was incorporated to manipulate the water dissociation kinetics. We note here that so far most of the interfacial engineered TMPs are designed for HER while rarely reported in OER or ORR,<sup>[118]</sup> probably due to their more complex reaction mechanisms.

### 4.3. Phase Modification

Phase modification occupies a very important position among various modified strategies, which can be realized by forming

single crystallines, amorphous structure, or tuning the metal/phosphorus stoichiometric ratios. The common characteristic of phase modification is focusing on regulating the intrinsic properties of TMPs themselves to achieve promoted electrocatalytic activities. Regarding their contributions to the electrocatalysis, single-crystalline TMPs are helpful to investigate the electrocatalytic reaction mechanism and amorphous TMPs is thought to be more efficient because of containing more unsaturated active sites while tuning metal/phosphorus stoichiometric ratios is conducive to understanding the nature of active sites.

#### 4.3.1. Single Crystallines

Well-defined single crystallines are usually served as the model to study the electrochemical reactions.<sup>[119]</sup> Because of having a preferential growth of crystallographic orientation, single crystallines become ideal platforms to interrogate the electrocatalytic reaction mechanisms in the combination of theory and experiment.<sup>[120]</sup> However, the synthesis of TMPs single crystallines is a challenging work and corresponding breakthroughs may lead to finding a new catalyst system. In this regard, a representative case is the first identification of Ni<sub>2</sub>P as the efficient HER electrocatalyst. In 2005, Liu et al. theoretically predicted the Ni<sub>2</sub>P (001) facet could effectively facilitate HER.<sup>[27a]</sup> Afterward, Popczun et al. fabricated the Ni<sub>2</sub>P nanoparticles with a high density of exposed (001) facet (Figure 7a), and experimentally verified its superb HER activity.<sup>[27b]</sup> These pioneering works

render TMPs to be a hotspot in energy-related electrocatalysis. Successively, Zhang and co-workers prepared the ultrathin CoP nanosheets with dominant reactive facets via a chemical transformation strategy.<sup>[121]</sup> From the fast Fourier transform (FFT) pattern (Figure 7b inset), a porous CoP nanosheet was in a single crystalline form with a preferential [100] orientation. When used as acidic HER electrocatalyst, this CoP nanosheets presented excellent activity with requiring 56 mV overpotential to achieve a current density of 10 mA cm<sup>-2</sup> and a Tafel slope of 44 mV dec<sup>-1</sup>, much better than that of polycrystalline CoP nanoparticles. DFT calculation uncovered that on CoP (100) facet (one typical plane of {200} facets), a near-zero  $\Delta G_H^*$  at high hydrogen coverage ( $\theta_H^*$ ) could result in high utilization efficiency of active sites, thereby rendering CoP (100) highly active. In contrast, Yang and co-workers fabricated the ternary (Fe<sub>x</sub>Ni<sub>1-x</sub>)<sub>2</sub>P nanosheets with preferentially exposed {011̄} facets by the hydrothermal method followed by a phosphidation process.<sup>[122]</sup> From the HRTEM image (Figure 7c), two sets of lattice fringes with the same spacing of 0.220 nm corresponded to {112̄1} and {1̄211} planes of hexagonal (Fe<sub>x</sub>Ni<sub>1-x</sub>)<sub>2</sub>P, respectively. The FFT pattern (inset in Figure 7c) disclosed the single crystalline form of the (Fe<sub>0.048</sub>Ni<sub>0.952</sub>)<sub>2</sub>P nanosheets with a preferential {011̄} orientation. Accordingly, this (Fe<sub>0.048</sub>Ni<sub>0.952</sub>)<sub>2</sub>P nanosheets presented excellent activities in electrocatalytic HER over a wide pH range. Besides HER, CoP single-crystalline was also utilized in electrocatalytic OER but its advantage in single crystalline form was unknown.<sup>[123]</sup> More recently, Schmidt and co-workers uncovered the crystal facets-dependent HER activities on CoPS

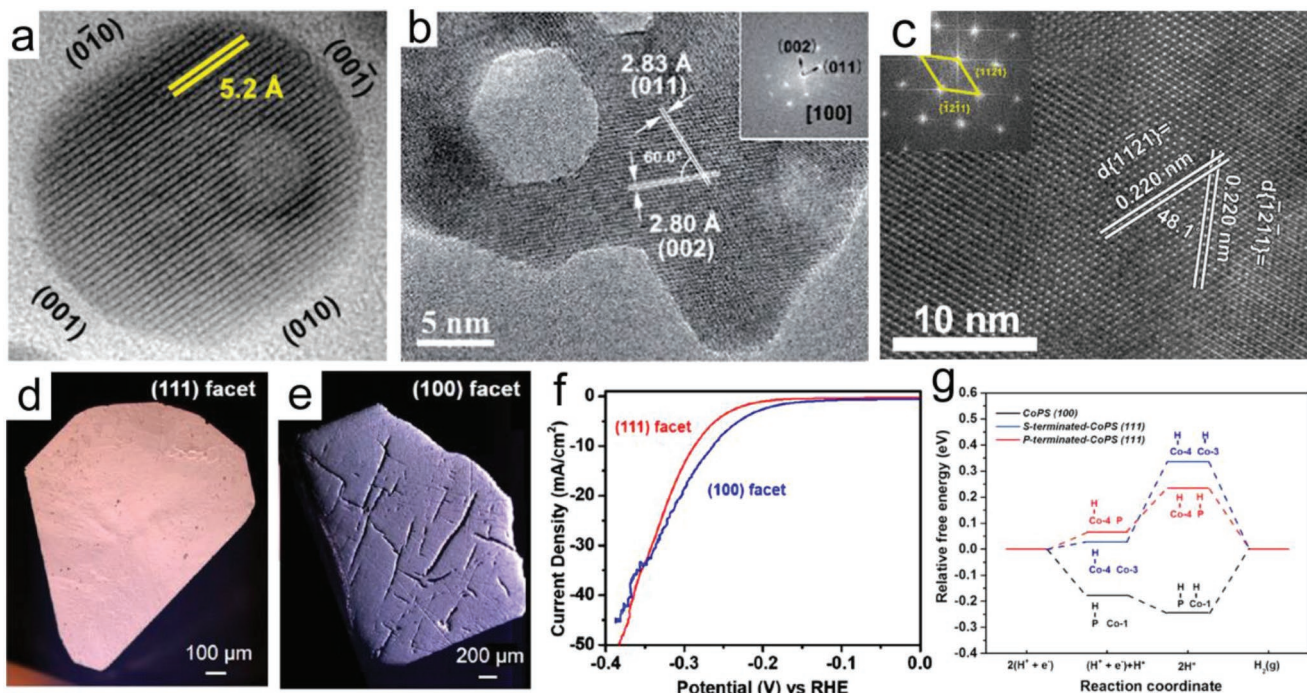


**Figure 7.** a) The HRTEM image of Ni<sub>2</sub>P nanoparticle with highly exposed Ni<sub>2</sub>P (001) facet. Reproduced with permission.<sup>[27b]</sup> Copyright 2013, American Chemical Society. b) The HRTEM image of ultrathin porous CoP nanosheets and its associated FFT pattern image (inset Figure 7b). Reproduced with permission.<sup>[121]</sup> Copyright 2017, Royal Society of Chemistry. c) The HRTEM image of (Fe<sub>0.048</sub>Ni<sub>0.952</sub>)<sub>2</sub>P nanosheets and the corresponding FFT pattern image (inset Figure 7c). Reproduced with permission.<sup>[122]</sup> Copyright 2019, Elsevier. The optical images of CoPS single crystals with exposed d) (111) facet and e) (100) facet. f) Comparison of HER performance on CoPS's (111) and (100) facets. g) Free energies of HER pathways on the CoPS (100) and CoPS (111). Reproduced with permission.<sup>[124]</sup> Copyright 2018, American Chemical Society.

single crystals by combining experiments with the theoretical calculation.<sup>[124]</sup> As depicted in optical images (Figure 7d,e), the (111) facet on CoPS single crystals was very smooth, while the surface of the (100) facet was rough with several small scratches. When employed as electrocatalysts for HER, these two crystalline facets displayed different HER activities as a function of overpotential (Figure 7f). In detail, (100) facet-CoPS displayed better activity than that of (111) facet-CoPS when the overpotential was below 0.35 V, while this situation was reversed at high overpotential region (>0.35 V). Accordingly, theoretical calculation indicated that this phenomenon resulted from the changes of rate-limiting step at different overpotential region (Figure 7g). At low overpotentials, the H atom adsorption (Volmer step) was the rate-limiting step, rendering the (100) facet with more favorable kinetics. Under large overpotential (>0.35 V), the H<sub>2</sub> recombination/desorption would dominate the HER process. Since the (111) facet had lower desorption barriers, it presented a higher performance in contrast with the (100) facet in this region. This work offers a valuable benchmark to investigate the facet dependence of HER activity on TMPs. We note here that more attention should be paid to this challenging but essential part with the aim of making better TMPs electrocatalysts.

#### 4.3.2. Amorphous Structure

From the catalytic point of view, amorphous catalysts are promising due to their greater flexibility in structure and composition. More importantly, their disordered domains contain lots of defects and vacancies, which are considered as the electrocatalytic active sites.<sup>[125]</sup> In fact, amorphous structures are often sensitive to synthesis conditions. Early studies have manifested that amorphous TMPs-alloys film fabricated by electrodeposition presented high activities towards HER.<sup>[126]</sup> With the development of synthetic strategies, some amorphous TMPs nanocatalysts appeared. For instance, Schaak and co-workers prepared the amorphous MoP nanoparticles with a diameter of  $\approx$ 4 nm through the solution-phase method, followed by thermal treatment to remove the organic ligands.<sup>[127]</sup> They found that annealing temperatures affected the MoP nanoparticles' crystallinity and size. After calcining at a temperature of 450 °C, MoP nanoparticles still remained amorphous features, which could be identified from the selected area electron diffraction (SAED) plot (Figure 8a). Regarding the electrocatalytic HER activity, MoP nanoparticles supported on the Ti electrode needed an overpotential of 90 mV to afford a current density of 10 mA cm<sup>-2</sup> in 0.5 M H<sub>2</sub>SO<sub>4</sub>. Successively, they synthesized 3 nm amorphous WP nanoparticles and displayed their high performance in electrocatalytic HER.<sup>[128]</sup> Besides, Xiong and co-workers reported the fabrication of the bulk amorphous NiFeP material via melting spinning and the rapid quenching process.<sup>[129]</sup> They found that the content of P in this alloy affected the phase structure. As displayed in Figure 8b, Ni<sub>40</sub>Fe<sub>40</sub>P<sub>20</sub> (NFP40) possessed a metallic appearance and its amorphous nature was confirmed by the HRTEM and corresponding SAED pattern. It was worth noting that the surficial oxide layer with a thickness of 5–7 nm is observed. Furthermore, synchrotron radiation-based X-ray absorption fine structure (XAFS) spectroscopy was used to unveil the local structural information. As depicted in Figure 8c,d, there were two bonding

types in NFP40, including the metal–metal bonds (Ni–Ni, Fe–Fe) and metal–phosphorus bonds (Ni–P, Fe–P). The metallic bonds expedited the electron transfer, while the phosphides provided moderate bonds with reaction intermediates. Meanwhile, the coordination numbers of Ni and Fe in NFP40 were greatly lower than those counterparts, manifesting metal atoms in the NFP40 were unsaturated. Integrated these typical merits together, this NFP40 electrode presented an excellent performance in OER with needing 219 mV overpotential to afford a current density of 10 mA cm<sup>-2</sup> and a small Tafel slope of 32 mV dec<sup>-1</sup> in 1 M NaOH, better than that of noble RuO<sub>2</sub> (Figure 8e). Interestingly, this NFP40 electrode could also facilitate the OER in acidic solution with requiring 540 mV overpotential to deliver a current density of 10 mA cm<sup>-2</sup> as well as the sustainable lifespan of 30 h (Figure 8f). Despite promoted electrocatalytic behavior observed on amorphous TMPs, identifying practical active sites in amorphous structure is still a very challenging work. It is anticipated that the development of *in situ* characterization techniques and precise computational modeling would contribute significantly to understand these fundamental properties.

#### 4.3.3. Metal/Phosphorus Stoichiometric Ratios

Since the first try of nanostructured metal phosphides in electrocatalysis, strenuous efforts have been dedicated to the pursuit of optimal metal/phosphorus stoichiometric ratios. As described before, different metal/phosphorus stoichiometric ratios result in obvious structural variations in the crystal structure, thus directly influencing the electrocatalytic performance.<sup>[22]</sup> Therefore, studying the effects of stoichiometric ratios on electrocatalytic activity is helpful to guide the design of catalysts by identifying the key intrinsic parameters that affect the electrocatalytic activities. Accordingly, herein, we profile recent advances in this field, and some typical works are selected to manifest how the stoichiometric ratios impact the catalytic activities.

In this regard, the primary question is that for metal-rich or phosphorus-rich TMPs, which one is better for electrocatalysis. This issue is commonly required to be discussed in a specific electrocatalytic reaction. For example, for HER, a general viewpoint at the early stage is believed that phosphorus-rich TMPs present better performance than the metal-rich one. This standpoint could be found in the Schaak group's work, in which they compared the HER activities on the morphologically equivalent Co<sub>2</sub>P and CoP nanocrystals.<sup>[130]</sup> As demonstrated in Figure 9a, Co<sub>2</sub>P (left) adopted the Co<sub>2</sub>Si structure type, while CoP (right) crystallized in the MnP structure type. The major difference between them was that the low-index surfaces of Co<sub>2</sub>P had a much larger proportion of exposed Co atoms than that of CoP. Regarding the electrocatalytic HER activity, Co<sub>2</sub>P required an overpotential of 95 mV to deliver a current density of 10 mA cm<sup>-2</sup> in 0.5 M H<sub>2</sub>SO<sub>4</sub>, which was inferior to that of CoP (75 mV@10 mA cm<sup>-2</sup>) (Figure 9b). This work illustrated that lower Co/P stoichiometric ratios led to promoted HER activity, mainly aroused from that the higher proportion of Co–P bonds in CoP might offer more active sites. Likewise, Liu and co-workers utilized a similar solution-based method to prepare the monodispersed nickel phosphide nanocrystals, including Ni<sub>5</sub>P<sub>4</sub>, Ni<sub>2</sub>P, and Ni<sub>12</sub>P<sub>5</sub>.<sup>[131]</sup> When these nanocrystals were evaluated

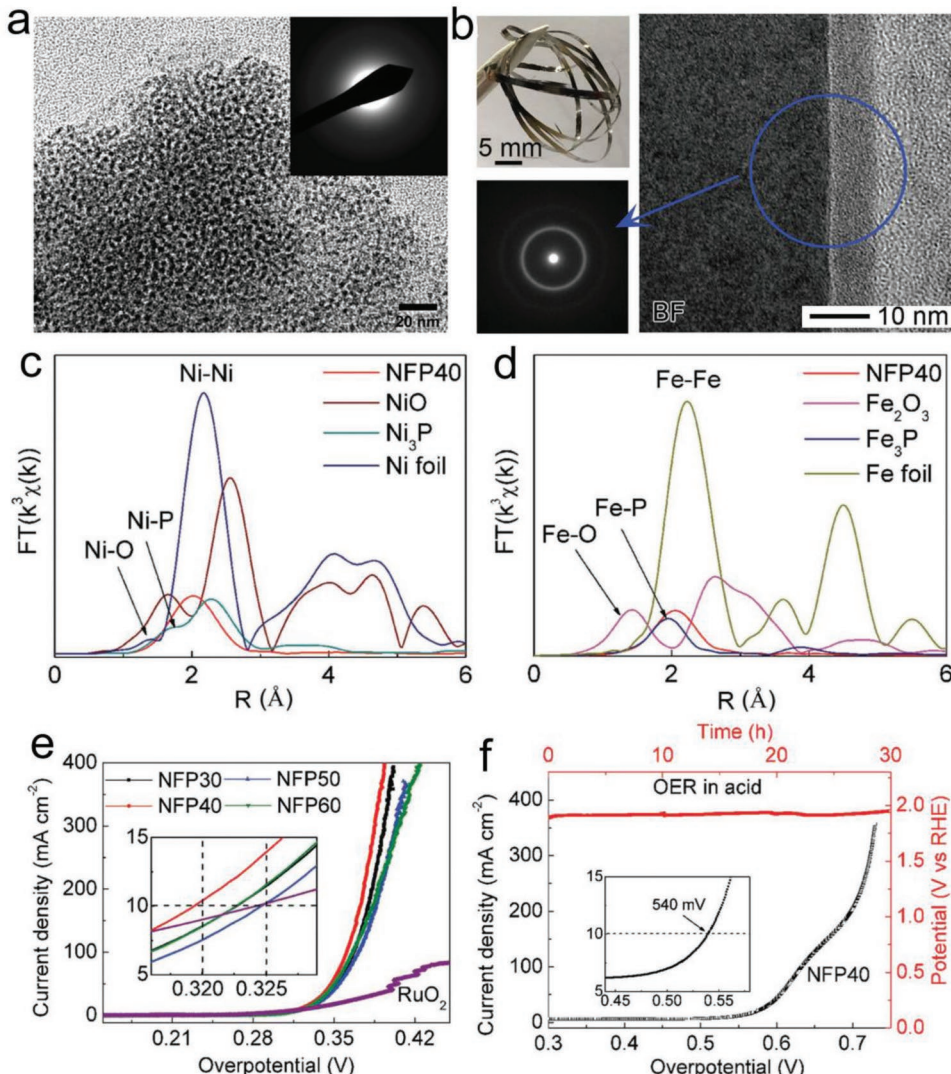


**Figure 8.** a) The TEM image of amorphous MoP and its inserted SAED pattern. Reproduced with permission.<sup>[127]</sup> Copyright 2014, American Chemical Society. b) The optical graph, HRTEM image, and SAED pattern of  $\text{Ni}_{40}\text{Fe}_{40}\text{P}_{20}$  (NFP40). The EXAFS spectra of c) Ni K-edge and d) Fe K-edge in NFP40 and contrast samples. e) OER performance of  $\text{RuO}_2$  and  $\text{NiFeP}_x$  ( $x$  means various Ni/Fe ratios) samples in 1 M NaOH. f) The polarization curve and durability test of NFP40 in acidic medium. Reproduced with permission.<sup>[129]</sup> Copyright 2017, John Wiley and Sons.

as HER catalysts, the electrocatalytic activity followed this order:  $\text{Ni}_5\text{P}_4 > \text{Ni}_2\text{P} > \text{Ni}_{12}\text{P}_5$ . With higher positive charged Ni and a stronger ensemble effect of P, phosphorus-rich  $\text{Ni}_3\text{P}_4$  achieved better performance. Besides, Wang and co-workers observed a similar activity trend in molybdenum-based phosphides.<sup>[132]</sup> As demonstrated in Figure 9c, to deliver a current density of 10 mA cm<sup>-2</sup>, metal-rich  $\text{Mo}_3\text{P}$  required an overpotential of  $\approx 500$  mV, while it decreased to  $\approx 140$  mV on MoP. According to an elaborate theoretical calculation, they drew a conclusion that the P atoms served as active sites for HER, which could bond proton at a low H coverage and desorb  $\text{H}_2$  at high H coverage. Apart from HER, a similar activity trend for TMPs can be also observed on electrocatalytic ORR. In this respect, an impressive work has been done by Geyer's group, in which they synthesized the highly monodisperse CoP and  $\text{Co}_2\text{P}$  nanocrystals and compared their electrocatalytic ORR performance.<sup>[133]</sup>

In Figure 9d, CoP displayed excellent activity with a half-wave potential of 0.858 V (closer to Pt/C), which was superior to that of metal-rich  $\text{Co}_2\text{P}$  ( $E_{1/2} = 0.839$  V). In order to find the reasons for the discrepancy in ORR activity, they further performed the DFT calculation to compare the reaction barriers. As displayed in Figure 9e,f, under an electrode potential of 1.23 V, the energies for the first three steps were nearly downhill, while the final  $\text{OH}^*$  desorption step ( $\text{OH}^* + 3\text{OH}^- + e^- \rightarrow 4\text{OH}^-$ ) was obviously endothermic, becoming the rate-determining step for ORR on both CoP (211) and  $\text{Co}_2\text{P}$  (211). Typically, in this step, the value of adsorption free energy on CoP (2.40 eV) was lower than that on  $\text{Co}_2\text{P}$  (4.23 eV), thus rendering CoP with higher ORR activity. As for the reason why high phosphorus content was in favor of facilitating the  $\text{OH}^*$  desorption step, they deduced that high electronegativity P atoms could attract electrons from Co atoms and thereby the binding strength between

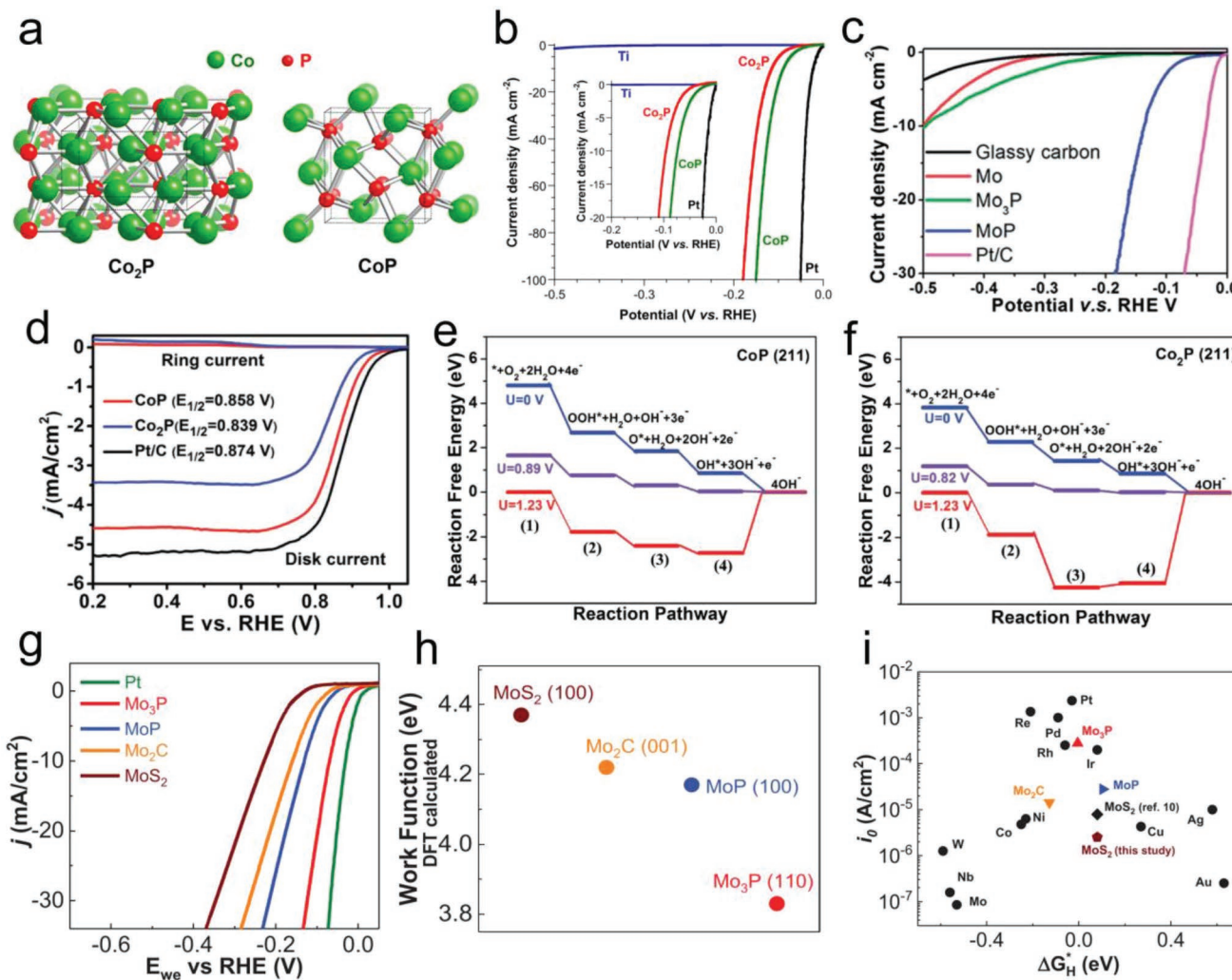


**Figure 9.** a) Crystalline structures of  $\text{Co}_2\text{Si}$ -type  $\text{Co}_2\text{P}$  (left) and  $\text{MnP}$ -type  $\text{CoP}$  (right). b) Polarization curves of  $\text{Co}_2\text{P}/\text{Ti}$ ,  $\text{CoP}/\text{Ti}$  electrodes, bare  $\text{Ti}$  foil, and  $\text{Pt}$  mesh in  $0.5 \text{ M H}_2\text{SO}_4$ . Reproduced with permission.<sup>[130]</sup> Copyright 2015, American Chemical Society. c) Polarization curves of  $\text{Mo}_3\text{P}$ ,  $\text{MoP}$ ,  $\text{Mo}$ , and contrastive samples in  $0.5 \text{ M H}_2\text{SO}_4$ . Reproduced with permission.<sup>[132]</sup> Copyright 2014, Royal Society of Chemistry. d) ORR performance of  $\text{Co}_2\text{P}$ ,  $\text{CoP}$ , and  $\text{Pt/C}$  with a rotating speed of 1600 rpm in  $\text{O}_2$ -saturated  $0.1 \text{ M KOH}$  solution. Free energy diagram at different potentials for ORR on surfaces of e)  $\text{CoP}$  (211) surface and f)  $\text{Co}_2\text{P}$  (211). Reproduced with permission.<sup>[133]</sup> Copyright 2018, John Wiley and Sons. g) Polarization curves for  $\text{Pt}$ ,  $\text{Mo}_3\text{P}$ ,  $\text{MoP}$ ,  $\text{Mo}_2\text{C}$ , and  $\text{MoS}_2$  samples. h) Comparison of absolute work functions on  $\text{Mo}_3\text{P}$  (110) plane and contrastive catalysts. i) HER volcano plot obtained from plotting exchange current density concerning Gibbs free energy of adsorbed hydrogen on various samples. Reproduced with permission.<sup>[134]</sup> Copyright 2019, John Wiley and Sons.

the adsorbed  $\text{OH}^*$  and the surface  $\text{Co}$  atoms was weakened. From the above works, it can be seen that  $\text{P}$  atoms in TMPs play a crucial role in electrocatalysis.

Nevertheless, when we jump to the conclusion that lower  $\text{M}/\text{P}$  stoichiometric ratios in TMPs are better for HER, this issue becomes controversial again. More recently, Asadi and co-workers reported that tri-molybdenum phosphide ( $\text{Mo}_3\text{P}$ ) nanoparticles presented a better HER activity than that of phosphorus-rich  $\text{MoP}$  from practical experiment and theoretical calculation.<sup>[134]</sup> Typically,  $\text{Mo}_3\text{P}$  adopted the tetragonal structure with each  $\text{Mo}$  atom is coordinated by either two or four  $\text{P}$  atoms, while  $\text{MoP}$  crystallized in hexagonal structure with  $\text{Mo}$  six-coordinated by  $\text{P}$  atoms. Caused by variation in structure, in Figure 9g,  $\text{Mo}_3\text{P}$  nanoflakes displayed remarkable electrocatalytic HER behavior with requiring 69 mV overpotential to

support a current density of  $10 \text{ mA cm}^{-2}$ , superior to that of  $\text{MoP}$  counterpart ( $130 \text{ mV}@10 \text{ mA cm}^{-2}$ ). Subsequently, DFT calculation was performed to explain the difference in HER activity. As shown in Figure 9h,  $\text{Mo}_3\text{P}$  had a lower work function ( $3.83 \text{ eV}$ ) as compared to  $\text{MoP}$  ( $4.17 \text{ eV}$ ), indicating that the  $\text{Mo}$ -states were possibly responsible for the charge transfer. Meanwhile, the computational simulation of HER process revealed that hydrogen tends to be stable at the bridging sites of  $\text{Mo}$  instead of  $\text{P}$  sites, thus engendering an ideal hydrogen adsorption Gibbs-free energy on  $\text{Mo}_3\text{P}$  (110) surface (Figure 9i). Besides, Schipper et al. also observed a similar phenomenon in various stoichiometric ratios Fe-based phosphides thin films.<sup>[135]</sup> In their work, the HER activities followed the trend  $\text{Fe}_3\text{P} > \text{Fe}_2\text{P} > \text{FeP}$  because metal-rich phosphides ( $\text{Fe}_3\text{P}$  and  $\text{Fe}_2\text{P}$ ) surface had higher hydrogen coverages under thermoneutral

hydrogen absorption conditions. Till now, it is still an open question to distinguish which stoichiometric ratio in TMPs is optimized for electrocatalysis. But it is expected that ongoing efforts in this area will contribute to an in-depth understanding of the nature of active sites in TMPs.

#### 4.4. Structural Engineering

There is a general point that the electrode structure is of significance to achieve considerable catalytic performance. On the one hand, electrode structures dominate the number of available active sites. On the other hand, they can affect mass transport, concentration gradient, and stability. Recent advances in the structural design of electrocatalysts are ranging from the dimensional control, porous structure to novel substrates. Regarding the dimensional control, nanostructured TMPs with 0D, 1D, 2D, 3D morphologies have been reported everywhere and their contribution to electrocatalysis was well discussed in recent works.<sup>[18c,136]</sup> Hence, herein, we mainly focus on the latter two cases and found out why these modifications are useful for electrocatalysis.

##### 4.4.1. Porous Structure

Porous materials have extensive applications in various domains, such as industrial catalysis, biomedicine, solar cells, material filtration, and electrode materials.<sup>[137]</sup> In electrocatalysis, constructing the porous structure is in favor of exposing abundant active sites, facilitating electrolyte infiltration and

accelerating gas release.<sup>[138]</sup> Taken these typical merits into account, continuous efforts have been dedicated to the controllable synthesis of porous TMPs for electrocatalysis. In this part, some porous TMPs are selected with focusing on the evolution process of pore structure and the influence of pore structure on catalytic performance.

Sacrificial template method has been widely used to construct various porous micro-nanostructures.<sup>[139]</sup> In general, the formation of the porous structure is caused by some components in precursors being selectively removed away. For example, Wang's group fabricated porous CoPO nanosheets by using the zeolitic imidazolate framework-67 (ZIF-67) nanosheets as the self-template, followed by oxidation and phosphidation processes.<sup>[140]</sup> It was worth noting that the generation of the porous structure occurred on the oxidation step, in which carbon component in the ZIF-67 precursor was volatilized. As displayed in Figure 10a, it could be seen that numerous pores with a diameter of 20–40 nm were well distributed throughout the nanosheets. Benefited from the porous structure and O doping, this porous CoPO nanosheets demonstrated excellent activities in both electrocatalytic HER and OER. In comparison, Cheng and co-workers fabricated porous and multishelled Ni<sub>2</sub>P hollow microspheres by using the carbon sphere as the self-template, followed by a two-step thermal treatment.<sup>[141]</sup> Regarding the formation of this unique structure, it was caused by the decomposition of carbon during the oxidation process. As displayed in Figure 10b, this sample was assembled by smaller Ni<sub>2</sub>P nanoparticles simultaneously leaving numerous voids on the surface with a size of 2 to 25 nm in diameter. Such a unique structure imparted it with abundant active sites and short charge transport

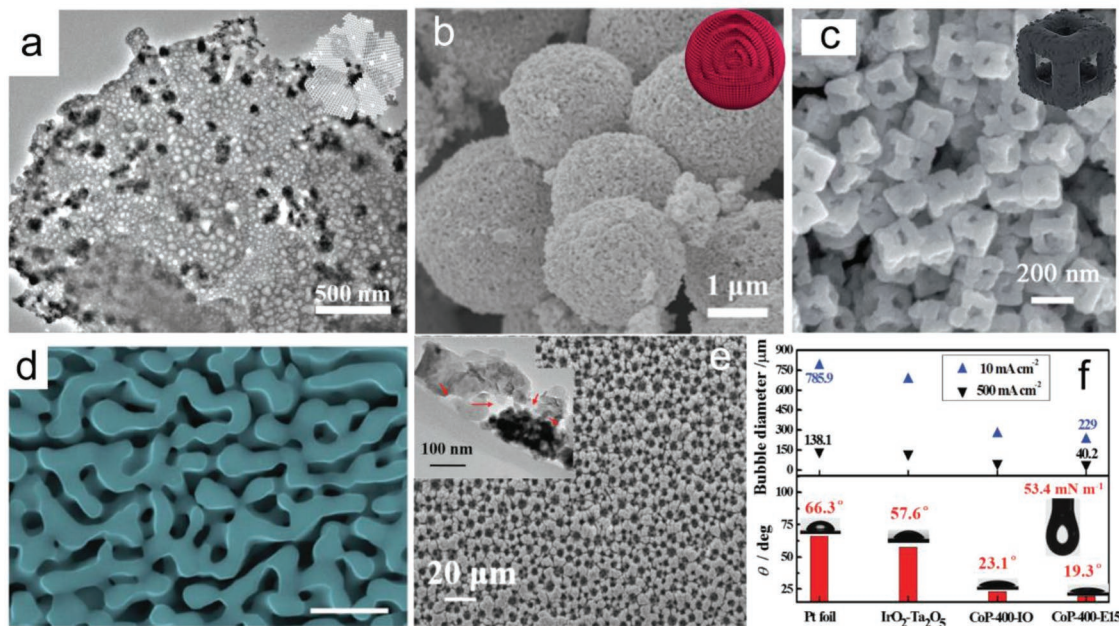


**Figure 10.** a) TEM image of the 2D porous CoPO nanosheets. Reproduced with permission.<sup>[140]</sup> Copyright 2018, John Wiley and Sons. b) SEM image of the multishelled Ni<sub>2</sub>P hollow microspheres. Reproduced with permission.<sup>[141]</sup> Copyright 2017, American Chemical Society. c) SEM image of Co<sub>0.6</sub>Fe<sub>0.4</sub>P nanoframes. Reproduced with permission.<sup>[142]</sup> Copyright 2019, Royal Society of Chemistry. d) SEM image of nanoporous Co<sub>2</sub>P with a cooling rate of 3 krpm, scale bar: 500 nm. Reproduced with permission.<sup>[145]</sup> Copyright 2016, John Wiley and Sons. e) SEM image of Co<sub>2</sub>P film with micro-nanoscale pores. f) The measurements of contact angle and surface tension around the gas-liquid interface on various samples. Reproduced with permission.<sup>[146]</sup> Copyright 2018, John Wiley and Sons.

distances. As expected, in 1 M KOH, this multishelled Ni<sub>2</sub>P only needed 98 and 270 mV overpotentials to deliver a current density of 10 mA cm<sup>-2</sup> for HER and OER, respectively, which were better than that of solid-interior Ni<sub>2</sub>P microspheres and Ni<sub>2</sub>P nanoparticles. Successively, Peng's group prepared 3D carved open Co<sub>0.6</sub>Fe<sub>0.4</sub>P framework by using bimetallic Co–Fe Prussian blue analogues (Co–Fe PBAs) as the template, followed by etching and phosphidation processes.<sup>[142]</sup> This distinctive structure was formed during the selective etching step, in which Co/Fe ions at the face center was removed by the etchant, while the edges and corners of Co–Fe PBAs were well retained. As depicted in Figure 10c, the morphology of Co<sub>0.6</sub>Fe<sub>0.4</sub>P was open 3D frameworks, which could offer magnified specific surface area, facile electrolyte infiltration and gas evolution for electrocatalysis. Thereby, Co<sub>0.6</sub>Fe<sub>0.4</sub>P nanoframes presented better performance in both HER and OER as compared with that of Co<sub>0.6</sub>Fe<sub>0.4</sub>P nanocubes. Similar work could be found in hierarchical porous CoP/C nanoboxes, which used phytic acid as the etchant.<sup>[143]</sup>

As a typical selective dissolving process, dealloying is a robust way to generate a nanoporous structure with tunable pore sizes and porosities.<sup>[144]</sup> In this regard, Chen's group fabricated the bicontinuous nanoporous cobalt phosphide (np-Co<sub>2</sub>P) by single-roller melt spinning and dealloying methods.<sup>[145]</sup> Since the melt-spun ribbon precursors contained two crystalline phases (Co and Co<sub>2</sub>P), during the dealloying process the cobalt phase was selectively leached with the formation of bicontinuous nanoporous structure. As shown in Figure 10d, the isotropic nanopores were homogeneously distributed throughout the entire sample. As expected, this 3D nanoporous Co<sub>2</sub>P with pores size around 30 nm presented excellent HER performance in both acidic and alkaline media. In comparison, Jiao's group reported the synthesis of micro-nanoporous Co<sub>2</sub>P film by an integrated strategy (Figure 10e).<sup>[146]</sup> In detail, self-supported CoP film with micrometer-scale pores was first prepared by electrodeposition using hydrogen bubbles as the template. Then, after being sintered in the reducing atmosphere, CoP film was transformed into dual-phase Co<sub>2</sub>P–Co film (CoP-400). Finally, the micro-nanoporous Co<sub>2</sub>P film was formed by etching Co phase in acidic solution. Profited from this hierarchical porous structure, this Co<sub>2</sub>P film (CoP-400-E15) required 86 and 376 mV overpotentials to afford current densities of 10 and 150 mA cm<sup>-2</sup>, respectively, superior to that of CoP film and Co<sub>2</sub>P–Co film. Interestingly, this CoP-400-E15 film had both the smallest contact angles and bubble break-off diameter among these samples, manifesting rapid bubble release and electrolyte penetration on its hierarchical porous structure (Figure 10f). Based on the above discussions, it is believed that porous structure engineering will still be a promising methodology for constructing robust TMPs electrocatalysts.

#### 4.4.2. Novel Substrate

Substrates play an important role in electrocatalysis because they cannot only serve as the support for loading catalysts but also are responsible for electron transfer from the external circuit to catalysts. Regarding the selection criteria of a substrate, suitable substrates should have excellent conductivity, high mechanical

strength, corrosion resistance, and negligible activities. Taken the above considerations into account, we select some examples to summarize recent developments of novel substrates in electrocatalysis. As a kind of novel 2D material, black phosphorus (BP) has high charge-carrier mobility, tunable bandgap, and highly anisotropic characters.<sup>[147]</sup> Considering these merits of BP, Yan's group anchored Ni<sub>2</sub>P nanoparticles on few-layer BP nanosheets by a three-step method.<sup>[148]</sup> As demonstrated in Figure 11a, first, bulk BP crystals were prepared by vapor deposition, followed by a liquid exfoliation process to generate few-layer BP nanosheets. Finally, Ni<sub>2</sub>P@BP heterostructure was obtained through the solvothermal process. When utilized as HER electrocatalysts in 0.5 M H<sub>2</sub>SO<sub>4</sub>, this Ni<sub>2</sub>P@BP displayed remarkable performance with needing 107 mV overpotential to afford a current density of 10 mA cm<sup>-2</sup>, which was better than that of pure Ni<sub>2</sub>P (311 mV@10 mA cm<sup>-2</sup>) and pure BP (600 mV@10 mA cm<sup>-2</sup>). In comparison, Yu's group prepared the in-plane BP/Co<sub>2</sub>P heterostructures and demonstrated their electrocatalytic application in HER.<sup>[149]</sup> After liquid exfoliation, the edges of BP became more reactive because there were many defects and unsaturated P atoms, thus triggering the selectively grown of Co<sub>2</sub>P nanocrystals on the BP edges (inserted diagram in Figure 11b). As depicted in Figure 11b, the BP/Co<sub>2</sub>P heterostructure had uniform lamellar morphology with a border thickness of 15 nm. With the improved electrical conductivity, BP/Co<sub>2</sub>P hybrids displayed remarkable HER performance in both acidic and alkaline electrolyte (Figure 11c).

As another promising 2D material, ternary metal carbides (MXenes) possess the merits of good mechanical stability, great hydrophilicity, and conductivity, which enable it to be a suitable substrate.<sup>[150]</sup> For example, Qiu's group fabricated the MXene–CoP hybrid by a multistep method.<sup>[151]</sup> The shining point in this work was that the 2D MXenes could be transformed into hierarchical 3D architecture by a capillary-forced assembling strategy. Benefited from this, the 3D MXene matrix not only provided a highly conductive framework but also prevented the aggregation of active sites, thus boosting the catalytic performance. As shown in Figure 11d, this CoP@3D Ti<sub>3</sub>C<sub>2</sub>–MXene hybrids presented considerable HER performance with needing 168 mV overpotential to deliver a current density of 10 mA cm<sup>-2</sup>, outperforming that of pure CoP and CoP@Ti<sub>3</sub>C<sub>2</sub>–MXene (2D). Meanwhile, CoP@3D Ti<sub>3</sub>C<sub>2</sub>–MXene also demonstrated the best OER performance among these samples (Figure 11e).

Besides, the self-supported electrode is quite appealing because of simplifying the electrode preparation process, avoiding the side effect of insulting binder and bringing about sustainable stability.<sup>[152]</sup> In most cases, this self-supported substrate is selected to fabricate the TMPs nanoarrays.<sup>[136a]</sup> For example, Yuan's group prepared mesoporous CoP nanorod arrays (CoP-MNA) on Ni foam through an electrodeposition method.<sup>[153]</sup> It could be seen that the 3D Ni foam skeleton contained macroporous canals was beneficial for electrolyte penetration and gas evolution (Figure 11f). Profited from these typical merits, CoP-MNA required overpotentials of 121 and 235 mV to reach current densities of 100 and 800 mA cm<sup>-2</sup> for HER, respectively, better than that of noble metals. Obviously, the self-supported electrode will be the preferred matrix to support catalysts in order to achieve relatively high current densities and meet the demand for large-scale commercial production.

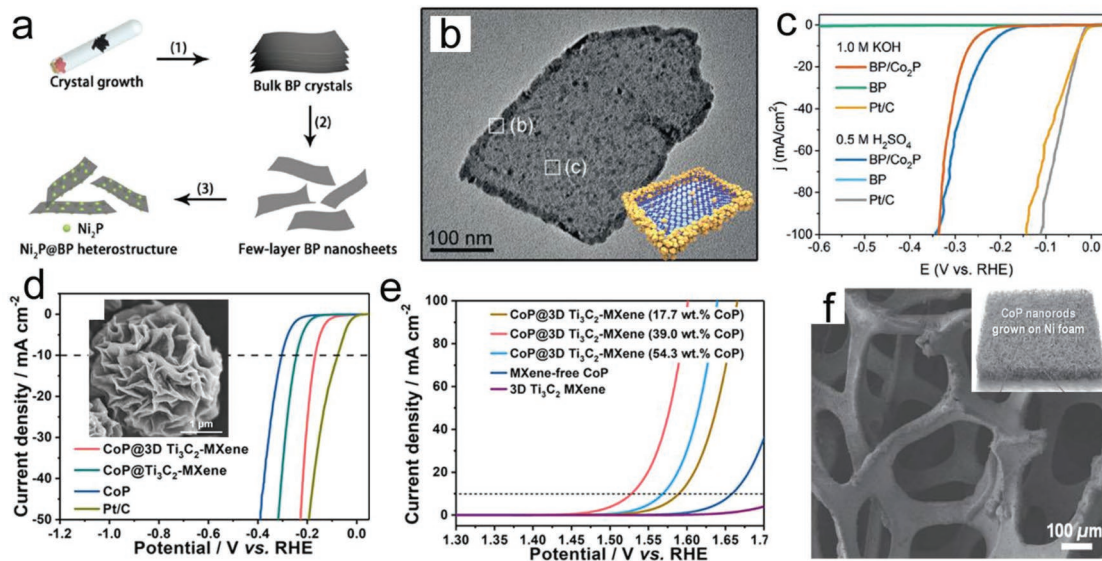


**Figure 11.** a) Schematic illustration of the synthetic methods of  $\text{Ni}_2\text{P}$ @BP heterostructure. Reproduced with permission.<sup>[148]</sup> Copyright 2017, John Wiley and Sons. b) the TEM image of BP/Co<sub>2</sub>P nanosheets. c) Polarization curves of Pt/C, BP, BP/Co<sub>2</sub>P in acidic and alkaline media. Reproduced with permission.<sup>[149]</sup> Copyright 2018, John Wiley and Sons. d) Polarization curves of CoP@3D Ti<sub>3</sub>C<sub>2</sub>-MXene and contrast catalysts for HER (inserted: morphology of CoP@3D Ti<sub>3</sub>C<sub>2</sub>-MXene). e) Polarization curves of CoP@3D Ti<sub>3</sub>C<sub>2</sub>-MXene and contrast catalysts for OER. Reproduced with permission.<sup>[151]</sup> Copyright 2018, American Chemical Society. f) SEM image of CoP nanorod arrays on nickel foam and its inserted optical image. Reproduced with permission.<sup>[153]</sup> Copyright 2015, John Wiley and Sons.

#### 4.5. Nanocarbon Incorporation

At the early stage, nanocarbons (CNTs or graphene) are usually chosen as substrates to support TMPs catalysts.<sup>[55,154]</sup> Regarding their functions, these nanocarbon matrixes can facilitate the electron transfer across the carbon network and provide large specific surface areas for exposing more catalytic active sites. With an in-depth study in this area, it is found that coupling nanocarbon with TMPs can engender multiple effects on electrocatalysis. It is a general point that nanoscale catalysts have high surface energy and are prone to be aggregated in either the fabrication process or electrochemical test, thus decreasing the number of active sites.<sup>[5b,155]</sup> While the existence of nanocarbon can restrict the aggregation of nanoparticles by confining the nanoparticles into the carbon matrix.<sup>[156]</sup> In this respect, one representative work has been made by Li and co-workers. They developed a MOF-assisted strategy to embed MoP nanoparticles into porous carbon (MoP@PC).<sup>[157]</sup> As depicted in Figure 12a, MoP nanoparticles were homogeneously distributed in a regular octahedral porous carbon matrix. The existence of nanocarbon could not only protect the catalysts from aggregation but also be served as the conductive framework for electron transfer. Thus, MoP@PC exhibited excellent HER activities with needing a 153 mV overpotential to deliver a current density of  $10 \text{ mA cm}^{-2}$  and a Tafel slope of  $66 \text{ mV dec}^{-1}$ . In comparison, our group reported the fabrication of Co/CoP@nitrogen carbon nanofibers via a controllable electrospinning method and subsequent thermal treatments.<sup>[158]</sup> As shown in Figure 12b, Co/CoP@NC presented continuous nanofiber morphology with a diameter of  $\approx 260 \text{ nm}$ . When evaluated as the HER catalyst, Co/CoP@NC displayed robust HER activity in both acidic and alkaline media. The existence of the

carbon matrix could not only confine the Co/CoP nanoparticles without aggregation but also form the interlaced 3D conductive network for boosting the electron transfer.

Stability is also a crucial criterion to evaluate catalysts' performance. While the surficial oxidation occurred on TMPs usually renders the decay of HER performance. Considering this issue, Sung's group prepared carbon-shell coated FeP nanoparticles (FeP/C) by a scalable method.<sup>[159]</sup> As depicted in Figure 12c, FeP with carbon shell revealed no apparent activity decay after 5000 CV cycles, while the performance of pure FeP decreased significantly with increasing cycles. Further analysis indicated that FeP with the carbon layer could prevent the formation of iron oxides on the surface, thus enabling its outstanding stability. Besides the protecting effect, more recent studies manifested the existence of electron interaction between nanocarbon and TMPs. For example, Feng's group prepared MoP nanoparticles enveloped in Mo- and P-doped carbon (MoP@C) and uncovered the electron localization effect caused by the carbon layer.<sup>[160]</sup> Abundant Mo-C and P-C bonds at interfaces could reshape the Fermi level and delocalize the accumulated electrons, thus accelerating its alkaline HER kinetics. As illustrated in Figure 12d inset, Mo-C and P-C bonds facilitated the electron transfer and promoted water dissociation into H, making subsequent H adsorption and desorption processes easily proceeded. Regarding the performance, MoP@C catalyst demonstrated an overpotential of 49 mV to deliver a current density of  $10 \text{ mA cm}^{-2}$ , much lowered than that of pure MoP (154 mV). Likewise, the electron interaction between nanocarbon and TMPs was also observed by Song and co-workers.<sup>[161]</sup> They synthesized the defective carbon-coated CoP nanoparticles (CoP-DC) by the phosphidation of the Co<sup>2+</sup>-contained polymer hydrogel. The theoretical calculation and experiment revealed that the strong interfacial

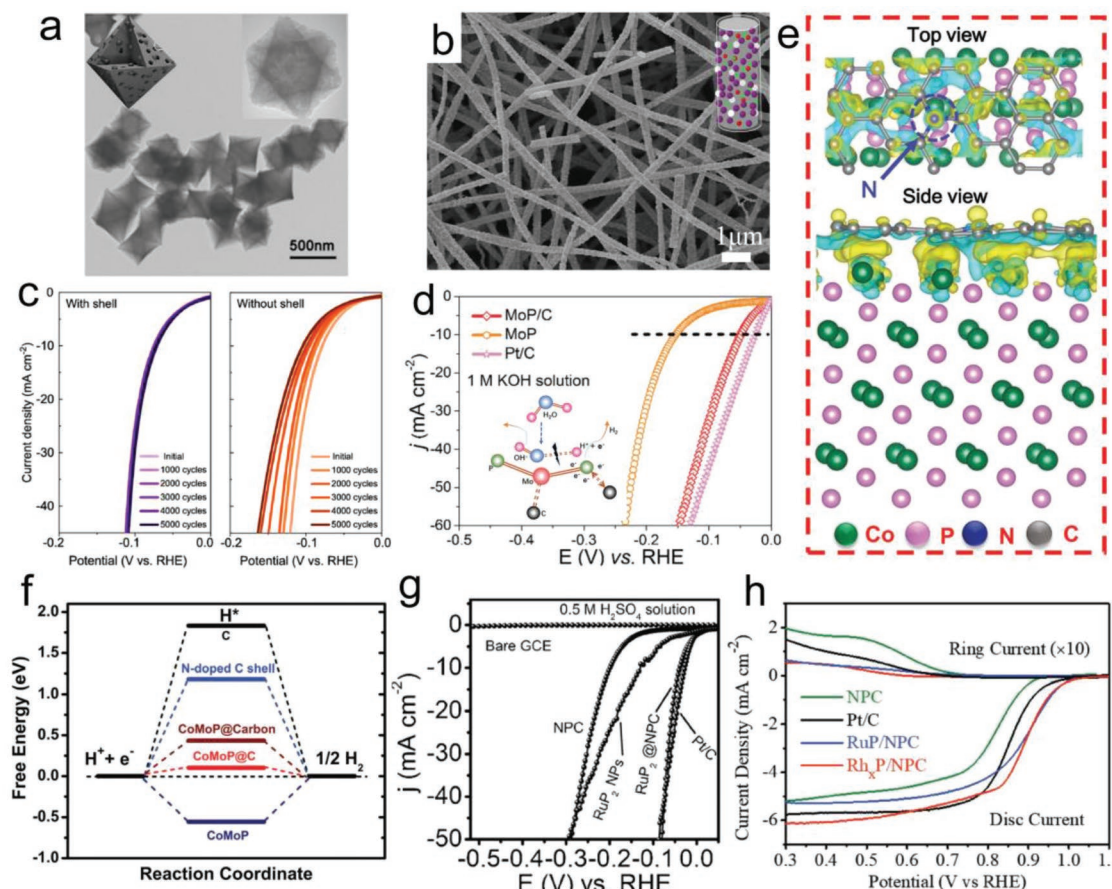


**Figure 12.** a) SEM image of MoP@porous carbon composite. Reproduced with permission.<sup>[157]</sup> Copyright 2016, John Wiley and Sons. b) SEM image of Co/CoP@nitrogen-doped carbon nanofibers. Reproduced with permission.<sup>[158]</sup> Copyright 2018, Elsevier. c) Long-term stability test of FeP/C and pure FeP electrocatalysts. Reproduced with permission.<sup>[159]</sup> Copyright 2017, American Chemical Society. d) HER performance of 20% Pt/C catalysts, MoP, and MoP@C samples in alkaline media. (Inserted diagram: possible HER mechanism on MoP/C). Reproduced with permission.<sup>[160]</sup> Copyright 2018, John Wiley and Sons. e) The charge density of electrons distributed between CoP and N-doped carbon. Reproduced with permission.<sup>[161]</sup> Copyright 2018, John Wiley and Sons. f) The calculated free energy diagram of the HER on various catalysts. Reproduced with permission.<sup>[162]</sup> Copyright 2017, Royal Society of Chemistry. g) HER performance of RuP<sub>2</sub>@NPC and contrast samples in acidic media. Reproduced with permission.<sup>[164]</sup> Copyright 2017, John Wiley and Sons. h) ORR performance of Rh<sub>x</sub>P/NPC, RuP/NPC, and contrastive catalysts. Reproduced with permission.<sup>[166]</sup> Copyright 2018, John Wiley and Sons.

polarization between CoP and DC triggered the charge redistribution. As demonstrated in the differential charge density plot (Figure 12e), the DC surface was served as the electron-rich surface, which can make the ORR process facilely proceeded. While positively charged CoP surface promoted the formation of CoOOH (real active sites) for OER. Benefitted from the interfacial polarization effect, CoP-DC displayed superior ORR and OER performance.

Besides, it is reported that this kind of interaction can be strengthened by coupling TMPs with heteroatom-doped carbon. For instance, Li's group utilized a one-step pyrolysis method to fabricate the CoMoP@C nanocatalyst, in which the ultrasmall CoMoP nanoparticles were embedded in few-layer N-doped carbon shell.<sup>[162]</sup> When evaluated as the acidic HER catalyst, this CoMoP@C exhibited remarkable performance with requiring a low overpotential of 41 mV to deliver a current density of 10 mA cm<sup>-2</sup> as well as a small Tafel slope of 49.73 mV dec<sup>-1</sup>, which was better than that of pure CoMoP nanoparticles and N-doped carbon. As displayed in Figure 12f,

compared to the CoMoP@carbon (without N dopants), the  $\Delta G_{H^*}$  on CoMoP@C was much more moderate (close to zero). It manifested that N dopants could boost the interfacial electronic interaction between carbon and TMPs, thus improving the electrocatalytic performance. As a rising star, noble TMPs also spurred great interests to be promising alternatives to pure noble metals for electrocatalysis.<sup>[163]</sup> In general, these reported noble TMPs are required to be coupled with heteroatom-doped carbon with the aim of achieving optimal electrocatalytic performance. For example, Mu and co-workers synthesized the RuP<sub>2</sub> nanoparticles enveloped in N,P-codoped carbon (RuP<sub>2</sub>@NPC) through the pyrolysis of phytic acid (PA) cross-linked ruthe-nium complexes and melamine.<sup>[164]</sup> Their motivation was derived from the DFT calculation, in which the result indicated that pure RuP<sub>2</sub> had an unfavorable  $\Delta G_{H^*}$  value of 0.627 eV. While once RuP<sub>2</sub> was coupled with N, P dual-doped carbon, the corresponding  $\Delta G_{H^*}$  on RuP<sub>2</sub>@NPC was optimized. As expected, RuP<sub>2</sub>@NPC exhibited Pt-like HER performance in 0.5 M H<sub>2</sub>SO<sub>4</sub> with needing 38 mV overpotential at a current

density of  $10 \text{ mA cm}^{-2}$ , which was much better than that of NPC ( $199 \text{ mV}@10 \text{ mA cm}^{-2}$ ), RuP<sub>2</sub> NPs ( $129 \text{ mV}@10 \text{ mA cm}^{-2}$ ) (Figure 12g). What is more, this RuP<sub>2</sub>@NPC also demonstrated Pt-like HER activity in both neutral and alkaline media. Besides, similar work can be found in OsP<sub>2</sub> nanoparticles@N, P-doped carbon and IrP<sub>2</sub>@N-doped carbon,<sup>[165]</sup> which can be served as robust electrocatalysts for HER. There is no doubt that the emergence of noble TMPs@heteroatom-doped carbon pushes HER performance on TMPs to a new level. Besides, this noble TMPs@heteroatom-doped carbon can also be used in electrocatalytic ORR. In this respect, Cho's group fabricated the RuP and Rh<sub>x</sub>P nanoparticles decorated on N, P dual-doped carbon by a simple pyrolysis method.<sup>[166]</sup> Typically, both Rh<sub>x</sub>P/NPC and RuP/NPC with low loadings of Rh and Ru ( $\approx 0.4 \text{ wt\%}$  of Rh,  $\approx 0.5 \text{ wt\%}$  of Ru) displayed remarkable ORR performance, further illustrating promising prospects of this kind of material (Figure 12h). Based on the above discussions, the nanocarbon cannot only protect the catalyst from agglomeration and oxidation but also engender strong interfacial interaction with TMPs, thus achieving greatly promoted activity and stability. The corresponding performance of reported TMP-based electrocatalysts in this chapter is listed in Table 1.

## 5. Applications

As mentioned before, these modulated strategies regulate the structure and composition of TMPs at the molecular/atom scale and indeed promote their corresponding electrocatalytic performance. For instance, the strategies of elemental doping, structural engineering, and nanocarbon incorporation can not only regulate the intrinsic catalytic active sites but also promote the gas/electrolyte transport and electron transfer. Inspired by these, TMPs are highlighted in the multifunctional electrocatalysis applications. Firstly, by dint of their high activity and stability in HER, OER, and ORR, TMPs are widely used in sustainable energy conversion devices, such as water electrolyzer, rechargeable metal–air batteries, etc. Subsequently, recent studies indicated that TMPs exhibit electrocatalytic effects in Li–S batteries. In common, the natural surface oxidation of TMPs brings about the detrimental effect on electrocatalysis HER.<sup>[25b]</sup> While in Li–S batteries, the surface oxidation layer on TMPs can lead to the activation of the surface metal sites for confining polysulfides via strong metal–sulfur bond, making TMPs as desirable sulfur host materials. Finally, some novel applications, such as carbon dioxide reduction, and electrocatalysis of organic molecules are proposed despite their potential catalytic mechanism being ambiguous.

### 5.1. Overall Water Splitting

Producing H<sub>2</sub> fuel by electrochemical water splitting is environmentally benign and regarded as an ideal way to replace current petrochemical processes.<sup>[167]</sup> As displayed in Figure 13a, the overall water splitting consists of the anodic oxygen evolution and cathodic hydrogen evolution reaction, which can occur under different pH-gradient electrolytes. Considering the high-performance of TMPs in both HER and OER, it is natural to

employ them as bifunctional overall water splitting electrode.<sup>[168]</sup> Generally speaking, those reported bifunctional water electrolysis applications of TMPs are in neutral or basic medium.<sup>[3a]</sup> For example, Wu et al. prepared the ternary Ni<sub>0.1</sub>Co<sub>0.9</sub>P porous nanosheets on conductive carbon fiber paper and tried them as the bifunctional electrode for overall water splitting in neutral-pH condition.<sup>[169]</sup> To reach a current density of  $10 \text{ mA cm}^{-2}$ , the required cell voltages with Ni<sub>0.1</sub>Co<sub>0.9</sub>P catalyst was 1.89 V, which was lower than that of noble Pt/C//Ir/C couples (Figure 13b). The enhanced electrocatalytic performance was derived from the cation doping, in which the incorporation of Ni induced a slight compression of CoP's lattice, thus regulating the surface electronic structure (Figure 13c). Compared with neutral water electrolysis, TMPs present a better performance in the alkaline water electrocatalysis. For instance, our group fabricated the core-branch CoP@NiFe–OH nanohybrids via a facile three-step method.<sup>[170]</sup> As shown in Figure 13d, these hybrids were homogeneously dispersed on the substrate. The outer NiFe–OH nanoplates were vertically grafted onto the inner CoP nanowires with forming a clear interface (Figure 13e). Benefitted from strong synergy effect between crystalline CoP nanowires and the amorphous NiFe–OH nanoplates, this bifunctional CoP@NiFe–OH electrode presented remarkable activity in alkaline water electrolysis with needing cell voltages of 1.53, 1.63, and 1.68 V to deliver current densities of 10, 50, 100  $\text{mA cm}^{-2}$ , respectively, which was better than that of noble (+)IrO<sub>2</sub>/C//Pt/C(–) counterpart (Figure 13f). It was worth noting that this bifunctional CoP@NiFe–OH electrode simultaneously demonstrates excellent stability (Figure 13g).

### 5.2. Metal–Air Batteries

The rechargeable metal–air batteries hold great promise to be the next-generation energy storage devices owing to their high power and energy density.<sup>[171]</sup> Among them, the zinc–air batteries (ZABs) can achieve a high theoretical specific energy density of  $1086 \text{ Wh kg}^{-1}$ , nearly five times higher than that of commercial LIBs.<sup>[172]</sup> Meanwhile, the low cost and environmental benignity of zinc render it to be a desired candidate for future utilization. Unfortunately, the main challenge in air cathodes lies in the high overpotential caused by sluggish OER/ORR kinetics.<sup>[173]</sup> In view of this issue, it is feasible to utilize the above-mentioned strategies to engineer TMPs electrocatalysts with needed characteristics. For instance, Wang et al. fabricated the Cu<sub>3</sub>P nanoparticles enveloped in N,P-codoped porous carbon matrix (Cu<sub>3</sub>P@NPPC) using N, P containing Cu-based MOF as the precursor, followed by carbonization and phosphidation.<sup>[174]</sup> When utilized as the air cathode in the homemade ZABs, it could achieve an open-circuit voltage of 1.46 V, the maximum power density of  $110.8 \text{ mW cm}^{-2}$  at  $192 \text{ mA cm}^{-2}$  as well as long-term cycle life of 38 h at  $5 \text{ mA cm}^{-2}$  (Figure 14a–e). The excellent performance resulted from the synergy between the Cu<sub>3</sub>P species and the heteroatom-doped carbon, the hierarchical porous structure promoting fast mass-transport pathways and the protective effect of outer carbon shell. Aside from the ZABs, TMPs have also been used as the cathode electrocatalysts in high energy density Li–O<sub>2</sub> and Na–O<sub>2</sub> batteries and present comparable catalytic performance.<sup>[175]</sup>

**Table 1.** Comparison of performance for selected TMPs with various modulated strategies.

Strategies	Catalysts <sup>[Ref.]</sup>	Electrolyte/reactions	$\eta$ [mV]@i [mA cm <sup>-2</sup> ]	Tafel slope [mV dec <sup>-1</sup> ]	Stability (i or $\eta$ )@times
Elemental doping	Zn <sub>0.08</sub> Co <sub>0.92</sub> P <sup>[83]</sup>	0.5 M H <sub>2</sub> SO <sub>4</sub> /HER	39@10	39	100 mA cm <sup>-2</sup> @22 h
	Ni@Ni <sub>2</sub> P–Ru <sup>[89]</sup>	0.5 M H <sub>2</sub> SO <sub>4</sub> /HER	51@10	35	5000 cycles
	Mo–CoP <sup>[90]</sup>	1 M KOH/OER	305@10	56	1.57 V@20 h <sup>b)</sup>
	NiCoP <sup>[91]</sup>	1 M KOH/OER	220@10	79.5	1.46 V@36 h <sup>b)</sup>
	FeCoNiP <sup>[92]</sup>	1 M KOH/OER	270@100	60	10 mA cm <sup>-2</sup> @24 h
	Pyrite-type CoPS <sup>[94]</sup>	0.5 M H <sub>2</sub> SO <sub>4</sub> /HER	48@10	48	10 mA cm <sup>-2</sup> @36 h
	CoS P <sup>[95]</sup>	0.5 M H <sub>2</sub> SO <sub>4</sub> /HER	109@100	55	95 mV@24 h <sup>b)</sup>
	o-CoSe <sub>2</sub>  P <sup>[96]</sup>	1 M KOH/HER	104@10	69	250 mV@20 h
	S:Co <sub>2</sub> P <sup>[97]</sup>	1 M KOH/OER	360@100	71	340 mV@20 h
	O-doped MoP@RGO <sup>[46a]</sup>	1 M KOH/HER	93@20	58	5000 cycles
	NiFeSP <sup>[98]</sup>	1 M KOH/HER	91@10	82.6	10 mA cm <sup>-2</sup> @25 h
	CoFePO <sup>[99]</sup>	1 M KOH/OER	274.5@10	51.7	=50 mA cm <sup>-2</sup> @100 h
Interfacial engineering	O-Ni <sub>(1-x)</sub> Fe <sub>x</sub> P <sub>2</sub> <sup>[100]</sup>	1 M KOH/OER	155@10	55	1.43 V@24 h <sup>b)</sup>
	Co <sub>1-x</sub> Ni <sub>x</sub> (S <sub>1-y</sub> P <sub>y</sub> ) <sub>2</sub> <sup>[101]</sup>	1 M KOH/OER	285@10	105	20 mA cm <sup>-2</sup> @100 h
	Ni <sub>2</sub> P–NiP <sub>2</sub> <sup>[104]</sup>	1 M KOH/HER	59.7@10	58.8	85 mV@24 h <sup>b)</sup>
	Co/CoP <sup>[108]</sup>	1 M KOH/OER	340@10	79.5	20 mA cm <sup>-2</sup> @12 h
	Fe@FeP <sup>[109]</sup>	0.5 M H <sub>2</sub> SO <sub>4</sub> /HER	110@100	55	10 000 cycles
	PANI/CoP <sup>[110]</sup>	0.5 M H <sub>2</sub> SO <sub>4</sub> /HER	–	34.5	=100 mA cm <sup>-2</sup> @30 h
	EG-Pt/CoP <sup>[111]</sup>	0.5 M H <sub>2</sub> SO <sub>4</sub> /HER	21@10	42.5	65 mA cm <sup>-2</sup> @100 h
	CoO <sub>x</sub> /CoP <sup>[114]</sup>	1 M KOH/HER	146@100	42.8	150 mV@35 h
	Ni <sub>5</sub> P <sub>4</sub> @NiCo <sub>2</sub> O <sub>4</sub> <sup>[115]</sup>	1 M KOH/HER	27@10	27	20 mA cm <sup>-2</sup> @45 h
	Co <sub>2</sub> P–Ni <sub>2</sub> P/TiO <sub>2</sub> <sup>[116]</sup>	1 M KOH/HER	92@10	49	92 mV@20 h
	sc-Ni <sub>2</sub> P <sup>δ</sup> /NiHO <sup>[117]</sup>	1 M KOH/HER	60@10	75	10 mA cm <sup>-2</sup> @100 h
Phase modification	Ni <sub>2</sub> P <sup>[27b]</sup>	0.5 M H <sub>2</sub> SO <sub>4</sub> /HER	130@20	46	500 cycles
	CoP <sup>[121]</sup>	0.5 M H <sub>2</sub> SO <sub>4</sub> /HER	131@100	44	10 mA cm <sup>-2</sup> @24 h
	(Fe <sub>x</sub> Ni <sub>1-x</sub> ) <sub>2</sub> P <sup>[122]</sup>	1 M PBS/HER	90@10	82.7	100 mA cm <sup>-2</sup> @20 h
	CoPS (111) <sup>[124]</sup>	0.5 M H <sub>2</sub> SO <sub>4</sub> /HER	–	86	–
	Amorphous MoP <sup>[127]</sup>	0.5 M H <sub>2</sub> SO <sub>4</sub> /HER	90@10	45	20 mA cm <sup>-2</sup> @18 h
	Amorphous NiFeP <sup>[129]</sup>	1 M NaOH/OER	219@10	32	10 mA cm <sup>-2</sup> @12 h
	Co <sub>2</sub> P <sup>[130]</sup>	0.5 M H <sub>2</sub> SO <sub>4</sub> /HER	95@10	45	20 mA cm <sup>-2</sup> @24 h
	CoP <sup>[130]</sup>	0.5 M H <sub>2</sub> SO <sub>4</sub> /HER	75@10	50	20 mA cm <sup>-2</sup> @24 h
	MoP <sup>[132]</sup>	0.5 M H <sub>2</sub> SO <sub>4</sub> /HER	180@30	54	140 mV@40 h
	CoP <sup>[133]</sup>	0.1 M KOH/ORR	0.858 V <sup>a)</sup>	–	0.7 V@30 h <sup>b)</sup>
	Co <sub>2</sub> P <sup>[133]</sup>	0.1 M KOH/ORR	0.839 V <sup>a)</sup>	–	0.7 V@30 h <sup>b)</sup>
	Mo <sub>3</sub> P <sup>[134]</sup>	0.5 M H <sub>2</sub> SO <sub>4</sub> /HER	69@10	38	200 mV@40 h
Structural engineering	MoP <sup>[134]</sup>	0.5 M H <sub>2</sub> SO <sub>4</sub> /HER	130@10	44	–
	CoPO <sup>[140]</sup>	1 M KOH/OER	280@10	59	10 mA cm <sup>-2</sup> @10 h
	Ni <sub>2</sub> P <sup>[141]</sup>	1 M KOH/HER	98@10	86.4	1000 cycles
	Co <sub>0.6</sub> Fe <sub>0.4</sub> P <sup>[142]</sup>	1 M KOH/HER	133@10	61	/
	np-Co <sub>2</sub> P <sup>[145]</sup>	1 M KOH/HER	60@10	40	100 mV@50 000 s
	Co <sub>2</sub> P film <sup>[146]</sup>	1 M KOH/HER	376@150	73	500 mA cm <sup>-2</sup> @90 h
	Ni <sub>2</sub> P@BP <sup>[148]</sup>	0.5 M H <sub>2</sub> SO <sub>4</sub> /HER	107@10	38.6	107 mV@24 h
Nanocarbon incorporation	BP/Co <sub>2</sub> P <sup>[149]</sup>	0.5 M H <sub>2</sub> SO <sub>4</sub> /HER	340@100	62	250 mV@24 h
	3D MXene-CoP <sup>[151]</sup>	1 M KOH/OER	298@10	51	10 mA cm <sup>-2</sup> @10 h
	CoP nanorods <sup>[153]</sup>	1 M KOH/HER	235@800	51	5000 cycles
	MoP@PC <sup>[157]</sup>	0.5 M H <sub>2</sub> SO <sub>4</sub> /HER	153@10	66	2000 cycles
	Co/CoP@NC <sup>[158]</sup>	1 M KOH/HER	180@10	60.3	10 000 cycles

**Table 1.** Continued.

Strategies	Catalysts <sup>[Ref.]</sup>	Electrolyte/reactions	$\eta$ [mV]@i [mA cm <sup>-2</sup> ]	Tafel slope [mV dec <sup>-1</sup> ]	Stability (i or $\eta$ )@times
	FeP/C <sup>[159]</sup>	0.5 M H <sub>2</sub> SO <sub>4</sub> /HER	71@10	/	10 000 cycles
	MoP@C <sup>[160]</sup>	1 M KOH/HER	49@10	54	72 mV@12 h
	CoP-DC <sup>[161]</sup>	0.1 M KOH/ORR	0.81 V <sup>a)</sup>	/	5000 cycles
	CoMoP@C <sup>[162]</sup>	0.5 M H <sub>2</sub> SO <sub>4</sub> /HER	41@10	49.73	120 mV@24 h
	RuP <sub>2</sub> @NPC <sup>[164]</sup>	0.5 M H <sub>2</sub> SO <sub>4</sub> /HER	38@10	38	10 mA cm <sup>-2</sup> @11 h
	RuP/NPC <sup>[166]</sup>	0.1 M KOH/ORR	0.89 V <sup>a)</sup>	/	0.7 V@80 000 s <sup>b)</sup>
	Rh <sub>x</sub> P/NPC <sup>[166]</sup>	0.1 M KOH/ORR	0.89 V <sup>a)</sup>	/	0.7 V@80 000 s <sup>b)</sup>

<sup>a)</sup>The half-wave potential for ORR; <sup>b)</sup>Voltage versus reversible hydrogen electrode, PBS: phosphate buffered saline (pH 7).

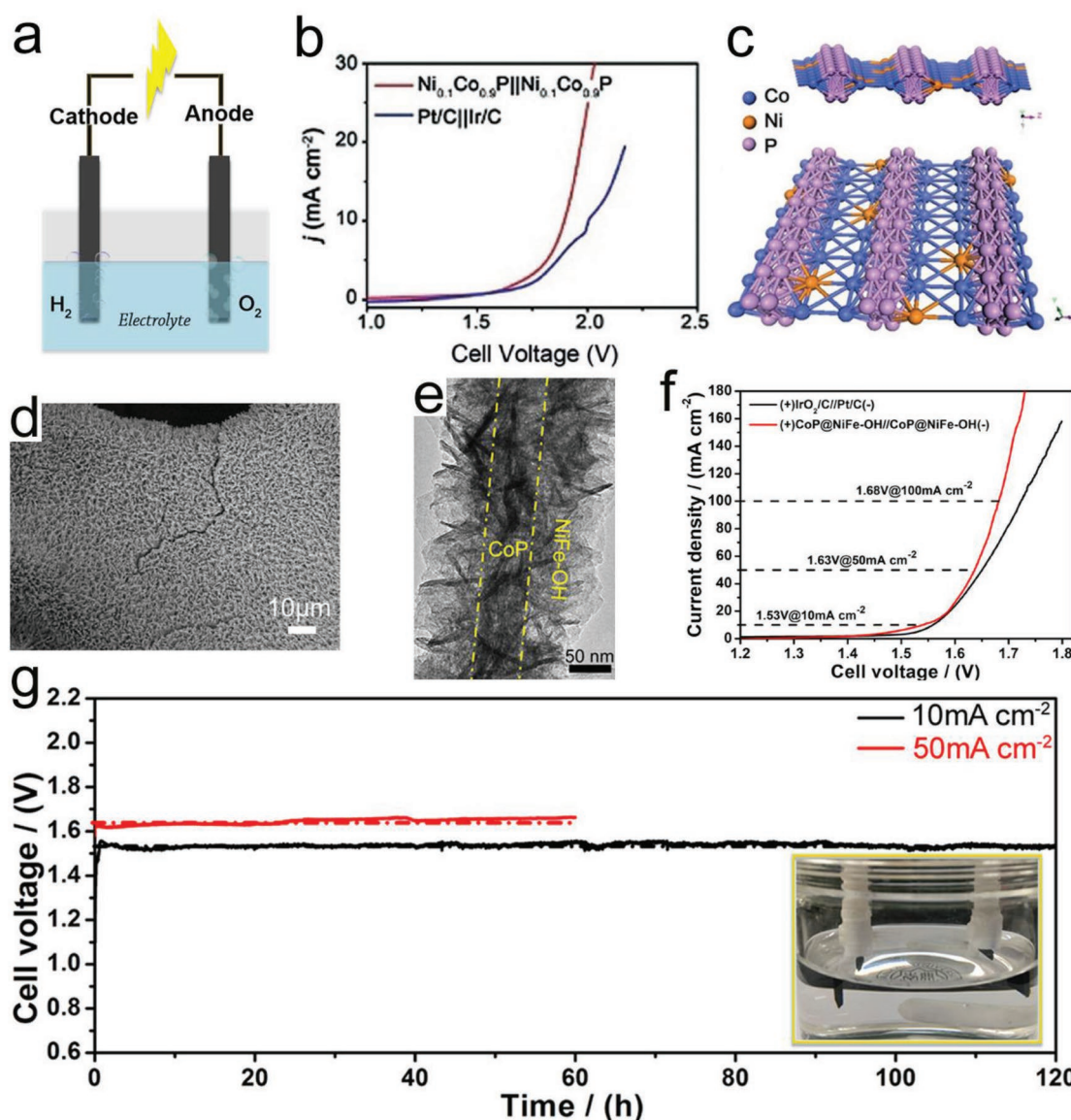


**Figure 13.** a) Schematic illustration of water electrolyzer. b) Polarization curves for overall water splitting consisting of  $\text{Ni}_{0.1}\text{Co}_{0.9}\text{P}||\text{Ni}_{0.1}\text{Co}_{0.9}\text{P}$  and commercial  $\text{Pt}/\text{C}||\text{Ir}/\text{C}$  catalysts in 1 M phosphate buffer solution. c) Crystal structure of  $\text{Ni}_{0.1}\text{Co}_{0.9}\text{P}$ . Reproduced with permission.<sup>[169]</sup> Copyright 2018, John Wiley and Sons. d) SEM image of  $\text{CoP}@\text{NiFe-OH}$  electrode. e) The TEM image of  $\text{CoP}@\text{NiFe-OH}$  electrode. f) Polarization curves of  $\text{CoP}@\text{NiFe-OH}$  electrode and  $(+)\text{IrO}_2/\text{C}/\text{Pt}/\text{C}(-)$  counterpart for overall water electrolysis in 1 M KOH. g) Stability test of bifunctional  $\text{CoP}@\text{NiFe-OH}$  electrode at different current density for overall water splitting. (Inset: a representative photograph of water electrolyzer). Reproduced with permission.<sup>[170]</sup> Copyright 2019, Elsevier.

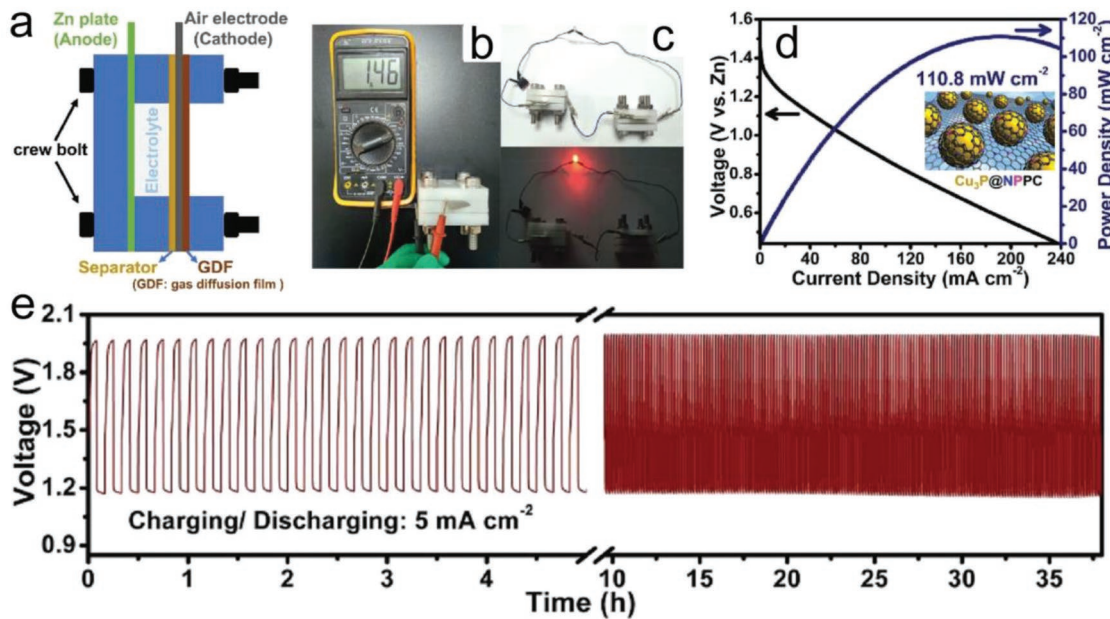


**Figure 14.** a) Graphical illustration of the homemade Zn–air battery. b) Image of the assembled Zn–air battery with an open-circuit voltage of 1.46 V. c) Red LED ( $\approx 2$  V) powered by two-series batteries. d) Polarization and the corresponding power density curves of the assembled battery. e) Long-term cycling tests of the Zn–air battery using  $\text{Cu}_3\text{P}@\text{NPPC}$ -650 as the air cathode at the charging and discharging current density of  $5 \text{ mA cm}^{-2}$ . Reproduced with permission.<sup>[174]</sup> Copyright 2018, John Wiley and Sons.

### 5.3. Li–S Batteries

Li–S batteries are considered as promising next-generation energy storage and conversion device due to its high energy density of  $2600 \text{ Wh kg}^{-1}$ , the low-cost and environmental benignity of S.<sup>[176]</sup> Unfortunately, they suffer from several intractable issues for practical utilization. Current major bottleneck lays in the shuttle effect of LPS intermediates, sluggish reaction kinetics, the poor electrical conductivity of the S and its discharge products ( $\text{Li}_2\text{S}/\text{Li}_2\text{S}_2$ ), resulting in inferior cyclic performance and large polarization.<sup>[72,177]</sup> Recently, micro-nanostructured carbon has been widely used as a host material to alleviate these issues.<sup>[75,178]</sup> But it is not effective to restrain the shuttle effect because of their weak adsorption of polysulfides.<sup>[76]</sup> Thus, polarized materials (metal oxides,<sup>[179]</sup> metal sulfides,<sup>[180]</sup> and metal hydroxides,<sup>[74]</sup> etc.) have been reported as the effective host materials to immobilize LPS via their strong chemical affinity. Nevertheless, the rate performance of these electrodes is unsatisfied because of their poor electrical conductivity.<sup>[181]</sup> In contrast, TMPs are regarded as the suitable sulfur cathodes to balance these two points. In 2017, Wang and co-workers experimentally revealed that the TMPs could potentially be served as the host materials with superior cyclic stability.<sup>[34]</sup> Successively, they further presented a molecular-level understanding of chemical interaction between TMPs and LPS.<sup>[78]</sup> The surficial oxidation could result in the formation of Co–O–P-like species on CoP surface. This rendered that surface Co sites could capture LPS species via strong Co–S bonding and yield Li–O–P moieties. While on the reduced CoP surface, due to the weak polarization of Co–P bonds, neither the Co nor the P sites could effectively bind LPS (Figure 15a). Therefore, as depicted in the CV curves (Figure 15b), the

oxidized CoP displayed much narrower current peaks and a smaller voltage hysteresis as compared with that of the CoP-R, indicating the faster electrochemical conversion of LPS on the oxidized CoP. The proposed lithium polysulfide-binding mechanism on the surface oxidation layer of TMPs may lay the foundation of rationally designing high performance TMPs cathode materials for Li–S batteries. In comparison, Qian and co-workers investigated the reaction kinetics of Li–S chemistry on different cobalt-based compounds ( $\text{Co}_3\text{O}_4$ ,  $\text{CoS}_2$ ,  $\text{Co}_4\text{N}$ , and CoP).<sup>[182]</sup> With the use of CoP as the sulfur scaffold, the best electrochemical performance was obtained. Its excellent performance stemmed from the moderate adsorption ability, rapid diffusion dynamics of LPS intermediates on CoP as well as its suitable p band positions. Besides, lowering the amount of electrolyte is beneficial for achieving high energy density at the cell level but in lean electrolyte the kinetics of the sulfur redox reactions are limited, resulting in the formation of “dead” sulfur on the electrode surface upon cycling. More recently, Wang and co-workers arrived at a new level by uncovering the electrocatalytic effects of MoP on sulfur redox reactions in the lean electrolyte.<sup>[183]</sup> Figure 15c presented charging/discharging voltage profiles of the CNT-S electrode and MoP-CNT-S electrode under a lean electrolyte/sulfur (E/S) ratio of  $6 \text{ mL}_\text{E mg}^{-1}\text{S}$ . Obviously, the improved specific capacity of  $863 \text{ mAh g}^{-1}$  at  $0.8 \text{ mA cm}^{-2}$  was achieved on MoP-CNT-S electrode because the MoP nanoparticles catalyzed the transformation of dissolved LPS into solid  $\text{Li}_2\text{S}/\text{Li}_2\text{S}_2$ , and more LPS tended to be electrochemically active on the MoP surface. In comparison, Tao and co-workers compared the adsorption energy and dissociated energy for  $\text{Li}_2\text{S}$  on different TMPs surfaces using theoretical calculations.<sup>[184]</sup> Figure 15d demonstrated the adsorption and decomposition mechanism on the

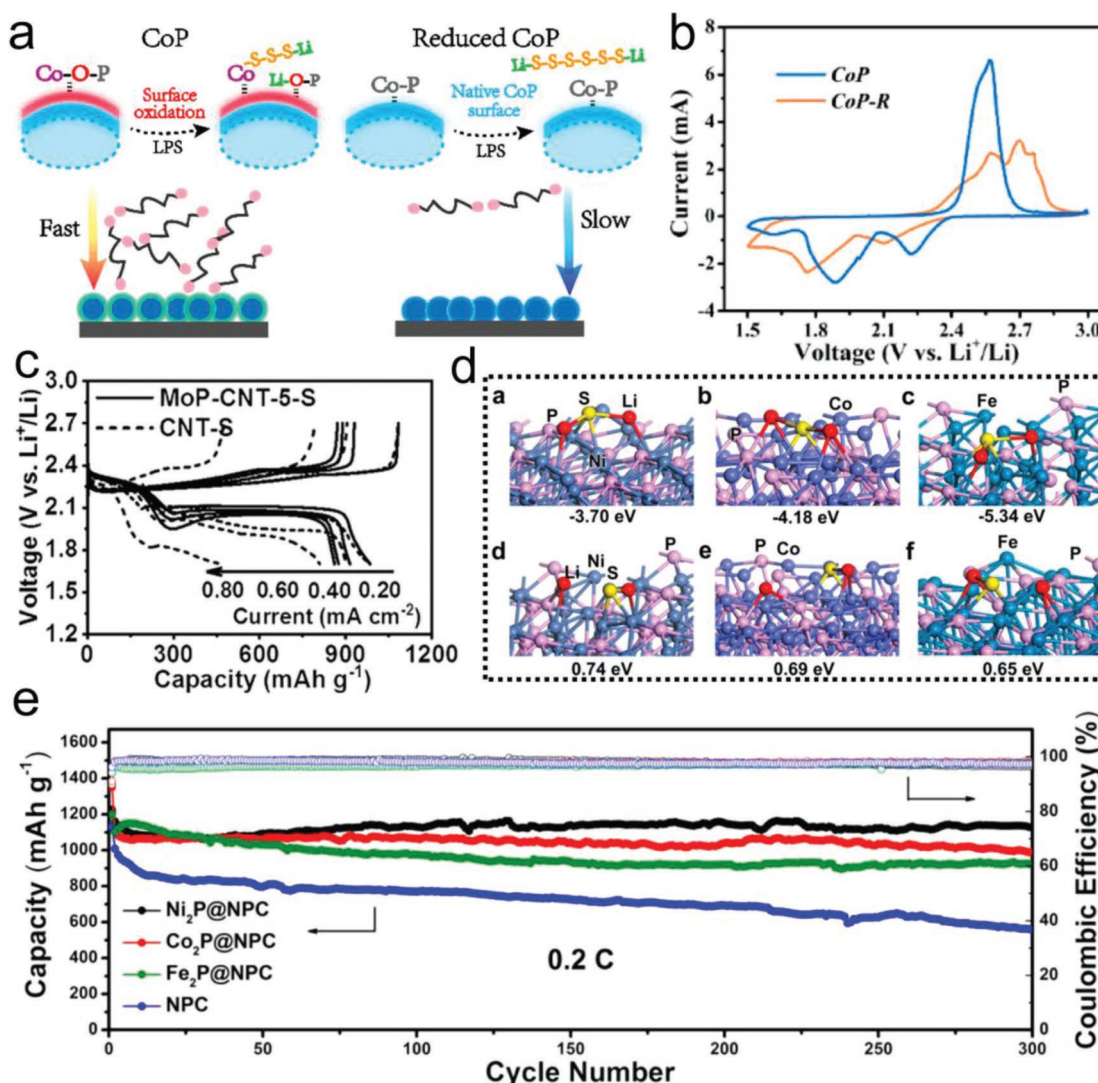


**Figure 15.** a) Schematic diagram of LPS adsorption and conversion processes on CoP surfaces versus reduced CoP surfaces. b) CV curves of S cathodes (measured against a Li metal anode) modified with CoP-CNT and CoP-R-CNT. Reproduced with permission.<sup>[78]</sup> Copyright 2018, American Chemical Society. c) Representative charging/discharging voltage profiles of the MoP-CNT-5-S and CNT-S electrodes at under lean electrolyte conditions ( $E/S = 6$ ; sulfur mass loading:  $\approx 4.0 \text{ mg cm}^{-2}$ ). Reproduced with permission.<sup>[183]</sup> Copyright 2018, John Wiley and Sons. d) Adsorption and decomposition mechanism on the surface of various TMPs. e) Cycling performance and corresponding coulombic efficiency of TMPs@NPC/S cathodes at 0.2 C. Reproduced with permission.<sup>[184]</sup> Copyright 2017, American Chemical Society.

surface of various TMPs. It could be seen that TMPs showed a strong affinity for trapping Li<sub>2</sub>S and boost the decomposition of Li<sub>2</sub>S. Accordingly, in coin-cell Li–S batteries, after 300 cycles the capacity retention of Fe<sub>2</sub>P@NPC/S, Co<sub>2</sub>P@NPC/S, and Ni<sub>2</sub>P@NPC/S were 82, 89, and 96%, respectively, much larger than that of NPC/S (55%) (Figure 15e). Although Fe<sub>2</sub>P@NPC presented the highest adsorption energy (5.34 eV) for Li<sub>2</sub>S, the cyclic performance of this cathode was inferior to that of other counterparts. This was mainly because the extremely strong adsorption ability for Li<sub>2</sub>S on Fe<sub>2</sub>P might lead to the accumulation of Li<sub>2</sub>S<sub>x</sub> on the cathode surface, further hampering the following Li<sub>2</sub>S<sub>x</sub> diffusion and conversion. This result revealed that the moderate bonding strength between Li<sub>2</sub>S and TMPs is preferred. It can be anticipated along with TMPs cathode

materials becoming a hotspot in Li–S batteries,<sup>[185]</sup> how to rationally modify the electrode structure and surface/interface features will be a major task in the future.

#### 5.4. Emerging Energy-Related Electrocatalytic Reactions

##### 5.4.1. Electrochemical CO<sub>2</sub> Reduction Reaction

The electrochemical conversion of atmospheric CO<sub>2</sub> into value-added products is quite attractive to mitigate global warming and achieves sustainable chemical energy storage.<sup>[186]</sup> In general, the electrochemical CO<sub>2</sub>RR can yield various products upon different catalysts, such as Cu for hydrocarbons, Pb, Sn

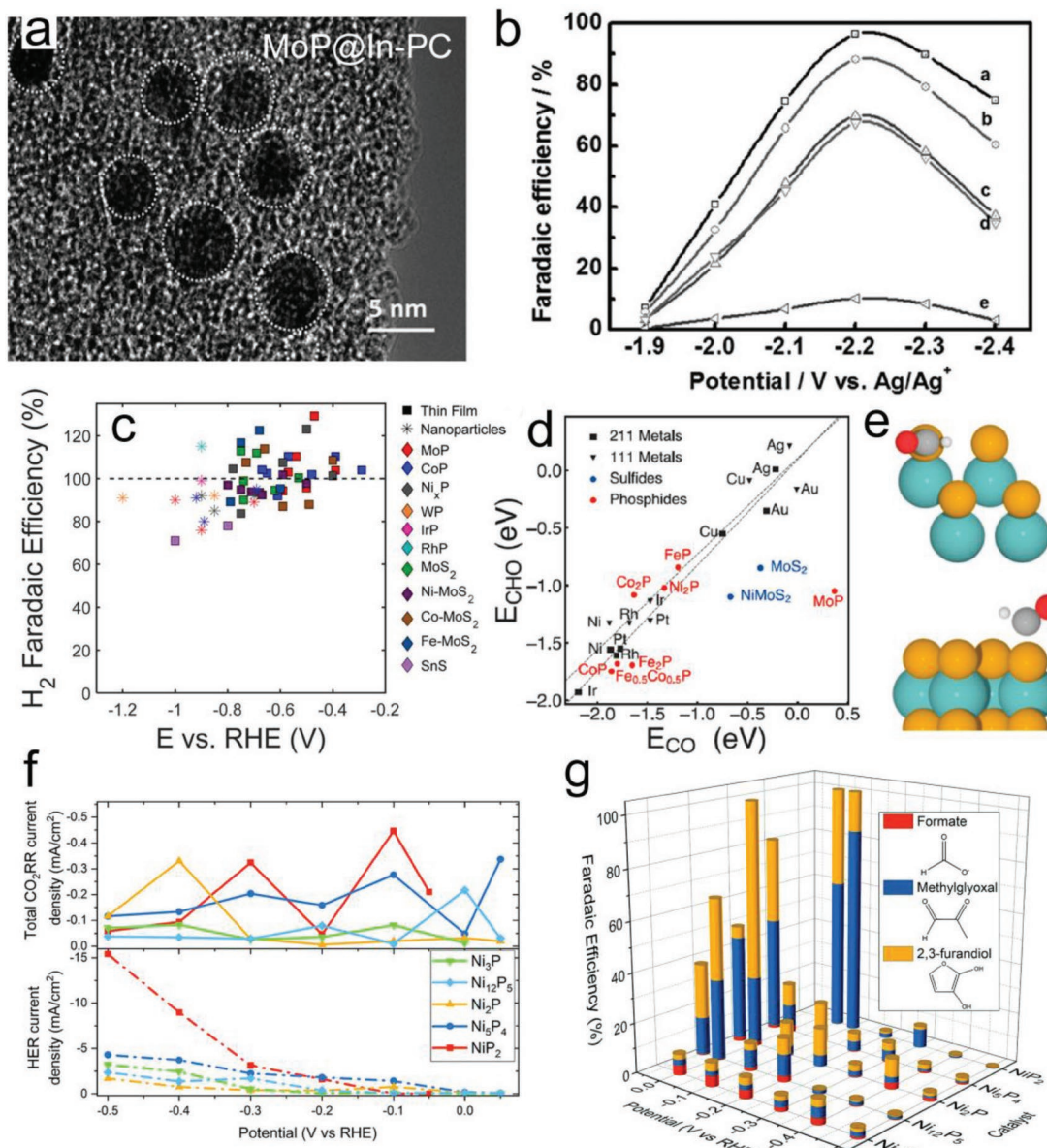


**Figure 16.** a) The TEM image of MoP@In-PC. b) Faradaic efficiency for formic acid production over a) MoP@In-PC, b) MoP@Ga-PC, c) MoP@PC-1, d) MoP@PC-2, and e) bulk MoP. Reproduced with permission.<sup>[32]</sup> Copyright 2018, John Wiley and Sons. c) Faradic efficiency of H<sub>2</sub> production under CO<sub>2</sub>RR conditions for representative transition metal phosphide and sulfide materials. d) The plot of the binding energy of CHO versus CO on surfaces at equilibrium hydrogen coverage (thermodynamic screening criteria for CO<sub>2</sub>RR). Reproduced with permission.<sup>[189]</sup> Copyright 2018, American Chemical Society. e) Top and side view of CHO bound to MoP unit cell. Reproduced with permission.<sup>[190]</sup> Copyright 2017, American Chemical Society. f) Partial current densities obtained by the product of faradaic efficiency and current density at 3 h of chronoamperometry. g) Faradaic efficiency for CO<sub>2</sub>RR as a function of potential and catalyst composition. Reproduced with permission.<sup>[191]</sup> Copyright 2018, Royal Society of Chemistry.

for formate and Au, Ag for carbon monoxide.<sup>[11c]</sup> However, the catalytic activities of these pure metals are unsatisfied resulted from the poor selectivity accompanied by a wide range of carbon products, high overpotentials, and significant H<sub>2</sub> coproduction.<sup>[12]</sup> Thermodynamic calculations have indicated that pure metal surfaces are intrinsically limited by the scaling relations between the binding affinities of successive intermediates, and thus it is difficult to optimize them separately.<sup>[187]</sup>

To circumvent the scaling limitation, the binary, even ternary metal alloys have successively appeared with promoted

reaction directionality and enhanced reaction kinetics toward CO<sub>2</sub>RR.<sup>[70,188]</sup> Similar to binary alloys, transition metal phosphides may be qualified to be CO<sub>2</sub>RR electrocatalysts due to their multifunctional active sites and good electrical conductivity. This hypothesis was firstly proved by Han's group.<sup>[32]</sup> They prepared the MoP nanoparticles supported on indium-doped porous carbon and demonstrated their application in electrochemical CO<sub>2</sub> reduction (Figure 16a). Using ionic liquid [Bmim]PF<sub>6</sub>/MeCN/H<sub>2</sub>O as the supporting electrolyte, this MoP@In-PC electrode could effectively catalyze CO<sub>2</sub> reduction

to formic acid with a large current density of  $43.8 \text{ mA cm}^{-2}$  and high faradaic efficiency of 96.5%, which was much larger than that of other counterparts and state-of-the-art Pb, Sn electrode (Figure 16b). They pointed out that the excellent catalytic performance of MoP@In-PC was caused by the synergistic effect between MoP and In-doped carbon via stabilizing the reaction intermediates. This work shed light on the novel electrocatalytic application of TMPs but intrinsic activities of TMPs in aqueous electrolytes for  $\text{CO}_2\text{RR}$  are still unknown. Considering this, Jaramillo's group investigated the  $\text{CO}_2\text{RR}$  activities on different kinds of TMPs under  $\text{CO}_2$ -saturated  $\text{KHCO}_3$  electrolyte.<sup>[189]</sup> The results indicated that TMPs presented a high faradaic efficiency toward HER relative to the  $\text{CO}_2\text{RR}$  (Figure 16c). Meanwhile, a further DFT calculation also revealed that most TMPs fell near the (211) and (111) transition metal scaling lines in the  $E_{\text{CHO}} - E_{\text{CO}}$  plot (Figure 16d), verifying that most TMPs may not offer reduced overpotential for  $\text{CO}_2\text{RR}$ . But a different case was MoP which deviated from the thermodynamic scaling line. And it had a weak bond with  $^*\text{CO}$  and a strong bond with  $^*\text{CHO}$ . This was because the (001) MoP surface was a phosphorus-terminated surface so that all adsorbates can only interact with the P sites. As displayed in Figure 16e, the phosphorus sites in MoP unit cells served as the active site for the adsorption of  $^*\text{CHO}$  intermediate. Taken this property into account, another study systematically investigated the behavior of the phosphorus active site on doped MoP for  $\text{CO}_2\text{RR}$  using DFT calculations.<sup>[190]</sup> The result revealed that MoP presented the ability to selectively distinguish chemically similar compounds by the bond order of adsorbate to the surface. Therefore, it was possible to selectively increase or decrease the binding energy toward certain adsorbates for  $\text{CO}_2\text{RR}$  on MoP.

The above results may signify that most TMPs cannot effectively catalyze  $\text{CO}_2\text{RR}$  because of kinetically favorable HER. But a recent study reversed this concept, in which uncovered the Ni-based phosphides can effectively catalyze  $\text{CO}_2$  into  $\text{C}_1$  (formic acid) and  $>\text{C}_2$  compounds (methylglyoxal and 2,3-furandiol) in aqueous media ( $\text{CO}_2$ -saturated 0.5 M  $\text{KHCO}_3$ ).<sup>[191]</sup> After investigating the electrocatalytic  $\text{CO}_2\text{RR}$  performance on five nickel phosphide compounds, including  $\text{Ni}_3\text{P}$ ,  $\text{Ni}_2\text{P}$ ,  $\text{Ni}_{12}\text{P}_5$ ,  $\text{Ni}_5\text{P}_4$ ,  $\text{NiP}_2$ , the structure–function relationships by correlating the P contents with the activity and selectivity of products were established. As shown in Figure 16f, the maximum  $\text{CO}_2\text{RR}$  specific current density of each catalyst presented a decreasing trend accompanied by the decreasing P content with achieving maximum value to  $470 \mu\text{A cm}^{-2}$  on  $\text{NiP}_2$  and minimum value on  $\text{Ni}_3\text{P}$ . While in selectivity, the maximum faradaic efficiency was approaching 84% on  $\text{NiP}_2$  at 0.10 V versus RHE for methylglyoxal, and for 2,3-furandiol the maximum value of 71% was achieved on  $\text{Ni}_3\text{P}$  at 0 V versus RHE (Figure 16g). These values are much higher than that of the state-of-the-art Cu and alloys, which yield multicarbon products with a faradic efficiency only over 1%. Interestingly, at more reductive potentials for all nickel phosphides the HER suppressed the  $\text{CO}_2\text{RR}$ , which presented an opposite behavior with that of copper catalysts. This may mean the different mechanism of  $\text{CO}_2\text{RR}$  on nickel phosphides compared with that on reported pure metal catalysts. This study proved TMPs to be the best nonbiological catalysts for the conversion  $\text{CO}_2$  to  $>\text{C}_2$  products in aqueous media but a mechanistic understanding of TMPs for  $\text{CO}_2\text{RR}$  is underexplored.

#### 5.4.2. Electrocatalysis of Organic Molecules

Although bifunctional TMPs can simultaneously split water into hydrogen and oxygen, the energy conversion efficiency is still unsatisfied mainly because the sluggish OER requires a much higher overpotential to match the rate of HER.<sup>[192]</sup> Meanwhile, the potential mixing of hydrogen and oxygen may bring about security risks.<sup>[193]</sup> In light of these issues, a feasible strategy is replacing the anodic OER with thermodynamically more favorable organic molecules electrooxidation. For example, Sun and co-workers reported the first use of a bifunctional  $\text{Ni}_2\text{P}$  electrode to simultaneously catalyze the cathodic HER and anodic 5-hydroxymethylfurfural electrooxidation.<sup>[194]</sup> This protocol could not only produce value-added products ( $\text{H}_2$ ) and updated biomass (2,5-furandicarboxylic acid) but also significantly lower the cell voltage. In comparison, Zhang and co-workers recently constructed a novel energy-saving electrolyzer with simultaneously occurring the HER and selective semidehydrogenation reaction of tetrahydroisoquinolines (THIQs, 1a) over bifunctional  $\text{Ni}_2\text{P}$  electrode (Figure 17a).<sup>[195]</sup> As displayed in Figure 17b, in the absence of THIQs, the onset potential for catalyzing OER by  $\text{Ni}_2\text{P}$  was 1.48 V versus RHE, while once introducing the THIQs, the onset potential was negatively shifted to the potential of  $\approx 1.32$  V versus RHE. More interestingly, this electrooxidized process could only yield the semi-dehydrogenation product dihydroisoquinolines (DHIQs, 2a) instead of the complete dehydrogenation product isoquinolines (Figure 17c). This controllable selective electrooxidation is mainly caused by the in situ formed  $\text{Ni}^{II}/\text{Ni}^{III}$  species on the electrode surface, which served as robust redox-active mediators to boost this conversion. As expected, to achieve a current density of  $20 \text{ mA cm}^{-2}$ , a two-electrode electrolyzer using  $\text{Ni}_2\text{P}$  for simultaneous generation of  $\text{H}_2$  and DHIQs required 300 mV smaller voltage than that of pure water splitting, indicating their much better energy conversion efficiency (Figure 17d). Similar energy-saving electrolyzers equipped with TMPs electrode have successively emerged by using the electrooxidation of hydrazine,<sup>[196]</sup> urea,<sup>[197]</sup> aloe extract,<sup>[198]</sup> to replace the sluggish OER and presented industrial practicability. Moreover, by means of directly converting chemical energy to electricity, electrochemical fuel cells hold great promise to be an ideal way for clean power generation.<sup>[199]</sup> Among them, the direct fuel cells using methanol/ethanol/formic acid as liquid fuels have attracted great attention over the past few years. However, their practical utilization is mainly impeded by the lack of robust electrocatalysts to facilitate the reaction kinetics and directionality. Although nanostructured noble metals alloys are usually regarded as the best catalysts toward these reactions, their high cost, poor carbon monoxide (CO) tolerance, and stability problem impose big obstacles on practical applications.<sup>[200]</sup> In contrast, alloying noble metals with phosphorus has been identified as a useful way to overcome the above limitations. For example, Zhao et al. employed a one-step solution-based method to prepare amorphous Pd–Ni–P nanoparticles.<sup>[201]</sup> When evaluated as electrocatalyst for methanol oxidation, Pd–Ni–P/C showed higher specific activity and catalytic durability compared with those of Pd–Ni/C, Pd/C, and commercial Pd. Besides, similar observations can be found in yolk–shell Pd–Ni–P alloy,<sup>[202]</sup> in which the introduction of

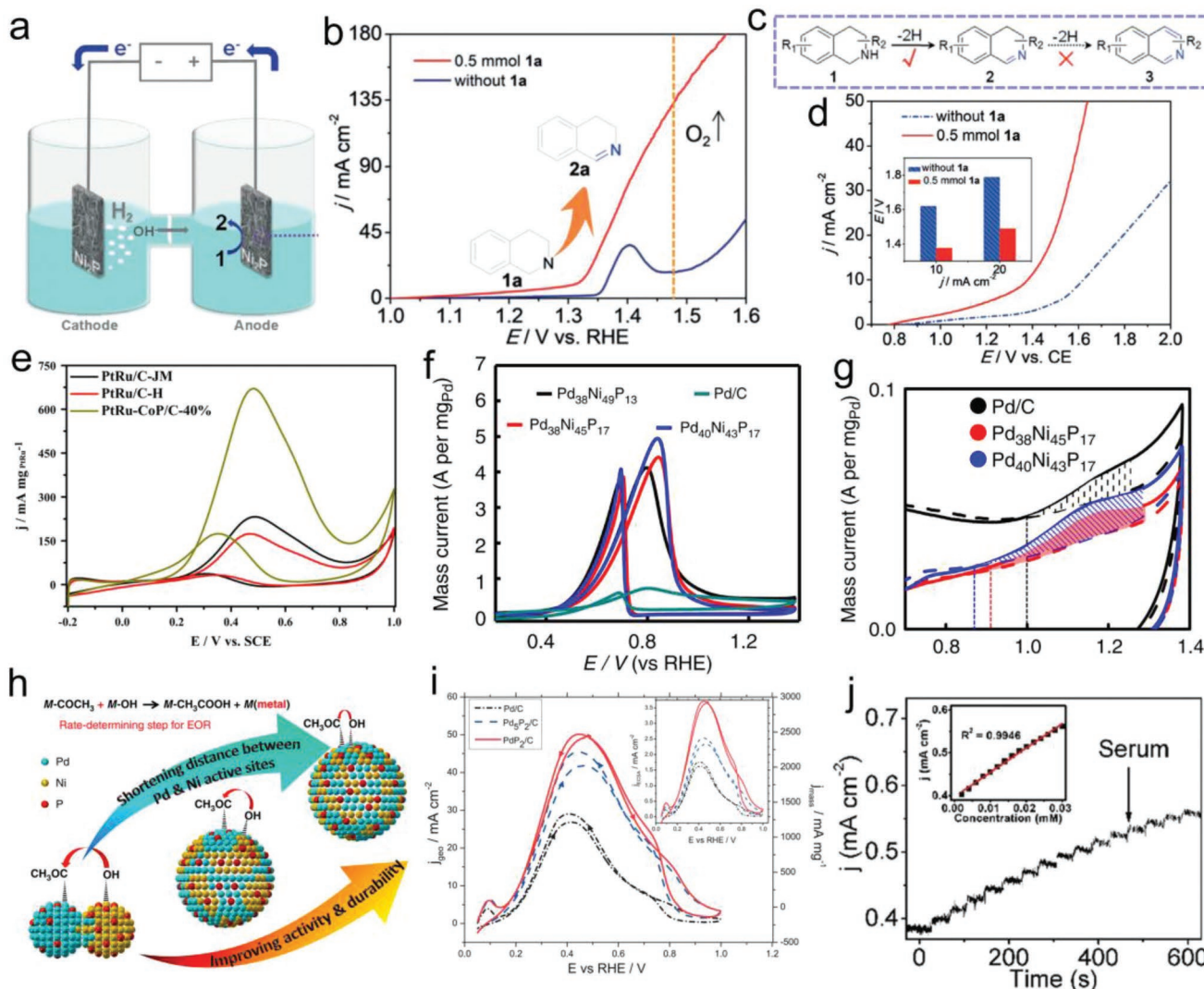


**Figure 17.** a) Electrocatalytic semidehydrogenation of THIQs 1 coupled with HER in water. b) Polarization curves of a Ni<sub>2</sub>P anode at a scan rate of 5 mV s<sup>-1</sup> in 1.0 M KOH with and without 0.5 mmol 1a. c) Dehydrogenation reaction of 1 to form DHIQs 2 and IQs 3. d) Polarization curves and potential comparison (inset) for achieving current densities (10 and 20 mA cm<sup>-2</sup>) over a Ni<sub>2</sub>P||Ni<sub>2</sub>P electrolyzer in 1.0 M KOH with and without 0.5 mmol 1a. Reproduced with permission.<sup>[195]</sup> Copyright 2019, John Wiley and Sons. e) The electrocatalytic performance of PtRu/C-JM, PtRu/C-H, and PtRu-CoP/C-40% catalysts for methanol electrooxidation in 0.5 M H<sub>2</sub>SO<sub>4</sub> with containing 1.0 M CH<sub>3</sub>OH. Reproduced with permission.<sup>[203]</sup> Copyright 2015, Elsevier. f) CV curves of different Pd–Ni–P samples and commercial Pd/C in 1.0 M NaOH with containing 1.0 M C<sub>2</sub>H<sub>5</sub>OH. g) Overlap of partial CO stripping voltammograms for the Pd/C, Pd<sub>38</sub>Ni<sub>45</sub>P<sub>17</sub>, and Pd<sub>40</sub>Ni<sub>43</sub>P<sub>17</sub> in 1.0 M NaOH. h) Schematic illustration of the enhanced electrocatalytic EOR performance on Pd–Ni–P promoted by shorted Pd–Ni active site distance. Reproduced with permission.<sup>[206]</sup> Copyright 2017, Nature Publishing Group. i) CV curves of formic acid oxidation on Pd/C, Pd<sub>5</sub>P<sub>2</sub>/C, and PdP<sub>2</sub>/C in 0.5 mol L<sup>-1</sup> H<sub>2</sub>SO<sub>4</sub> + 0.5 mol L<sup>-1</sup> HCOOH. (Inset data: surface specific activity). Reproduced with permission.<sup>[204]</sup> Copyright 2016, Elsevier. j) The amperometric responses of CoP NA/TM with the successive addition of the human blood serum sample (10%) in 0.1 M NaOH (Inset: corresponding calibration curve). Reproduced with permission.<sup>[209]</sup> Copyright 2017, Royal Society of Chemistry.

phosphorus into noble metal could endow them with enhanced catalytic properties and superior corrosion resistance. Different from the above strategy, Xing's group announced that the introduction of CoP nanoparticles into Pt–Ru/C materials can dramatically slow down the loss of Pt and Ru, thus achieving excellent stability and electrocatalytic activity for methanol oxidation.<sup>[203]</sup> As displayed in Figure 17e, the maximum peak current of 670.5 mA mg<sub>PtRu</sub><sup>-1</sup> was observed on PtRu–CoP/C-40%, which is 2.89 times higher than that of commercial PtRu/C-JM catalyst. Meanwhile, the direct methanol fuel cell equipped

with PtRu–CoP/C can deliver a higher power density of 85.7 mW cm<sup>-2</sup> than that of state-of-the-art PtRu/C catalyst, manifesting its promising prospect in practical application. Moreover, regarding the ethanol electrooxidation, Pd is thought to be more efficient electrocatalyst than that of Pt-based materials because of its relatively high activity and better resistance to CO poisoning.<sup>[204]</sup> Recently, ternary Pd–M–P (M = Cu, Ni) materials were successively fabricated and presented remarkably improved activity and stability for ethanol electrooxidation.<sup>[201,205]</sup> For instance, Wang and co-workers reported on

ternary Pd-Ni-P nanocatalysts and found that the ethanol electrooxidation activities are highly correlated with the distance between Pd sites and Ni sites.<sup>[206]</sup> By tailoring the phosphorization time and temperature, phase segregation Pd/Ni-P heterodimers ( $\text{Pd}_{38}\text{Ni}_{49}\text{P}_{13}$ , 260 °C-5 min) can be gradually alloyed into  $\text{Pd}_{38}\text{Ni}_{45}\text{P}_{17}$  nanoparticles (260 °C-1 h) and further transformed into  $\text{Pd}_{40}\text{Ni}_{43}\text{P}_{17}$  nanoparticles (260 °C-1 h and 290 °C-1 h) with closer Pd–Ni distance. As displayed in Figure 17f,  $\text{Pd}_{40}\text{Ni}_{43}\text{P}_{17}$  nanoparticles present excellent electrocatalytic activity toward ethanol electrooxidation with a mass peak current densities of 4.95 A per mg<sub>Pd</sub>, which is higher than that of  $\text{Pd}_{38}\text{Ni}_{49}\text{P}_{13}$  (4.12 A per mg<sub>Pd</sub>),  $\text{Pd}_{38}\text{Ni}_{45}\text{P}_{17}$  (4.42 A per mg<sub>Pd</sub>), and commercial Pd/C (0.72 A per mg<sub>Pd</sub>). Besides, CO antipoisoning tests manifested that the onset potentials for the electrocatalytic oxidation of CO on  $\text{Pd}_{40}\text{Ni}_{43}\text{P}_{17}$  are more negative than that of  $\text{Pd}_{38}\text{Ni}_{45}\text{P}_{17}$  NPs and commercial Pd/C, revealing that  $\text{Pd}_{40}\text{Ni}_{43}\text{P}_{17}$  nanoparticles with shorter Pd–Ni distance presented a good CO antipoisoning ability (Figure 17g). Further DFT calculation revealed that its enhanced electrocatalytic performance is stemmed from that the shortened distance between Pd and Ni active sites can significantly boost the formation of free OH radicals, thus facilitating the following combination of OH and CH<sub>3</sub>CO radicals (Figure 17h). Additionally, the electrocatalysts in formic acid oxidation reaction suffer from similar issues. In order to decrease the dosage of noble metal and improve the catalytic performance, Kucernak et al. recently prepared the homogeneous Pd<sub>2</sub>P and Pd<sub>5</sub>P<sub>2</sub> nanoparticles on carbon.<sup>[204]</sup> When evaluated as electrocatalysts for formic acid oxidation, these Pd-phosphides presented better performance than that of pure Pd/C, and the corresponding activities were positively correlated with phosphorus content (Figure 17i). Further analysis indicated that the improved performance was attributed to the increased hydrogen absorption ability as well as the oxophilic nature of surface phosphorus atoms. In comparison, nonnoble metal TMPs are also promising but their performance for these reactions is usually poorer as compared with that of noble TMPs.<sup>[33,207]</sup> Aside from these, the electrocatalytic behaviors of TMPs toward organic molecules also extend their application to biosensors.<sup>[208]</sup> For example, Sun's group fabricated the CoP nanowires on titanium mesh (CoP NA/TM) and tried it as electrode toward electro-oxidation of the glucose.<sup>[209]</sup> Since this CoP NA/TM electrode had a fast response with a wide linear range and high sensitivity toward electrooxidation of the glucose, they further extended its use to detecting the glucose in human blood serum. As depicted in the amperometric responses curve (Figure 17j), with the successive addition of human blood serum, the catalytic current presented a quick linear response, revealing its promising prospect in practical analysis. Table 2 summarizes the recent progress of TMPs in energy-related electrocatalysis applications.

## 6. Conclusions and Outlook

The search for cost-effective and highly-efficient electrocatalysts is crucial for promoting renewable energy storage and conversion by means of the electrochemical process. Following this trend, recently, TMPs hold great promise in catalyzing many

energy-related electrocatalysis reactions due to their intrinsic physicochemical properties, tunable structure, and composition. In view of remarkable breakthroughs in this field, this review has profiled recent advances of nanostructured TMPs electrocatalysts from synthesis method, modulated strategies, and corresponding applications.

In particular, we selected the HER, OER, ORR as examples and elaborately discussed the modulated strategies of TMPs toward these reactions with the aim of highlighting the theory–structure–activity relationships. Among them, elemental doping is featured with incorporating the foreign atom into the TMPs lattice to modulate the electronic structure, thus achieving optimized adsorption energy. The interfacial regulation aims to achieve synergy among different components, while the phase modification focuses on tailoring the intrinsic electrocatalytic activity by forming single crystalline, amorphous structure, or altering metal/phosphorus stoichiometric ratios. Meanwhile, the structural engineering mainly concentrates on altering the catalysts' local environment by forming porous structure or selecting suitable matrixes to expose sufficient active sites, facilitate electron and mass transfer as well as bring about sustainable stability. In comparison, coupling nanocarbons with TMPs is recognized to achieve multifunctional effects. We note that these modulated strategies are not limited in these three reactions but also are applicable in many energy-related electrocatalytic reactions. Therefore, benefited from these multiple modulated strategies, we further summarize their wide applications in water electrolyzer, metal–air batteries, Li–S batteries, carbon dioxide electroreduction, and organic molecules electrocatalysis.

Although considerable achievements have been made, some critical challenges still exist, which hinder the advance of designing high-performance TMPs electrocatalysts for further practical utilization. In the following part, we propose some facing challenges and future outlook:

**Operando Characterization Techniques:** A fundamental understanding of the catalytic behavior in each reaction will better direct the design of TMPs catalysts. Prior to identifying the active sites, an urgent task is to understand the structural evolution of catalysts and recognize the real active species during electrocatalysis. However, these established ex situ techniques may not reflect, even give misleading information due to unstable intermediate species and possible air exposure. Therefore, powerful operando characterization techniques, such as operando Raman analysis and X-ray absorption spectroscopy are highly required to unveil the real interfacial structure and reaction intermediates during these electrochemical processes. This process can not only help to revise the established theoretical model to better understand the catalytic reaction mechanism but also advance the identification of real active sites.

**Theoretical Calculation:** Although theoretical calculations have been identified as a powerful tool to offer a valuable reference for guiding catalysts design, there are still some open questions. For example, the theoretical model is always perfect single-crystal surface, while the experimental TMPs catalysts are polycrystalline, rendering that sometimes the simulation results deviate from the experimental one. Furthermore, in OER, TMPs with partial surficial oxidation are often selected as

**Table 2.** Selected energy-related electrocatalysis applications of TMPs. Water splitting, Zn-air batteries, Li–S batteries, carbon oxide reduction, energy-saving electrolyzer, methanol oxidation, ethanol oxidation, formic acid oxidation, glucose electrochemical sensor, and direct methanol fuel cell are abbreviated as “WS,” “ZABs,” “LSBs,” “CO<sub>2</sub>RR,” “ESE,” “MO,” “EO,” “FAO,” “GES,” and “DMFC,” respectively.

Materials <sup>[Ref.]</sup>	Applications	Electrochemical performance
Ni <sub>0.1</sub> Co <sub>0.9</sub> P <sup>[169]</sup>	WS in 1 M PBS	Cell voltage of 1.89 V to reach 20 mA cm <sup>-2</sup>
CoP@NiFe-OH <sup>[170]</sup>	WS in 1 M KOH	Cell voltage of 1.68 V to reach 100 mA cm <sup>-2</sup>
Cu <sub>3</sub> P@NPPC <sup>[174]</sup>	ZABs	Maximum power density of 110.8 mW cm <sup>-2</sup> at 192 mA cm <sup>-2</sup>
CoP-CNT-S <sup>[78]</sup>	LSBs	Specific capacity of 790 mAh g <sup>-1</sup> at 0.2 C after 200 cycles
S@CoP/rGO <sup>[182]</sup>	LSBs	Specific capacity of 417.3 mAh g <sup>-1</sup> and power density of 137.3 kW kg <sup>-1</sup> at 40 C
MoP-CNT-S <sup>[183]</sup>	LSBs	Specific capacity of 863 mAh g <sup>-1</sup> at 0.8 mA cm <sup>-2</sup> at lean electrolyte
Ni <sub>2</sub> P@NPC/S <sup>[184]</sup>	LSBs	96% capacity retention after 300 cycles at 0.2 C
MoP@In-PC <sup>[32]</sup>	Non aqueous CO <sub>2</sub> RR	Current density of 43.8 mA cm <sup>-2</sup> and 96.5% faradic efficiency for formic acid
Ni-based phosphides <sup>[191]</sup>	Aqueous CO <sub>2</sub> RR	71% faradic efficiency for 2,3-furandiol on Ni <sub>2</sub> P
Ni <sub>2</sub> P/Ni foam <sup>[194]</sup>	ESE	Cell voltage of 1.58 V to reach 50 mA cm <sup>-2</sup>
Ni <sub>2</sub> P/Ni foam <sup>[195]</sup>	ESE	300 mV smaller voltage than that of water electrolyzer at 20 mA cm <sup>-2</sup>
Pd–Ni–P nanoparticles <sup>[201]</sup>	MO	3.5% loss of current density after 400 CV cycles
Pd–Ni–P alloy <sup>[202]</sup>	MO	87% current density retention after 2000 CV cycles
PtRu–CoP/C-40% <sup>[203]</sup>	DMFC	Power density of 85.7 mW cm <sup>-2</sup> at 30 °C
Pd <sub>40</sub> Ni <sub>43</sub> P <sub>17</sub> nanoparticles <sup>[206]</sup>	EO	Mass peak current densities of 4.95 A per mg <sub>Pd</sub>
Pd-based phosphides <sup>[204]</sup>	FAO	A peak current density over 60% higher than that of Pd/C
CoP NA/TM <sup>[209]</sup>	GES	Good response of blood glucose

the theoretical model to calculate the reaction energy barriers, while ample experimental results have indicated that upon OER, the surface of TMPs is evolved into the metal oxides/oxyhydroxides. Therefore, more accurate theoretical models are needed. Regarding these much more complex reaction processes, more attention should be paid to the fundamental understanding of reaction pathways in TMPs for ORR, CO<sub>2</sub>RR so that we can accordingly propose effective modulated strategies toward TMPs to expedite the reaction rates.

**Recommended Practices and Benchmark Evaluation Criteria:** To obtain reliable data to evaluate catalysts' performance, more focuses should be given on the electrochemical test. For example, in linear sweep voltammetry method when voltage is scanned from the negative to the positive direction to evaluate the OER activity, the oxidation peak of TMPs often overlap with the OER onset currents, potentially leading to the overestimation of their activities. Besides, a fast scanning rate in linear sweep voltammetry test can yield large background capacitive current, especially for the 3D self-supported electrode, rendering a wrong judgment of their activity. Therefore, the electrochemical test should be carefully performed and here are some recommended practices that can be referred.<sup>[210]</sup> Furthermore, to promote the practical application of TMPs in these energy-related technologies, it is an urgent task to set up some new evaluation criteria. For example, in overall water splitting, the hydrogen production rate normalized per catalyst mass loading catalysts at a constant voltage can be served as an assessment standard to better evaluate the performance of electrocatalysts.

**Practical Applications:** To make these energy-related electrocatalytic technologies into commercially available the cost of electrocatalysts should be taken into first consideration. In this case, earth-abundant transition metal iron and nickel-based

phosphides naturally become an ideal choice in the long run. While in the middle-term, some ruthenium-based phosphides are also appealing as compared with noble-metal-free TMPs because ruthenium-based phosphides indeed show similar, even better performance than that of pure platinum in catalyzing HER and ORR over a wide pH range. Regarding the cost, the price of Ru is nearly three times lower than that of Pt, and the formation of ruthenium-based phosphides can further decrease the dosage of noble Ru. Hence, one thing that should be done now is lowering the synthesis cost of ruthenium-based phosphides catalysts. Another way is the integration of electrochemical devices with the renewable power source, such as photovoltaic modules or wind generator can significantly lower the total cost by rational design of corresponding setup configuration.

In summary, recent work has witnessed the possibility of TMPs in multifunctional electrocatalysis technologies to alleviate intractable energy and environmental issues. Despite huge challenges ahead, it is envisaged that the ongoing research efforts in theoretical calculation and experiment will give rise to the best TMPs catalysts and being put into the market. Therefore, the clean, sustainable society is expected to be achieved in the near future.

## Acknowledgements

Y.L. and Z.D. contributed equally to this work. This work was financially supported by the National Natural Science Foundation of China (51622102, 51571124, 21421001), the MOST (2017YFA0206702), the 111 Project (B12015), Natural Science Foundation of Tianjin (18ZXJMTG00040, 16PTSYJC00030), and the Fundamental Research Funds for the Central Universities.

## Conflict of Interest

The authors declare no conflict of interest.

## Keywords

electrocatalysis, modulated strategies, novel applications, theory–structure–activity relationships, transition metal phosphides

Received: June 29, 2019

Revised: August 24, 2019

Published online:

- [1] a) P. De Luna, C. Hahn, D. Higgins, S. A. Jaffer, T. F. Jaramillo, E. H. Sargent, *Science* **2019**, *364*, eaav3506; b) C. F. Shih, T. Zhang, J. Li, C. Bai, *Joule* **2018**, *2*, 1925; c) R. Service, *Science* **2018**, *361*, 120.
- [2] a) S. Chu, Y. Cui, N. Liu, *Nat. Mater.* **2017**, *16*, 16; b) R. Paul, L. Zhu, H. Chen, J. Qu, L. Dai, *Adv. Mater.* **2019**, *31*, 1806403; c) Q. Zhao, Z. Yan, C. Chen, J. Chen, *Chem. Rev.* **2017**, *117*, 10121; d) K. Chang, X. Hai, J. Ye, *Adv. Energy Mater.* **2016**, *6*, 1502555.
- [3] a) S. Anantharaj, S. R. Ede, K. Sakthikumar, K. Karthick, S. Mishra, S. Kundu, *ACS Catal.* **2016**, *6*, 8069; b) Z. W. Seh, J. Kibsgaard, C. F. Dickens, I. Chorkendorff, J. K. Nørskov, T. F. Jaramillo, *Science* **2017**, *355*, eaad4998; c) S. Dresp, F. Dionigi, M. Klingenhof, P. Strasser, *ACS Energy Lett.* **2019**, *4*, 933.
- [4] a) X. Duan, J. Xu, Z. Wei, J. Ma, S. Guo, S. Wang, H. Liu, S. Dou, *Adv. Mater.* **2017**, *29*, 1701784; b) W. Tu, Y. Zhou, Z. Zou, *Adv. Mater.* **2014**, *26*, 4607; c) T. Zheng, K. Jiang, H. Wang, *Adv. Mater.* **2018**, *30*, 1802066.
- [5] a) Y. Liu, Y. Li, H. Kang, T. Jin, L. Jiao, *Mater. Horiz.* **2016**, *3*, 402; b) X. Zou, Y. Zhang, *Chem. Soc. Rev.* **2015**, *44*, 5148; c) N. T. Suen, S. F. Hung, Q. Quan, N. Zhang, Y. J. Xu, H. M. Chen, *Chem. Soc. Rev.* **2017**, *46*, 337.
- [6] a) L. Dai, Y. Xue, L. Qu, H.-J. Choi, J.-B. Baek, *Chem. Rev.* **2015**, *115*, 4823; b) J. Wang, W. Cui, Q. Liu, Z. Xing, A. M. Asiri, X. Sun, *Adv. Mater.* **2016**, *28*, 215; c) J. Wang, F. Xu, H. Jin, Y. Chen, Y. Wang, *Adv. Mater.* **2017**, *29*, 1605838.
- [7] a) Y. Jiao, Y. Zheng, M. Jaroniec, S. Z. Qiao, *Chem. Soc. Rev.* **2015**, *44*, 2060; b) M. S. Faber, S. Jin, *Energy Environ. Sci.* **2014**, *7*, 3519.
- [8] a) J. K. Nørskov, T. Bligaard, J. Rossmeisl, C. H. Christensen, *Nat. Chem.* **2009**, *1*, 37; b) F. Abild-Pedersen, J. Greeley, F. Studt, J. Rossmeisl, T. R. Munter, P. G. Moses, E. Skúlason, T. Bligaard, J. K. Nørskov, *Phys. Rev. Lett.* **2007**, *99*, 016105.
- [9] a) C. G. Morales-Guio, L. A. Stern, X. Hu, *Chem. Soc. Rev.* **2014**, *43*, 6555; b) C. R. Zhu, D. Gao, J. Ding, D. Chao, J. Wang, *Chem. Soc. Rev.* **2018**, *47*, 4332.
- [10] a) B. Hinnemann, P. G. Moses, J. Bonde, K. P. Jørgensen, J. H. Nielsen, S. Horch, I. Chorkendorff, J. K. Nørskov, *J. Am. Chem. Soc.* **2005**, *127*, 5308; b) T. F. Jaramillo, K. P. Jørgensen, J. Bonde, J. H. Nielsen, S. Horch, I. Chorkendorff, *Science* **2007**, *317*, 100.
- [11] a) Q. Shi, C. Zhu, D. Du, Y. Lin, *Chem. Soc. Rev.* **2019**, *48*, 3181; b) Z. Xia, L. An, P. Chen, D. Xia, *Adv. Energy Mater.* **2016**, *6*, 1600458; c) W. Zhang, Y. Hu, L. Ma, G. Zhu, Y. Wang, X. Xue, R. Chen, S. Yang, Z. Jin, *Adv. Sci.* **2018**, *5*, 1700275; d) M. Shao, Q. Chang, J.-P. Dodelet, R. Chenitz, *Chem. Rev.* **2016**, *116*, 3594.
- [12] J. Wu, Y. Huang, W. Ye, Y. Li, *Adv. Sci.* **2017**, *4*, 1700194.
- [13] a) Y. Li, H. Wang, L. Xie, Y. Liang, G. Hong, H. Dai, *J. Am. Chem. Soc.* **2011**, *133*, 7296; b) M. A. Lukowski, A. S. Daniel, F. Meng, A. Forticaux, L. Li, S. Jin, *J. Am. Chem. Soc.* **2013**, *135*, 10274.
- [14] a) L. Xu, Q. Jiang, Z. Xiao, X. Li, J. Huo, S. Wang, L. Dai, *Angew. Chem., Int. Ed.* **2016**, *55*, 5277; b) J. Xu, P. Gao, T. Zhao, *Energy Environ. Sci.* **2012**, *5*, 5333.
- [15] a) H. Xie, T. Wang, J. Liang, Q. Li, S. Sun, *Nano Today* **2018**, *21*, 41; b) A. Loijudice, P. Lobaccaro, E. A. Kamali, T. Thao, B. H. Huang, J. W. Ager, R. Buonsanti, *Angew. Chem., Int. Ed.* **2016**, *55*, 5789.
- [16] a) D. Kong, H. Wang, J. J. Cha, M. Pasta, K. J. Koski, J. Yao, Y. Cui, *Nano Lett.* **2013**, *13*, 1341; b) Y. Sun, F. Alimohammadi, D. Zhang, G. Guo, *Nano Lett.* **2017**, *17*, 1963.
- [17] Y. Liang, Y. Li, H. Wang, J. Zhou, J. Wang, T. Regier, H. Dai, *Nat. Mater.* **2011**, *10*, 780.
- [18] a) H. Zhao, Z.-Y. Yuan, *Catal. Sci. Technol.* **2017**, *7*, 330; b) S. Izhar, M. Nagai, *Catal. Today* **2009**, *146*, 172; c) H. Du, R. M. Kong, X. Guo, F. Qu, J. Li, *Nanoscale* **2018**, *10*, 21617.
- [19] M. Sun, H. Liu, J. Qu, J. Li, *Adv. Energy Mater.* **2016**, *6*, 1600087.
- [20] S. Carencio, D. Portehault, C. Boissière, N. Mézailles, C. Sanchez, *Chem. Rev.* **2013**, *113*, 7981.
- [21] J. F. Callejas, C. G. Read, C. W. Roske, N. S. Lewis, R. E. Schaak, *Chem. Mater.* **2016**, *28*, 6017.
- [22] J.-H. Chen, K. H. Whitmire, *Coord. Chem. Rev.* **2018**, *355*, 271.
- [23] B. Owens-Baird, Y. V. Kolen'ko, K. Kovnir, *Chem. Eur. J.* **2018**, *24*, 7298.
- [24] Y. Lv, X. Wang, *Catal. Sci. Technol.* **2017**, *7*, 3676.
- [25] a) P. Liu, J. A. Rodriguez, *Catal. Lett.* **2003**, *91*, 247; b) P. Xiao, W. Chen, X. Wang, *Adv. Energy Mater.* **2015**, *5*, 1500985.
- [26] a) Y. Shi, B. Zhang, *Chem. Soc. Rev.* **2016**, *45*, 1529; b) Y. Pei, Y. Cheng, J. Chen, W. Smith, P. Dong, P. M. Ajayan, M. Ye, J. Shen, *J. Mater. Chem. A* **2018**, *6*, 23220.
- [27] a) P. Liu, J. A. Rodriguez, *J. Am. Chem. Soc.* **2005**, *127*, 14871; b) E. J. Popczun, J. R. McKone, C. G. Read, A. J. Biacchi, A. M. Wiltrot, N. S. Lewis, R. E. Schaak, *J. Am. Chem. Soc.* **2013**, *135*, 9267.
- [28] a) J. Ryu, N. Jung, J. H. Jang, H.-J. Kim, S. J. Yoo, *ACS Catal.* **2015**, *5*, 4066; b) V. V. T. Doan-Nguyen, S. Zhang, E. B. Trigg, R. Agarwal, J. Li, D. Su, K. I. Winey, C. B. Murray, *ACS Nano* **2015**, *9*, 8108.
- [29] M. Ledendecker, S. Krick Calderón, C. Papp, H. P. Steinrück, M. Antonietti, M. Shalom, *Angew. Chem., Int. Ed.* **2015**, *54*, 12361.
- [30] Q. Qin, H. Jang, P. Li, B. Yuan, X. Liu, J. Cho, *Adv. Energy Mater.* **2019**, *9*, 1803312.
- [31] Y. Lv, Y. Lin, L. Yang, Z. Cai, B. Jing, J. Yu, X. Jiang, Z. Xing, J. Zou, *Chem. Eng. J.* **2018**, *342*, 228.
- [32] X. Sun, L. Lu, Q. Zhu, C. Wu, D. Yang, C. Chen, B. Han, *Angew. Chem., Int. Ed.* **2018**, *57*, 2427.
- [33] C. Zhu, S. Fu, B. Z. Xu, J. Song, Q. Shi, M. H. Engelhard, X. Li, S. P. Beckman, J. Sun, D. Du, Y. Lin, *Small* **2017**, *13*, 1700796.
- [34] Y. Mi, W. Liu, X. Li, J. Zhuang, H. Zhou, H. Wang, *Nano Res.* **2017**, *10*, 3698.
- [35] H. B. Wu, B. Y. Xia, L. Yu, X. Y. Yu, X. W. Lou, *Nat. Commun.* **2015**, *6*, 6512.
- [36] B. Cao, G. M. Veith, J. C. Neufeld, R. R. Adzic, P. G. Khalifah, *J. Am. Chem. Soc.* **2013**, *135*, 19186.
- [37] K. Jiang, S. Siahrostami, T. Zheng, Y. Hu, S. Hwang, E. Stavitski, Y. Peng, J. Dynes, M. Gangisetty, D. Su, K. Attenkofer, H. Wang, *Energy Environ. Sci.* **2018**, *11*, 893.
- [38] T. H. M. Lau, S. Wu, R. Kato, T.-S. Wu, J. Kulhavý, J. Mo, J. Zheng, J. S. Foord, Y.-L. Soo, K. Suenaga, M. T. Darby, S. C. E. Tsang, *ACS Catal.* **2019**, *9*, 7527.
- [39] Y. Wang, B. Kong, D. Zhao, H. Wang, C. Selomulya, *Nano Today* **2017**, *15*, 26.
- [40] Y. Zang, S. Niu, Y. Wu, X. Zheng, J. Cai, J. Ye, Y. Xie, Y. Liu, J. Zhou, J. Zhu, X. Liu, G. Wang, Y. Qian, *Nat. Commun.* **2019**, *10*, 1217.
- [41] a) Y. Zhong, X. Xia, F. Shi, J. Zhan, J. Tu, H. J. Fan, *Adv. Sci.* **2016**, *3*, 1500286; b) M.-S. Balogun, Y. Huang, W. Qiu, H. Yang, H. Ji, Y. Tong, *Mater. Today* **2017**, *20*, 425.
- [42] C. W. Lee, K. D. Yang, D.-H. Nam, J. H. Jang, N. H. Cho, S. W. Im, K. T. Nam, *Adv. Mater.* **2018**, *30*, 1704717.
- [43] P. Yu, F. Wang, T. A. Shifa, X. Zhan, X. Lou, F. Xia, J. He, *Nano Energy* **2019**, *58*, 244.

- [44] F. H. Saadi, A. I. Carim, W. S. Drisdell, S. Gul, J. H. Baricuatro, J. Yano, M. P. Soriaga, N. S. Lewis, *J. Am. Chem. Soc.* **2017**, *139*, 12927.
- [45] A. Wang, M. Qin, J. Guan, L. Wang, H. Guo, X. Li, Y. Wang, R. Prins, Y. Hu, *Angew. Chem., Int. Ed.* **2008**, *47*, 6052.
- [46] a) G. Zhang, G. Wang, Y. Liu, H. Liu, J. Qu, J. Li, *J. Am. Chem. Soc.* **2016**, *138*, 14686; b) T. Q. Zhang, J. Liu, L. B. Huang, X. D. Zhang, Y. G. Sun, X. C. Liu, D. S. Bin, X. Chen, A. M. Cao, J. S. Hu, L. J. Wan, *J. Am. Chem. Soc.* **2017**, *139*, 11248.
- [47] a) Y. Pan, K. Sun, S. Liu, X. Cao, K. Wu, W. C. Cheong, Z. Chen, Y. Wang, Y. Li, Y. Liu, D. Wang, Q. Peng, C. Chen, Y. Li, *J. Am. Chem. Soc.* **2018**, *140*, 2610; b) H. Tabassum, W. Guo, W. Meng, A. Mahmood, R. Zhao, Q. Wang, R. Zou, *Adv. Energy Mater.* **2017**, *7*, 1601671.
- [48] X. Wang, L. Chai, J. Ding, L. Zhong, Y. Du, T.-T. Li, Y. Hu, J. Qian, S. Huang, *Nano Energy* **2019**, *62*, 745.
- [49] J. Xiao, Z. Zhang, Y. Zhang, Q. Lv, F. Jing, K. Chi, S. Wang, *Nano Energy* **2018**, *51*, 223.
- [50] F. Bu, W. Chen, M. F. Aly Aboud, I. Shakir, J. Gu, Y. Xu, *J. Mater. Chem. A* **2019**, *7*, 14526.
- [51] H. Liang, A. N. Gandi, D. H. Anjum, X. Wang, U. Schwingenschlögl, H. N. Alshareef, *Nano Lett.* **2016**, *16*, 7718.
- [52] E. J. Popczun, C. G. Read, C. W. Roske, N. S. Lewis, R. E. Schaak, *Angew. Chem., Int. Ed.* **2014**, *53*, 5427.
- [53] Z. Xing, Q. Liu, A. M. Asiri, X. Sun, *Adv. Mater.* **2014**, *26*, 5702.
- [54] P. Jiang, Q. Liu, Y. Liang, J. Tian, A. M. Asiri, X. Sun, *Angew. Chem., Int. Ed.* **2014**, *53*, 12855.
- [55] Q. Liu, J. Tian, W. Cui, P. Jiang, N. Cheng, A. M. Asiri, X. Sun, *Angew. Chem., Int. Ed.* **2014**, *53*, 6710.
- [56] Z. S. Wu, L. Huang, H. Liu, H. L. Wang, *ACS Catal.* **2019**, *9*, 2956.
- [57] Z. Wu, Q. Gan, X. Li, Y. Zhong, H. Wang, *J. Phys. Chem. C* **2018**, *122*, 2848.
- [58] Y. Zhang, L. Gao, E. J. M. Hensen, J. P. Hofmann, *ACS Energy Lett.* **2018**, *3*, 1360.
- [59] J. S. Kim, B. Kim, H. Kim, K. Kang, *Adv. Energy Mater.* **2018**, *8*, 1702774.
- [60] Z. Yan, H. Sun, X. Chen, H. Liu, Y. Zhao, H. Li, W. Xie, F. Cheng, J. Chen, *Nat. Commun.* **2018**, *9*, 2373.
- [61] F. Cheng, J. Shen, B. Peng, Y. Pan, Z. Tao, J. Chen, *Nat. Chem.* **2011**, *3*, 79.
- [62] M. W. Kanan, D. G. Nocera, *Science* **2008**, *321*, 1072.
- [63] A. Dutta, N. Pradhan, *J. Phys. Chem. Lett.* **2017**, *8*, 144.
- [64] S. Jin, *ACS Energy Lett.* **2017**, *2*, 1937.
- [65] J. Chang, Y. Xiao, M. Xiao, J. Ge, C. Liu, W. Xing, *ACS Catal.* **2015**, *5*, 6874.
- [66] Z.-F. Huang, J. Wang, Y. Peng, C.-Y. Jung, A. Fisher, X. Wang, *Adv. Energy Mater.* **2017**, *7*, 1700544.
- [67] a) S. Fu, C. Zhu, J. Song, D. Du, Y. Lin, *Adv. Energy Mater.* **2017**, *7*, 1700363; b) Z. Xia, S. Guo, *Chem. Soc. Rev.* **2019**, *48*, 3265.
- [68] K. P. Singh, E. J. Bae, J.-S. Yu, *J. Am. Chem. Soc.* **2015**, *137*, 3165.
- [69] M. Li, T. Liu, X. Bo, M. Zhou, L. Guo, S. Guo, *Nano Energy* **2017**, *33*, 221.
- [70] D. D. Zhu, J. L. Liu, S. Z. Qiao, *Adv. Mater.* **2016**, *28*, 3423.
- [71] Y. Wang, J. Liu, Y. Wang, A. M. Al-Enizi, G. Zheng, *Small* **2017**, *13*, 1701809.
- [72] P. G. Bruce, S. A. Freunberger, L. J. Hardwick, J.-M. Tarascon, *Nat. Mater.* **2012**, *11*, 19.
- [73] Y. Z. Song, W. L. Cai, L. Kong, J. S. Cai, Q. Zhang, J. Y. Sun, *Adv. Energy Mater.* **2019**, <https://doi.org/10.1002/aenm.201901075>.
- [74] H. J. Peng, Z. W. Zhang, J. Q. Huang, G. Zhang, J. Xie, W. T. Xu, J. L. Shi, X. Chen, X. B. Cheng, Q. Zhang, *Adv. Mater.* **2016**, *28*, 9551.
- [75] Z.-L. Xu, J.-K. Kim, K. Kang, *Nano Today* **2018**, *19*, 84.
- [76] X. Liu, J. Q. Huang, Q. Zhang, L. Mai, *Adv. Mater.* **2017**, *29*, 1601759.
- [77] J. Shen, X. Xu, J. Liu, Z. Liu, F. Li, R. Hu, J. Liu, X. Hou, Y. Feng, Y. Yu, M. Zhu, *ACS Nano* **2019**, *13*, 8986.
- [78] Y. Zhong, L. Yin, P. He, W. Liu, Z. Wu, H. Wang, *J. Am. Chem. Soc.* **2018**, *140*, 1455.
- [79] V. R. Stamenkovic, D. Strmcnik, P. P. Lopes, N. M. Markovic, *Nat. Mater.* **2017**, *16*, 57.
- [80] a) C. Tang, H. F. Wang, Q. Zhang, *Acc. Chem. Res.* **2018**, *51*, 881; b) B. Wang, C. Tang, H.-F. Wang, X. Chen, R. Cao, Q. Zhang, *J. Energy Chem.* **2019**, *38*, 8.
- [81] J. Kibsgaard, C. Tsai, K. Chan, J. D. Benck, J. K. Nørskov, F. Abild-Pedersen, T. F. Jaramillo, *Energy Environ. Sci.* **2015**, *8*, 3022.
- [82] W. Gu, L. Gan, X. Zhang, E. Wang, J. Wang, *Nano Energy* **2017**, *34*, 421.
- [83] T. Liu, D. Liu, F. Qu, D. Wang, L. Zhang, R. Ge, S. Hao, Y. Ma, G. Du, A. M. Asiri, L. Chen, X. Sun, *Adv. Energy Mater.* **2017**, *7*, 1700020.
- [84] T. Liu, X. Ma, D. Liu, S. Hao, G. Du, Y. Ma, A. M. Asiri, X. Sun, L. Chen, *ACS Catal.* **2017**, *7*, 98.
- [85] X. Xiao, L. Tao, M. Li, X. Lv, D. Huang, X. Jiang, H. Pan, M. Wang, Y. Shen, *Chem. Sci.* **2018**, *9*, 1970.
- [86] W. Gao, M. Yan, H.-Y. Cheung, Z. Xia, X. Zhou, Y. Qin, C.-Y. Wong, J. C. Ho, C.-R. Chang, Y. Qu, *Nano Energy* **2017**, *38*, 290.
- [87] J. Song, C. Zhu, B. Z. Xu, S. Fu, M. H. Engelhard, R. Ye, D. Du, S. P. Beckman, Y. Lin, *Adv. Energy Mater.* **2017**, *7*, 1601555.
- [88] Y. Wu, X. Tao, Y. Qing, H. Xu, F. Yang, S. Luo, C. Tian, M. Liu, X. Lu, *Adv. Mater.* **2019**, *31*, 1900178.
- [89] Y. Liu, S. Liu, Y. Wang, Q. Zhang, L. Gu, S. Zhao, D. Xu, Y. Li, J. Bao, Z. Dai, *J. Am. Chem. Soc.* **2018**, *140*, 2731.
- [90] C. Guan, W. Xiao, H. Wu, X. Liu, W. Zang, H. Zhang, J. Ding, Y. P. Feng, S. J. Pennycook, J. Wang, *Nano Energy* **2018**, *48*, 73.
- [91] V. R. Jothi, R. Bose, H. Rajan, C. Jung, S. C. Yi, *Adv. Energy Mater.* **2018**, *8*, 1802615.
- [92] J. Xu, J. Li, D. Xiong, B. Zhang, Y. Liu, K.-H. Wu, I. Amorim, W. Li, L. Liu, *Chem. Sci.* **2018**, *9*, 3470.
- [93] J. Kibsgaard, T. F. Jaramillo, *Angew. Chem., Int. Ed.* **2014**, *53*, 14433.
- [94] M. Cabán-Acevedo, M. L. Stone, J. R. Schmidt, J. G. Thomas, Q. Ding, H.-C. Chang, M.-L. Tsai, J.-H. He, S. Jin, *Nat. Mater.* **2015**, *14*, 1245.
- [95] W. Liu, E. Hu, H. Jiang, Y. Xiang, Z. Weng, M. Li, Q. Fan, X. Yu, E. I. Altman, H. Wang, *Nat. Commun.* **2016**, *7*, 10771.
- [96] Y.-R. Zheng, P. Wu, M.-R. Gao, X.-L. Zhang, F.-Y. Gao, H.-X. Ju, R. Wu, Q. Gao, R. You, W.-X. Huang, S.-J. Liu, S.-W. Hu, J. Zhu, Z. Li, S.-H. Yu, *Nat. Commun.* **2018**, *9*, 2533.
- [97] M. A. R. Anjum, M. D. Bhatt, M. H. Lee, J. S. Lee, *Chem. Mater.* **2018**, *30*, 8861.
- [98] Y. Xin, X. Kan, L. Y. Gan, Z. Zhang, *ACS Nano* **2017**, *11*, 10303.
- [99] J. Duan, S. Chen, A. Vasileff, S. Z. Qiao, *ACS Nano* **2016**, *10*, 8738.
- [100] K. Liu, F. Wang, P. He, T. A. Shifa, Z. Wang, Z. Cheng, X. Zhan, J. He, *Adv. Energy Mater.* **2018**, *8*, 1703290.
- [101] H. J. Song, H. Yoon, B. Ju, G.-H. Lee, D.-W. Kim, *Adv. Energy Mater.* **2018**, *8*, 1802319.
- [102] P. Chen, Y. Tong, C. Wu, Y. Xie, *Acc. Chem. Res.* **2018**, *51*, 2857.
- [103] Y. Yang, M. Luo, W. Zhang, Y. Sun, X. Chen, S. Guo, *Chem* **2018**, *4*, 2054.
- [104] T. Liu, A. Li, C. Wang, W. Zhou, S. Liu, L. Guo, *Adv. Mater.* **2018**, *30*, 1803590.
- [105] L. Zeng, K. Sun, X. Wang, Y. Liu, Y. Pan, Z. Liu, D. Cao, Y. Song, S. Liu, C. Liu, *Nano Energy* **2018**, *51*, 26.
- [106] H. Yan, Y. Xie, A. Wu, Z. Cai, L. Wang, C. Tian, X. Zhang, H. Fu, *Adv. Mater.* **2019**, *31*, 1901174.
- [107] Y. Ge, P. Dong, S. R. Craig, P. M. Ajayan, M. Ye, J. Shen, *Adv. Energy Mater.* **2018**, *8*, 1800484.
- [108] Z.-H. Xue, H. Su, Q.-Y. Yu, B. Zhang, H.-H. Wang, X.-H. Li, J.-S. Chen, *Adv. Energy Mater.* **2017**, *7*, 1602355.
- [109] X. Li, W. Liu, M. Zhang, Y. Zhong, Z. Weng, Y. Mi, Y. Zhou, M. Li, J. J. Cha, Z. Tang, H. Jiang, X. Li, H. Wang, *Nano Lett.* **2017**, *17*, 2057.

- [110] J. X. Feng, S. Y. Tong, Y. X. Tong, G. R. Li, *J. Am. Chem. Soc.* **2018**, *140*, 5118.
- [111] J. Y. Li, H. X. Liu, W. Y. Gou, M. K. Zhang, Z. M. Xia, S. Zhang, C. R. Chang, Y. Y. Ma, Y. Q. Qu, *Energy Environ. Sci.* **2019**, *12*, 2298.
- [112] a) J. Zhang, T. Wang, D. Pohl, B. Rellinghaus, R. Dong, S. Liu, X. Zhuang, X. Feng, *Angew. Chem., Int. Ed.* **2016**, *55*, 6702; b) D. Strmcnik, P. P. Lopes, B. Genorio, V. R. Stamenkovic, N. M. Markovic, *Nano Energy* **2016**, *29*, 29.
- [113] J. Hu, C. Zhang, L. Jiang, H. Lin, Y. An, D. Zhou, M. K. H. Leung, S. Yang, *Joule* **2017**, *1*, 383.
- [114] K. Xu, H. Cheng, H. Lv, J. Wang, L. Liu, S. Liu, X. Wu, W. Chu, C. Wu, Y. Xie, *Adv. Mater.* **2018**, *30*, 1703322.
- [115] T. Zhang, K. Yang, C. Wang, S. Li, Q. Zhang, X. Chang, J. Li, S. Li, S. Jia, J. Wang, L. Fu, *Adv. Energy Mater.* **2018**, *8*, 1801690.
- [116] X. Liu, Q. Hu, B. Zhu, G. Li, L. Fan, X. Chai, Q. Zhang, J. Liu, C. He, *Small* **2018**, *14*, 1802755.
- [117] B. You, Y. Zhang, Y. Jiao, K. Davey, S. Z. Qiao, *Angew. Chem., Int. Ed.* **2019**, *58*, 11796.
- [118] X. Zhang, J. Li, Y. Yang, S. Zhang, H. Zhu, X. Zhu, H. Xing, Y. Zhang, B. Huang, S. Guo, E. Wang, *Adv. Mater.* **2018**, *30*, 1803551.
- [119] Y. Zheng, Y. Jiao, M. Jaroniec, S. Z. Qiao, *Angew. Chem., Int. Ed.* **2015**, *54*, 52.
- [120] Y. Zheng, Y. Jiao, A. Vasileff, S.-Z. Qiao, *Angew. Chem., Int. Ed.* **2018**, *57*, 7568.
- [121] C. Zhang, Y. Huang, Y. Yu, J. Zhang, S. Zhuo, B. Zhang, *Chem. Sci.* **2017**, *8*, 2769.
- [122] W. Zhang, Y. Zou, H. Liu, S. Chen, X. Wang, H. Zhang, X. She, D. Yang, *Nano Energy* **2019**, *56*, 813.
- [123] W. Li, X. Gao, D. Xiong, F. Xia, J. Liu, W. G. Song, J. Xu, S. M. Thalluri, M. F. Cerqueira, X. Fu, L. Liu, *Chem. Sci.* **2017**, *8*, 2952.
- [124] T. Wu, M. L. Stone, M. J. Shearer, M. J. Stolt, I. A. Guzei, R. J. Hamers, R. Lu, K. Deng, S. Jin, J. R. Schmidt, *ACS Catal.* **2018**, *8*, 1143.
- [125] B. R. Goldsmith, B. Peters, J. K. Johnson, B. C. Gates, S. L. Scott, *ACS Catal.* **2017**, *7*, 7543.
- [126] I. Paseka, *Electrochim. Acta* **1995**, *40*, 1633.
- [127] J. M. McEnaney, J. C. Crompton, J. F. Callejas, E. J. Popczun, A. J. Biacchi, N. S. Lewis, R. E. Schaak, *Chem. Mater.* **2014**, *26*, 4826.
- [128] J. M. McEnaney, J. C. Crompton, J. F. Callejas, E. J. Popczun, C. G. Read, N. S. Lewis, R. E. Schaak, *Chem. Commun.* **2014**, *50*, 11026.
- [129] F. Hu, S. Zhu, S. Chen, Y. Li, L. Ma, T. Wu, Y. Zhang, C. Wang, C. Liu, X. Yang, L. Song, X. Yang, Y. Xiong, *Adv. Mater.* **2017**, *29*, 1606570.
- [130] J. F. Callejas, C. G. Read, E. J. Popczun, J. M. McEnaney, R. E. Schaak, *Chem. Mater.* **2015**, *27*, 3769.
- [131] Y. Pan, Y. Liu, J. Zhao, K. Yang, J. Liang, D. Liu, W. Hu, D. Liu, Y. Liu, C. Liu, *J. Mater. Chem. A* **2015**, *3*, 1656.
- [132] P. Xiao, M. A. Sk, L. Thia, X. Ge, R. J. Lim, J.-Y. Wang, K. H. Lim, X. Wang, *Energy Environ. Sci.* **2014**, *7*, 2624.
- [133] H. Li, Q. Li, P. Wen, T. B. Williams, S. Adhikari, C. Dun, C. Lu, D. Itanze, L. Jiang, D. L. Carroll, G. L. Donati, P. M. Lundin, Y. Qiu, S. M. Geyer, *Adv. Mater.* **2018**, *30*, 1705796.
- [134] A. Kondori, M. Esmaeilirad, A. Baskin, B. Song, J. Wei, W. Chen, C. U. Segre, R. Shahbazian-Yassar, D. Prendergast, M. Asadi, *Adv. Energy Mater.* **2019**, *9*, 1900516.
- [135] D. E. Schipper, Z. Zhao, H. Thirumalai, A. P. Leitner, S. L. Donaldson, A. Kumar, F. Qin, Z. Wang, L. C. Grabow, J. Bao, K. H. Whitmire, *Chem. Mater.* **2018**, *30*, 3588.
- [136] a) J. Hou, Y. Wu, B. Zhang, S. Cao, Z. Li, L. Sun, *Adv. Funct. Mater.* **2019**, *29*, 1808367; b) J. Joo, T. Kim, J. Lee, S.-I. Choi, K. Lee, *Adv. Mater.* **2019**, *31*, 1806682.
- [137] a) S. Peng, G. Jin, L. Li, K. Li, M. Srinivasan, S. Ramakrishna, J. Chen, *Chem. Soc. Rev.* **2016**, *45*, 1225; b) Y. Liu, N. Zhang, L. Jiao, J. Chen, *Adv. Mater.* **2015**, *27*, 6702; c) T. Jin, Y. Liu, Y. Li, K. Cao, X. Wang, L. Jiao, *Adv. Energy Mater.* **2017**, *7*, 1700087.
- [138] Y. Yang, H. Fei, G. Ruan, J. M. Tour, *Adv. Mater.* **2015**, *27*, 3175.
- [139] J.-J. Miao, L.-P. Jiang, C. Liu, J.-M. Zhu, J.-J. Zhu, *Inorg. Chem.* **2007**, *46*, 5673.
- [140] G. Anandhababu, Y. Huang, D. D. Babu, M. Wu, Y. Wang, *Adv. Funct. Mater.* **2018**, *28*, 1706120.
- [141] H. Sun, X. Xu, Z. Yan, X. Chen, F. Cheng, P. S. Weiss, J. Chen, *Chem. Mater.* **2017**, *29*, 8539.
- [142] Y. Lian, H. Sun, X. Wang, P. Qi, Q. Mu, Y. Chen, J. Ye, X. Zhao, Z. Deng, Y. Peng, *Chem. Sci.* **2019**, *10*, 464.
- [143] X. Wang, Z. Na, D. Yin, C. Wang, Y. Wu, G. Huang, L. Wang, *ACS Nano* **2018**, *12*, 12238.
- [144] a) Q. Chen, K. Sieradzki, *Nat. Mater.* **2013**, *12*, 1102; b) C. Wang, Q. Chen, *Chem. Mater.* **2018**, *30*, 3894; c) Q. Chen, Y. Ding, M. Chen, *MRS Bull.* **2018**, *43*, 43.
- [145] Y. Tan, H. Wang, P. Liu, C. Cheng, F. Zhu, A. Hirata, M. Chen, *Adv. Mater.* **2016**, *28*, 2951.
- [146] X. Yu, M. Wang, X. Gong, Z. Guo, Z. Wang, S. Jiao, *Adv. Energy Mater.* **2018**, *8*, 1802445.
- [147] a) S. Wu, K. S. Hui, K. N. Hui, *Adv. Sci.* **2018**, *5*, 1700491; b) W. Lei, G. Liu, J. Zhang, M. Liu, *Chem. Soc. Rev.* **2017**, *46*, 3492.
- [148] Z.-Z. Luo, Y. Zhang, C. Zhang, H. T. Tan, Z. Li, A. Abutaha, X.-L. Wu, Q. Xiong, K. A. Khor, K. Hippalgaonkar, J. Xu, H. H. Hng, Q. Yan, *Adv. Energy Mater.* **2017**, *7*, 1601285.
- [149] J. Wang, D. Liu, H. Huang, N. Yang, B. Yu, M. Wen, X. Wang, P. K. Chu, X. F. Yu, *Angew. Chem., Int. Ed.* **2018**, *57*, 2600.
- [150] B. Anasori, M. R. Lukatskaya, Y. Gogotsi, *Nat. Rev. Mater.* **2017**, *2*, 16098.
- [151] L. Xiu, Z. Wang, M. Yu, X. Wu, J. Qiu, *ACS Nano* **2018**, *12*, 8017.
- [152] a) H. Sun, Z. Yan, F. Liu, W. Xu, F. Cheng, J. Chen, *Adv. Mater.* **2019**, <https://doi.org/10.1002/adma.201806326>; b) T. Y. Ma, S. Dai, S. Z. Qiao, *Mater. Today* **2016**, *19*, 265.
- [153] Y.-P. Zhu, Y.-P. Liu, T.-Z. Ren, Z.-Y. Yuan, *Adv. Funct. Mater.* **2015**, *25*, 7337.
- [154] L. Ma, X. Shen, H. Zhou, G. Zhu, Z. Ji, K. Chen, J. Mater. Chem. A **2015**, *3*, 5337.
- [155] a) Y. Li, G. A. Somorjai, *Nano Lett.* **2010**, *10*, 2289; b) Y. Yang, M. Luo, Y. Xing, S. Wang, W. Zhang, F. Lv, Y. Li, Y. Zhang, W. Wang, S. Guo, *Adv. Mater.* **2018**, *30*, 1706085.
- [156] a) X. Wang, K. Cao, Y. Wang, L. Jiao, *Small* **2017**, *13*, 1700873; b) M. Q. Wang, C. Ye, H. Liu, M. Xu, S. J. Bao, *Angew. Chem., Int. Ed.* **2018**, *57*, 1963.
- [157] J. Yang, F. Zhang, X. Wang, D. He, G. Wu, Q. Yang, X. Hong, Y. Wu, Y. Li, *Angew. Chem., Int. Ed.* **2016**, *55*, 12854.
- [158] Y. Li, H. Li, K. Cao, T. Jin, X. Wang, H. Sun, J. Ning, Y. Wang, L. Jiao, *Energy Storage Mater.* **2018**, *12*, 44.
- [159] D. Y. Chung, S. W. Jun, G. Yoon, H. Kim, J. M. Yoo, K.-S. Lee, T. Kim, H. Shin, A. K. Sinha, S. G. Kwon, K. Kang, T. Hyeon, Y.-E. Sung, *J. Am. Chem. Soc.* **2017**, *139*, 6669.
- [160] G. W. Li, Y. Sun, J. C. Rao, J. Q. Wu, A. Kumar, Q. N. Xu, C. G. Fu, E. K. Liu, G. R. Blake, P. Werner, B. Q. Shao, K. Liu, S. Parkin, X. J. Liu, M. Fahlman, S.-C. Liou, G. Auffermann, J. Zhang, C. Felser, X. L. Feng, *Adv. Energy Mater.* **2018**, *8*, 1801258.
- [161] Y. Lin, L. Yang, Y. Zhang, H. Jiang, Z. Xiao, C. Wu, G. Zhang, J. Jiang, L. Song, *Adv. Energy Mater.* **2018**, *8*, 1703623.
- [162] Y.-Y. Ma, C.-X. Wu, X.-J. Feng, H.-Q. Tan, L.-K. Yan, Y. Liu, Z.-H. Kang, E.-B. Wang, Y.-G. Li, *Energy Environ. Sci.* **2017**, *10*, 788.
- [163] a) J. Yu, Y. Guo, S. She, S. Miao, M. Ni, W. Zhou, M. Liu, Z. Shao, *Adv. Mater.* **2018**, *30*, 1800047; b) K. Wang, B. Huang, F. Lin, F. Lv, M. Luo, P. Zhou, Q. Liu, W. Zhang, C. Yang, Y. Tang, Y. Yang, W. Wang, H. Wang, S. Guo, *Adv. Energy Mater.* **2018**, *8*, 1801891.
- [164] Z. Pu, I. S. Amiiniu, Z. Kou, W. Li, S. Mu, *Angew. Chem., Int. Ed.* **2017**, *56*, 11559.
- [165] a) L. Fang, Y. Wang, X. Yang, H. Zhang, Y. Wang, *J. Catal.* **2019**, *370*, 404; b) Z. H. Pu, J. H. Zhao, I. S. Amiiniu, W. Q. Li, M. Wang, D. P. He, S. C. Mu, *Energy Environ. Sci.* **2019**, *12*, 952.

- [166] Q. Qin, H. Jang, L. Chen, G. Nam, X. Liu, J. Cho, *Adv. Energy Mater.* **2018**, *8*, 1801478.
- [167] a) M. A. Abbas, J. H. Bang, *Chem. Mater.* **2015**, *27*, 7218; b) J. Kibsgaard, I. Chorkendorff, *Nat. Energy* **2019**, *4*, 430; c) Y. L. Zhang, M. C. Luo, Y. Yang, Y. J. Li, S. J. Guo, *ACS Energy Lett.* **2019**, *4*, 1672.
- [168] B. Xiong, L. Chen, J. Shi, *ACS Catal.* **2018**, *8*, 3688.
- [169] R. Wu, B. Xiao, Q. Gao, Y.-R. Zheng, X.-S. Zheng, J.-F. Zhu, M. R.-Gao, S.-H. Yu, *Angew. Chem.* **2018**, *130*, 15671.
- [170] Y. Li, S. Guo, T. Jin, Y. Wang, F. Cheng, L. Jiao, *Nano Energy* **2019**, *63*, 103821.
- [171] a) F. Cheng, J. Chen, *Chem. Soc. Rev.* **2012**, *41*, 2172; b) Y. Shao, F. Ding, J. Xiao, J. Zhang, W. Xu, S. Park, J.-G. Zhang, Y. Wang, J. Liu, *Adv. Funct. Mater.* **2013**, *23*, 987.
- [172] a) Y. Li, H. Dai, *Chem. Soc. Rev.* **2014**, *43*, 5257; b) X. Wang, Y. Li, T. Jin, J. Meng, L. Jiao, M. Zhu, J. Chen, *Nano Lett.* **2017**, *17*, 7989.
- [173] J.-S. Lee, S. T. Kim, R. Cao, N.-S. Choi, M. Liu, K. T. Lee, J. Cho, *Adv. Energy Mater.* **2011**, *1*, 34.
- [174] R. Wang, X.-Y. Dong, J. Du, J.-Y. Zhao, S.-Q. Zang, *Adv. Mater.* **2018**, *30*, 1703711.
- [175] a) X. Hou, Y. Jiang, Y.-S. He, Z.-F. Ma, J. Yang, X. Yuan, *J. Electrochem. Soc.* **2018**, *165*, A2904; b) J. Wang, R. Gao, L. Zheng, Z. Chen, Z. Wu, L. Sun, Z. Hu, X. Liu, *ACS Catal.* **2018**, *8*, 8953.
- [176] a) H.-J. Peng, J.-Q. Huang, Q. Zhang, *Chem. Soc. Rev.* **2017**, *46*, 5237; b) L. Ma, W. Zhang, L. Wang, Y. Hu, G. Zhu, Y. Wang, R. Chen, T. Chen, Z. Tie, J. Liu, Z. Jin, *ACS Nano* **2018**, *12*, 4868; c) L. Zhang, X. Chen, F. Wan, Z. Niu, Y. Wang, Q. Zhang, J. Chen, *ACS Nano* **2018**, *12*, 9578.
- [177] Z. Wang, J. Shen, J. Liu, X. Xu, Z. Liu, R. Hu, L. Yang, Y. Feng, J. Liu, Z. Shi, L. Ouyang, Y. Yu, M. Zhu, *Adv. Mater.* **2019**, *31*, 1902228.
- [178] a) M.-Q. Zhao, Q. Zhang, J.-Q. Huang, G.-L. Tian, J.-Q. Nie, H.-J. Peng, F. Wei, *Nat. Commun.* **2014**, *5*, 3410; b) J. Cao, C. Chen, Q. Zhao, N. Zhang, Q. Lu, X. Wang, Z. Niu, J. Chen, *Adv. Mater.* **2016**, *28*, 9629.
- [179] K. Cao, H. Liu, Y. Li, Y. Wang, L. Jiao, *Energy Storage Mater.* **2017**, *9*, 78.
- [180] Z. Yuan, H.-J. Peng, T.-Z. Hou, J.-Q. Huang, C.-M. Chen, D.-W. Wang, X.-B. Cheng, F. Wei, Q. Zhang, *Nano Lett.* **2016**, *16*, 519.
- [181] S. Huang, Y. V. Lim, X. Zhang, Y. Wang, Y. Zheng, D. Kong, M. Ding, S. A. Yang, H. Y. Yang, *Nano Energy* **2018**, *51*, 340.
- [182] J. Zhou, X. Liu, L. Zhu, J. Zhou, Y. Guan, L. Chen, S. Niu, J. Cai, D. Sun, Y. Zhu, J. Du, G. Wang, Y. Qian, *Joule* **2018**, *2*, 2681.
- [183] Y. Yang, Y. Zhong, Q. Shi, Z. Wang, K. Sun, H. Wang, *Angew. Chem., Int. Ed.* **2018**, *57*, 15549.
- [184] H. Yuan, X. Chen, G. Zhou, W. Zhang, J. Luo, H. Huang, Y. Gan, C. Liang, Y. Xia, J. Zhang, J. Wang, X. Tao, *ACS Energy Lett.* **2017**, *2*, 1711.
- [185] a) Y. Zhong, X. Xia, S. Deng, D. Xie, S. Shen, K. Zhang, W. Guo, X. Wang, J. Tu, *Adv. Mater.* **2018**, *30*, 1805165; b) X. X. Chen, S. Y. Zeng, H. Muheiyati, Y. J. Zhai, C. C. Li, X. Y. Ding, L. Wang, D. B. Wang, L. Q. Xu, Y. Y. He, Y. T. Qian, *ACS Energy Lett.* **2019**, *4*, 1496.
- [186] a) B. Kumar, M. Asadi, D. Pisasale, S. Sinha-Ray, B. A. Rosen, R. Haasch, J. Abiade, A. L. Yarin, A. Salehi-Khojin, *Nat. Commun.* **2013**, *4*, 2819; b) H. Yang, N. Han, J. Deng, J. Wu, Y. Wang, Y. Hu, P. Ding, Y. Li, Y. Li, J. Lu, *Adv. Energy Mater.* **2018**, *8*, 1801536; c) O. S. Bushuyev, P. De Luna, C. T. Dinh, L. Tao, G. Saur, J. van de Lagemaat, S. O. Kelley, E. H. Sargent, *Joule* **2018**, *2*, 825.
- [187] A. A. Peterson, J. K. Nørskov, *J. Phys. Chem. Lett.* **2012**, *3*, 251.
- [188] A. Khoshidi, J. Violet, J. Hashemi, A. A. Peterson, *Nat. Catal.* **2018**, *1*, 263.
- [189] A. T. Landers, M. Fields, D. A. Torelli, J. Xiao, T. R. Hellstern, S. A. Francis, C. Tsai, J. Kibsgaard, N. S. Lewis, K. Chan, C. Hahn, T. F. Jaramillo, *ACS Energy Lett.* **2018**, *3*, 1450.
- [190] M. Fields, C. Tsai, L. D. Chen, F. Abild-Pedersen, J. K. Nørskov, K. Chan, *ACS Catal.* **2017**, *7*, 2528.
- [191] K. U. D. Calvinho, A. B. Laursen, K. M. K. Yap, T. A. Goetjen, S. Hwang, N. Murali, B. Mejia-Sosa, A. Lubarski, K. M. Teeluck, E. S. Hall, E. Garfunkel, M. Greenblatt, G. C. Dismukes, *Energy Environ. Sci.* **2018**, *11*, 2550.
- [192] a) X. Xiao, C.-T. He, S. Zhao, J. Li, W. Lin, Z. Yuan, Q. Zhang, S. Wang, L. Dai, D. Yu, *Energy Environ. Sci.* **2017**, *10*, 893; b) X.-Y. Yu, Y. Feng, B. Guan, X. W. Lou, U. Paik, *Energy Environ. Sci.* **2016**, *9*, 1246; c) J. Zhou, Y. Dou, A. Zhou, R.-M. Guo, M.-J. Zhao, J.-R. Li, *Adv. Energy Mater.* **2017**, *7*, 1602643.
- [193] Y. Chen, A. Lavacchi, H. Miller, M. Bevilacqua, J. Filippi, M. Innocenti, A. Marchionni, W. Oberhauser, L. Wang, F. Vizza, *Nat. Commun.* **2014**, *5*, 4036.
- [194] B. You, N. Jiang, X. Liu, Y. Sun, *Angew. Chem., Int. Ed.* **2016**, *55*, 9913.
- [195] C. Huang, Y. Huang, C. Liu, Y. Yu, B. Zhang, *Angew. Chem., Int. Ed.* **2019**, *58*, 12014.
- [196] a) M. Liu, R. Zhang, L. Zhang, D. Liu, S. Hao, G. Du, A. M. Asiri, R. Kong, X. Sun, *Inorg. Chem. Front.* **2017**, *4*, 420; b) C. Tang, R. Zhang, W. Lu, Z. Wang, D. Liu, S. Hao, G. Du, A. M. Asiri, X. Sun, *Angew. Chem., Int. Ed.* **2017**, *56*, 842.
- [197] L. Xie, Q. Liu, Y. Luo, Z. Liu, Y. Xu, A. M. Asiri, X. Sun, F. Xie, *ChemistrySelect* **2017**, *2*, 10285.
- [198] S. Hao, L. Yang, D. Liu, R. Kong, G. Du, A. M. Asiri, Y. Yang, X. Sun, *Chem. Commun.* **2017**, *53*, 5710.
- [199] a) M. K. Debe, *Nature* **2012**, *486*, 43; b) Y. Chen, W. Zhou, D. Ding, M. Liu, F. Ciucci, M. Tade, Z. Shao, *Adv. Energy Mater.* **2015**, *5*, 1500537.
- [200] a) J. Zhu, S. Huang, J. Key, S. Nie, S. Ma, P. K. Shen, *Catal. Sci. Technol.* **2017**, *7*, 5974; b) J. Chang, L. Feng, K. Jiang, H. Xue, W.-B. Cai, C. Liu, W. Xing, *J. Mater. Chem. A* **2016**, *4*, 18607.
- [201] M. Zhao, K. Abe, S.-i. Yamaura, Y. Yamamoto, N. Asao, *Chem. Mater.* **2014**, *26*, 1056.
- [202] Z. Kang, M. Zhao, Y. Wu, T. Xia, J.-P. Cao, W. Cai, L. Chen, *Appl. Surf. Sci.* **2019**, *484*, 441.
- [203] L. Feng, K. Li, J. Chang, C. Liu, W. Xing, *Nano Energy* **2015**, *15*, 462.
- [204] A. R. J. Kucernak, K. F. Fahy, V. N. N. Sundaram, *Catal. Today* **2016**, *262*, 48.
- [205] H. Lv, L. Sun, D. Xu, Y. Ma, B. Liu, *Appl. Catal., B* **2019**, *253*, 271.
- [206] L. Chen, L. Lu, H. Zhu, Y. Chen, Y. Huang, Y. Li, L. Wang, *Nat. Commun.* **2017**, *8*, 14136.
- [207] J. Xu, Y. Liu, J. Li, I. Amorim, B. Zhang, D. Xiong, N. Zhang, S. M. Thalluri, J. P. S. Sousa, L. Liu, *J. Mater. Chem. A* **2018**, *6*, 20646.
- [208] Q. Q. Sun, M. Wang, S. J. Bao, Y. C. Wang, S. Gu, *Analyst* **2016**, *141*, 256.
- [209] Y. Liu, X. Cao, R. Kong, G. Du, A. M. Asiri, Q. Lu, X. Sun, *J. Mater. Chem. B* **2017**, *5*, 1901.
- [210] a) C. Wei, R. R. Rao, J. Peng, B. Huang, I. E. L. Stephens, M. Risch, Z. J. Xu, Y. Shao-Horn, *Adv. Mater.* **2019**, *31*, 1806296; b) S. Anantharaj, S. R. Ede, K. Karthick, S. Sam Sankar, K. Sangeetha, P. E. Karthik, S. Kundu, *Energy Environ. Sci.* **2018**, *11*, 744; c) E. L. Clark, J. Resasco, A. Landers, J. Lin, L.-T. Chung, A. Walton, C. Hahn, T. F. Jaramillo, A. T. Bell, *ACS Catal.* **2018**, *8*, 6560.